

# **CORROSION OF ALLOY 22 INDUCED BY DUST DELIQUESCENCE BRINES**

*Prepared for*

**U.S. Nuclear Regulatory Commission  
Contract NRC-02-07-006**

*Prepared by*

**L. Yang<sup>1</sup>  
R. Pabalan<sup>1</sup>  
P. Shukla<sup>1</sup>  
M. Juckett<sup>1</sup>  
X. He<sup>1</sup>  
K.T. Chiang<sup>1</sup>  
H. Gonzalez<sup>2</sup>  
T. Ahn<sup>2</sup>**

**<sup>1</sup>Center for Nuclear Waste Regulatory Analyses  
San Antonio, Texas**

**<sup>2</sup>U.S. Nuclear Regulatory Commission  
Washington, DC**

**March 2011**

## ABSTRACT

In the potential repository at Yucca Mountain, Nevada, nuclear waste materials would be housed in waste packages. The U.S. Department of Energy is considering Alloy 22 as the material for the outer container of the waste packages. During the preclosure period, the potential repository drift would be ventilated and atmospheric aerosols and tunnel dusts could be deposited onto the waste package surfaces by the ventilation, leading to the accumulation of small amounts of hygroscopic salts on the waste package surfaces. The hygroscopic salts could deliquesce and form a brine solution on the waste package surfaces when the relative humidity of the in-drift environment is near or above the salt's deliquescence relative humidity. This report evaluates Alloy 22 corrosion by the deliquescence brines under potential repository conditions.

The Yucca Mountain dusts and their salt contents were reviewed, and the brine properties that may be formed from the dust salts under potential drift conditions (high temperature and low relative humidity) are discussed. Because the brines formed under potential Yucca Mountain conditions are expected to be mixed with large amounts of nondeliquescent dust mixtures, an experimental assessment on the corrosion of metals in contact with the deliquescent and nondeliquescent dust mixtures was also conducted.

General corrosion of Alloy 22 in bulk deliquescence brines containing  $\text{Na}^+$ ,  $\text{K}^+$ ,  $\text{Cl}^-$ , and  $\text{NO}_3^-$  ions at elevated temperatures in closed systems (autoclaves) has been reported in the literature. Because the potential drift would be open to the atmosphere, experiments on Alloy 22 corrosion in open systems were conducted in the present study. In these experiments, the pH effects of the brine solution on the corrosion of Alloy 22 and the verification test for the pH effect were evaluated. The general corrosion rates of Alloy 22 in  $\text{NaCl-NaNO}_3\text{-KNO}_3$  brines were equal to or less than  $1 \mu\text{m/yr}$  [ $0.04 \text{ mil/yr}$ ] in the temperature range from  $120$  to  $220 \text{ }^\circ\text{C}$  [ $248$  to  $428 \text{ }^\circ\text{F}$ ] and a pH range of the brine solution from  $4.8$  to  $8.5$  (as measured at room temperature after tenfold dilution by weight).

Literature data on electrochemical tests and immersion tests for localized corrosion of Alloy 22 in large quantities of deliquescence brine systems were reviewed. A detailed model analysis on the possibility of localized corrosion of Alloy 22 in a nondeliquescent dust and deliquescent salt mixture under the potential Yucca Mountain drift conditions was conducted. Electrochemical potential (repassivation and corrosion) data suggest that localized corrosion in the form of crevice corrosion would not initiate for Alloy 22 in large quantities of brines at temperatures between  $120$  and  $150 \text{ }^\circ\text{C}$  [ $248$  and  $302 \text{ }^\circ\text{F}$ ]. However, previous investigators have reported pitting and crevice corrosion in immersion tests for specimens exposed to both closed and open systems containing large amounts of brines that contrast the electrochemical test results. Additional long-term immersion tests may resolve this discrepancy. Calculated cathodic capacities of Alloy 22 in dust deliquescence brines suggest that the high penetration rate due to localized corrosion may not be sustained under limited brine amounts in potential Yucca Mountain drift conditions.

# CONTENTS

Section	Page
ABSTRACT .....	ii
FIGURES .....	v
TABLES .....	vii
ACKNOWLEDGMENTS .....	viii
1 INTRODUCTION .....	1-1
1.1 Background .....	1-1
1.2 Scope and Organization of the Report .....	1-2
1.3 References .....	1-2
2 YUCCA MOUNTAIN DUSTS AND BRINE FORMATION AT ELEVATED TEMPERATURES .....	2-1
2.1 Overview of Salt Deliquescence .....	2-1
2.2 Characterization Data on Dusts Sampled From Yucca Mountain and Vicinity .....	2-3
2.2.1 Yucca Mountain Crest Data .....	2-3
2.2.2 Yucca Mountain Tunnel Data .....	2-4
2.2.3 Atmospheric (Cyclone) Dust Data .....	2-5
2.2.4 Remote Dust Data .....	2-7
2.3 Potential Composition of Brines Formed by Deliquescence of Salts Present in Yucca Mountain Dusts .....	2-7
2.4 Effect of Capillary Retention by Dusts on the Corrosivity of Deliquescence Brines .....	2-18
2.4.1 Test Methods .....	2-18
2.4.2 Test Results .....	2-19
2.4.2.1 Test 1—NaCl—Quartz Mixture at 70 °C [158 °F] .....	2-19
2.4.2.2 Test 2—NaCl—Dust Mixture at 70 °C [158 °F] .....	2-21
2.4.2.3 Test 3—NaCl—Quartz and NaCl—Dust Mixtures at 70 °C [158 °F] .....	2-23
2.4.2.4 Test 4—Effect of Dust Particle Sizes .....	2-24
2.4.2.5 Test 5—Alloy 22 and Carbon Steel Corrosion in NaCl—NaNO <sub>3</sub> —KNO <sub>3</sub> Dust Mixture at 125 °C [257 °F] .....	2-24
2.5 Summary and Conclusions .....	2-26
2.6 References .....	2-28
3 CORROSIVITY OF DELIQUESCENT BRINES TO ALLOY 22 AT ELEVATED TEMPERATURES .....	3-1
3.1 Corrosion Rate of Alloy 22 in Nitrate—Chloride Salt Systems Measured in Closed Systems .....	3-1
3.2 Corrosion Rate of Alloy 22 in Nitrate—Chloride Salt Systems Measured in Open Systems .....	3-2
3.2.1 Test Specimens .....	3-2
3.2.2 Test Vessels for Weight Loss Corrosion Rate Measurements .....	3-4
3.2.3 Test Vessels for Characterization of Vapor Phase Acidity .....	3-5
3.2.4 Weight Loss Results .....	3-6
3.2.5 Effect of pH on Corrosion Rate .....	3-10

## CONTENTS (continued)

Section	Page
3.3	Verification of the pH Effect on Alloy 22 Corrosion and Understanding of the pH Variations in the NaCl–NaNO <sub>3</sub> –KNO <sub>3</sub> Systems .....3-15
3.3.1	Corrosion Rates Measured With Coupled Multielectrode Array Sensors .....3-15
3.3.2	Causes for the Variations in the pH of the NaCl–NaNO <sub>3</sub> –KNO <sub>3</sub> Systems .....3-16
3.4	Summary .....3-21
3.5	References .....3-23
4	LOCALIZED CORROSION OF ALLOY 22 IN DUST DELIQUESCENCE BRINES .....4-1
4.1	Electrochemical Test Data on Localized Corrosion in Large Quantity of Brines .....4-1
4.2	Immersion Test Data on Localized Corrosion in Large Quantity of Brines .....4-5
4.3	Localized Corrosion Model for Alloy 22 in Dust Deliquescence Brines Under Potential Repository Conditions.....4-6
4.3.1	Model Development.....4-7
4.3.2	Model Parameters .....4-12
4.3.3	Calculated Cathodic Capacities.....4-16
4.3.4	Discussion on Cathodic Capacity Results .....4-19
4.4	Summary .....4-21
4.5	References .....4-21
5	SUMMARY AND CONCLUSIONS .....5-1
5.1	Formation of Deliquescence Brines at Elevated Temperatures and Low Relative Humidities .....5-1
5.2	Corrosivity of Potential Deliquescence Brines to Alloy 22 Waste Package Materials .....5-2
5.3	Localized Corrosion of Alloy 22 in Deliquescence Brines Under Potential Yucca Mountain Conditions .....5-2

## FIGURES

Figure	Page
2-1 Plot of Calculated Waste Package Temperature and Relative Humidity at the Potential Yucca Mountain Repository.....	2-2
2-2 Calculated Relative Humidity at 25 °C [77 °F] Over an Aqueous Solution Saturated With Either NaCl, NaNO <sub>3</sub> , or Both as a Function of Salt Mixture Composition.....	2-2
2-3 Calculated Deliquescence Relative Humidity Shown as Contour Lines of Different Salts and Salt Mixtures in the System NaCl–KCl–MgCl <sub>2</sub> at 90 °C [194 °F] .....	2-4
2-4 Calculated Deliquescence Relative Humidity of Different Salts and Salt Mixtures in the System Na–K–Cl–NO <sub>3</sub> as a Function of Temperature.....	2-5
2-5 Mineral Precipitates Calculated to Form Upon Evaporation of Initially Dilute Dust Leachates.....	2-12
2-6 Evolution of the Nitrate-to-Chloride Molar Ratio as More Water Is Taken Up by the Deliquescent Salt Assemblage at 110 °C [230 °F] .....	2-17
2-7 Schematic of Test Setup Used in Studying the Effect of Capillary Retention by Dusts on the Corrosivity of Deliquescence Brines.....	2-19
2-8 Maximum Corrosion Current Measured From Test 1 Carbon Steel Probes.....	2-20
2-9 Posttest Photographs of the Test 1 Carbon Steel Probes.....	2-21
2-10 (a) Measured Maximum Corrosion Current and (b) Calculated Corrosion Rate for Test 2 Carbon Steel Probes .....	2-22
2-11 Posttest Photographs of the Carbon Steel Probes From Test 2 .....	2-23
2-12 Maximum Corrosion Current Measured From the Test 3 Carbon Steel Probes.....	2-24
2-13 Maximum Corrosion Current Measured From the Test 4 Carbon Steel Probes.....	2-25
2-14 (a) Maximum Corrosion Current Measured From Test 5 Probes .....	2-27
3-1 Schematic Diagrams for the Creviced Specimens Used in the Tests .....	3-3
3-2 Schematic of Typical Glass Vessels Used for the Weight Loss Experiment .....	3-5
3-3 Schematic of Typical Glass Flask Used for the Characterization of Vapor Phase pH.....	3-6
3-4 Optical Appearance of the Specimens After the Tests in Liquid Phase .....	3-9
3-5 pH of the Vent-Bubbler Water and the Deionized Makeup Water That Was Added to the Test Vessels and Vent-Bubblers During the Tests .....	3-11
3-6 pH of the Vent-Bubbler Water During the Tests Conducted in Vessels A', B', and C' .....	3-12
3-7 Average Corrosion Rates for Alloy 22 as a Function of pH of the Vent-Bubbler Water .....	3-13
3-8 Relationship Between the pH of the Diluted Sample From the Liquid Phase and the pH of the Bubbler Water .....	3-14
3-9 Relationship Between Corrosion Rates of the Alloy 22 Specimens Exposed to the Liquid Phase.....	3-14
3-10 (a) Schematic Diagram of the Coated Multielectrode Array Sensor and (b) Photograph of a Coated Alloy 22 Multielectrode Array Sensor .....	3-15
3-11 Maximum Corrosion Rates for Alloy 22 Measured With a Coupled Multielectrode Array Sensor at Different pH in the NaCl–NaNO <sub>3</sub> –KNO <sub>3</sub> System .....	3-17
3-12 Relationship Between the Maximum Corrosion Rates Measured With the Alloy 22 Coupled Multielectrode Array Sensor and the pH of the Diluted Samples .....	3-17
3-13 Effect of Atmospheric Components on the pH of the Condenser Water Above the Test Flasks Containing Wet NaCl, NaNO <sub>3</sub> , and KNO <sub>3</sub> Salt Mixtures.....	3-19

## FIGURES (continued)

Figure	Page
3-14	Calculated Effect of Addition of SiO <sub>2</sub> and Dissolved SiO <sub>2</sub> Concentration on the pH of the NaCl–NaNO <sub>3</sub> –KNO <sub>3</sub> Solution at 160 °C [320 °F] .....3-19
3-15	Calculated Effect of the Addition of B(OH) <sub>3</sub> and Dissolved B(OH) <sub>3</sub> Concentration on the pH of NaCl–NaNO <sub>3</sub> Solution at 160 °C [320 °F] .....3-20
3-16	Calculated Effect of the Addition of P <sub>2</sub> O <sub>5</sub> and the Dissolved P <sub>2</sub> O <sub>5</sub> Concentration on the pH of NaCl–NaNO <sub>3</sub> –KNO <sub>3</sub> Solution at 160 °C [320 °F] .....3-20
3-17	(a) Corrosion Rates and (b) Open Circuit Potential Versus pH for Alloy 22 in Hydrochloric, Sulfuric, and Nitric With 4 m NaCl at 90 °C [194 °F].....3-22
4-1	Corrosion Potential Versus Time of Alloy 22 in 25 m NO <sub>3</sub> <sup>-</sup> +1 m Cl <sup>-</sup> Solution With the pH Adjusted to Different Values at 110 °C [230 °F].....4-2
4-2	Graphical Representation of the E <sub>rp</sub> Data Tabulated in Table 4-1 .....4-4
4-3	Schematic Diagram of the Crevice Corrosion Process. ....4-7
4-4	Schematic Representation of the Cathodic Region With Corresponding Cathodic and Anodic Polarization Curves .....4-10
4-5	Schematic Representation of Dust Deliquescence Brine Layer and Dust Layer on Alloy 22 Surface .....4-15
4-6	(a) Electrode Potential and (b) Current Density Distribution of Alloy 22 in the Cathodic Region .....4-17
4-7	Cathodic Capacity of Alloy 22 in Dust Deliquescence Brine as a Function of the Difference Between the Corrosion Potential and the Repassivation Potential .....4-18
4-8	Cathodic Capacity of Alloy 22 in Dust Deliquescence Brines as a Function of the Difference Between the Corrosion Potential and the Repassivation Potential .....4-19
4-9	Cathodic Capacity of Alloy 22 in Dust Deliquescence Brines as a Function of the Difference Between the Corrosion Potential and the Repassivation Potential .....4-20

## TABLES

Table	Page
2-1 Center for Nuclear Waste Regulatory Analyses Data on the Composition of Leachates of Dusts Sampled From the Surface of Yucca Crest (mg/L).....	2-5
2-2 Mineralogical Composition of Surface Samples Based on Center for Nuclear Waste Regulatory Analyses Powder X-Ray Diffraction Analysis.....	2-6
2-3 Composition of Leachates of Dusts Sampled From Inside the Tunnel at Yucca Mountain (mg/L) .....	2-6
2-4 Mineralogical Composition of Tunnel Samples Based on Center for Nuclear Waste Regulatory Analyses Powder X-Ray Diffraction Analysis.....	2-6
2-5 Center for Nuclear Waste Regulatory Analyses Data on the Composition of Leachates of Atmospheric Dusts Collected With the Torit Cyclone (mg/L) .....	2-8
2-6 Mineralogical Composition of Atmospheric Samples Based on Center for Nuclear Waste Regulatory Analyses Powder X-Ray Diffraction Analysis.....	2-8
2-7 Leachate Composition From the National Atmospheric Deposition Program Regional Precipitation (Rain Out) .....	2-9
2-8 Mineralogical Composition of Two Remote Sample Based on Center for Nuclear Waste Regulatory Analyses Powder X-Ray Diffraction Analysis.....	2-9
2-9 Composition of Leachable Portion of Dust Samples Taken From Yucca Mountain Tunnels .....	2-10
2-10 Salt Assemblages Derived From Evaporation of Dust Leachates With Composition Listed in Table 2-9. ....	2-11
2-11 Calculated Mutual Deliquescence Relative Humidity Percent As a Function of Temperature of Six Samples Representing Six Key Salt Assemblages.....	2-16
2-12 Calculated Molar Concentration Ratio of Chloride-to-Nitrate Ions As a Function of Temperature of Six Samples Representing Six Key Salt Assemblages.....	2-17
2-13 Chemical Compositions of Dust Leachate (ppm) .....	2-19
2-14 Chemical Composition of Brine Formed by Deliquescence of a NaCl–NaNO <sub>3</sub> –KNO <sub>3</sub> Salt Mixture at a Temperature of 125 °C [257 °F] .....	2-26
3-1 Specimens Used in the Experiments.....	3-3
3-2 Chemical Compositions of Specimen and Weld Fillers (in Weight Percent) .....	3-4
3-3 Corrosion Rates of Alloy 22 Specimens in the Liquid Vapor Phases and the pH of the Water in the Vent Bubbler Conducted in 2006 .....	3-7
3-4 Corrosion Rates of Alloy 22 Specimens in the Liquid and Vapor Phases and the pH of the Water in the Vent Bubbler Conducted in 2005 .....	3-10
4-1 Reported Value of Repassivation Potential $E_{rp}$ .....	4-3
4-2 Dust Particle Size, Dust Layer Thickness, Brine Film Thickness, and Ionic Conductivity and Effective Ionic Conductivity of Dust Deliquescence Brine.....	4-13
4-3 Calculated Deliquescence Relative Humidity, Dissolved Oxygen Concentration, and Ionic Conductivity of Deliquescence Salts at Various Temperatures .....	4-14
4-4 Effective Ionic Conductivity of Dust Deliquescence Brine Formed Between 120 and 170 °C [248 and 338 °F] .....	4-15

## ACKNOWLEDGMENTS

This report describes work performed by the Center for Nuclear Waste Regulatory Analyses (CNWRA<sup>®</sup>) and its contractors for the U.S. Nuclear Regulatory Commission (NRC) under Contract No. NRC-02-07-006. The activities reported here were performed on behalf of the NRC Office of Nuclear Material Safety and Safeguards, Division of High-Level Waste Repository Safety. This report is an independent product of CNWRA and does not necessarily reflect the view or regulatory position of the NRC. The NRC staff views expressed herein are preliminary and do not constitute a final judgment or determination of the matters addressed or of the acceptability of a license application for a geologic repository at Yucca Mountain.

The authors would like to thank J. Auguste, S. Young, and B. Derby for laboratory assistance. The authors acknowledge the technical review of G. Cragnolino, editorial review of L. Mulverhill, programmatic review of B. Sagar and D. Pickett, the technical discussions with Y.-M. Pan and K. Axler, and the administrative support of A. Ramos, J. Gonzalez, and B. Street in preparing this report.

The fabrication of the coupled multielectrode array sensor used in this study was financially supported by a CNWRA-sponsored Focused Internal Research and Development program.

## QUALITY OF DATA, ANALYSES, AND CODE DEVELOPMENT

**DATA:** All CNWRA-generated original data contained in this report meet the quality assurance requirements described in the Geosciences and Engineering Division Quality Assurance Manual. Sources for other data should be consulted for determining the level of quality for those data. Experimental data analyses have been recorded in CNWRA Scientific Notebooks 679E, 771, 737, and 851E.

**ANALYSES AND CODES:** The computer software Corrosion Analyzer™ (OLI Systems, Inc., 2006) was used in the analyses contained in this report. Corrosion Analyzer is commercial software controlled under the CNWRA quality assurance procedure “Development and Control of Scientific and Engineering Software” (TOP-18). Documentation for thermodynamic calculation in Section 2 can be found in Scientific Notebook 679E.

## Reference

OLI Systems, Inc. “Corrosion Analyzer Software.” Version 2.0. Morris Plains, New Jersey: OLI Systems, Inc. 2006.

Pabalan, R.T. “Verification and Validation of Mixed-Solvent Electrolyte Model for the Environmental Simulation Program and Analyzer Codes Developed by OLI Systems, Inc. (Morris Plains, NJ).” SN 679E. San Antonio, Texas: CNWRA. 2004.

# 1 INTRODUCTION

## 1.1 Background

The U.S. Department of Energy (DOE) is considering Alloy 22 as the outer container material of the waste package (Anderson, et al., 2003), which is an important component of the engineered barrier system designed to prevent or delay radionuclide release to the accessible environment. The U.S. Nuclear Regulatory Commission (NRC) and the Center for Nuclear Waste Regulatory Analyses staff are evaluating the corrosion behavior of Alloy 22 in the potential Yucca Mountain repository environment. Under the nominal-case scenario, corrosion of Alloy 22 is an important degradation process limiting the lifetime of the waste package (Bechtel SAIC Company, LLC, 2004).

During the preclosure period, which may last for several decades after waste package emplacement, the repository emplacement drifts would be actively ventilated (Sandia National Laboratory, 2007a). Atmospheric aerosols and tunnel dusts could be deposited onto the waste package surfaces by forced ventilation, leading to the accumulation of small amounts of hygroscopic salts on such surfaces (Bechtel SAIC Company, LLC, 2005a,b; Sandia National Laboratories, 2007a; Craig, et al., 2004). Hygroscopic salts could deliquesce (sorb moisture from the atmosphere) and form a brine solution on the waste package surfaces when the relative humidity of the in-drift environment is near or above the salt's deliquescence relative humidity.

According to Sandia National Laboratories (2007b), the temperature of the waste package surface is expected to be relatively low and constant during the ventilation period. However, the temperature is expected to increase after ventilation ceases or the drift is closed, reaching a maximum value shortly after the closure, followed by a gradual decrease thereafter. The maximum temperature at the waste package surface could be 203 °C [397 °F]. In parallel, the relative humidity in the drift is expected to be low during the ventilation period because of the relatively dry air blown from the outside and is expected to increase as soon as the drift is closed because water vapor pressure would tend to reach the ambient pressure. After drift closure, the relative humidity of the waste package is estimated to decrease slightly with the increase in temperature and then rise after the waste package temperature has peaked after approximately 200 years (Sandia National Laboratory, 2007b).

According to recent studies (Rard, 2004; Rard, et al., 2006), some salt assemblages (such as NaCl–NaNO<sub>3</sub>–KNO<sub>3</sub>) that may develop under the potential repository conditions can deliquesce at ambient pressure and temperatures over 190 °C [374 °F] with a corresponding relative humidity below 4.4 percent. Hence, brine may be present during the entire high temperature period.

The presence of brines on the waste package surfaces has important implications because many metals are more susceptible to localized corrosion or have higher general corrosion rates at higher temperatures when immersed in a brine system (Orme, et al., 2004; Yang, et al., 2003).

This report assesses Alloy 22 corrosion induced by dust deliquescence brines under potential drift conditions.

## 1.2 Scope and Organization of the Report

This report is organized into five chapters, including this introduction as Chapter 1.

The potential Yucca Mountain dusts and their salt contents were assessed, and the brine properties that may be formed from the dust salts under the potential emplacement drift conditions (high temperature and low relative humidity) are detailed in Chapter 2. Chapter 2 also includes an experimental assessment on the effect of nondeliquescent dusts mixed with soluble deliquescent salts on the corrosion of the metals contacting dust mixtures.

The general corrosion of Alloy 22 in bulk deliquescence brines containing  $\text{Na}^+$ ,  $\text{K}^+$ ,  $\text{Cl}^-$ , and  $\text{NO}_3^-$  ions at elevated temperatures is the subject of Chapter 3. A review on the corrosion of Alloy 22 in closed systems (autoclaves) and experiments on the corrosion of Alloy 22 in open systems (no deaeration, no exclusion of air) is presented in the chapter. The pH effects of the brine solution on Alloy 22 corrosion and the verification test for the pH effect are detailed in that chapter as well.

Localized corrosion of Alloy 22 in deliquescence brines at elevated temperatures is discussed in Chapter 4. This chapter includes a review of electrochemical test and immersion test results dealing with localized corrosion of Alloy 22 exposed to large quantities of deliquescence brines. A detailed model analysis on the possibility of localized corrosion of Alloy 22 in the mixture of nondeliquescent dusts and deliquescent salts under the potential Yucca Mountain drift conditions is also presented in this chapter.

Finally, a summary of conclusions is included in Chapter 5.

## 1.3 References

Anderson, M.J., N.R. Brown, J.D. Cloud, P.R.Z. Russell, and J. Trautner. "Waste Package Design for License Application." Proceedings of the 10<sup>th</sup> International High-Level Radioactive Waste Management Conference, Las Vegas, Nevada, March 30–April 3, 2003. Section E–7. Published on CD-ROM. La Grange Park, Illinois: American Nuclear Society. pp. 714–720. 2003.

Bechtel SAIC Company, LLC. "Analysis of Dust Deliquescence for FEP Screening." Report ANL–EBS–MD–000074. Rev. 01. Las Vegas, Nevada: Bechtel SAIC Company, LLC. 2005a.

———. "FEPs Screening of Processes and Issues in Drip Shield and Waste Package Degradation." Report ANL–EBS–PA–000002. Rev. 05. Las Vegas, Nevada: Bechtel SAIC Company, LLC. 2005b.

———. "WAPDEG Analysis of Waste Package and Drip Shield Degradation." Report ANL–EBS–PA–000001. Rev. 02. Las Vegas, Nevada: Bechtel SAIC Company, LLC. 2004a.

Craig, L., S. Carrol, and T. Wolery. "Deliquescence of  $\text{NaCl}$ – $\text{NaNO}_3$  and  $\text{KNO}_3$ – $\text{NaNO}_3$  Salt Mixtures at 90 °C in Water-Rock Interaction." R.B. Wanty and R.R. Seal II, eds. Vol. 2. London, England: Taylor Francis Group. pp. 1,275–1,278. 2004.

Orme, C.A., J. Gray, J. Hayes, L. Wong, R. Rebak, S. Carroll, J. Harper, and G. Gdowski. "Fiscal Year 2004 Summary Report: General Corrosion and Passive Film Stability." UCRL-TR-208588. Livermore, California: Lawrence Livermore National Laboratory. 2004.

Rard, J.A. "Results From Boiling Temperature Measurements for Saturated Solutions in the Systems  $\text{NaCl}+\text{KNO}_3+\text{H}_2\text{O}$ ,  $\text{NaNO}_3+\text{KNO}_3+\text{H}_2\text{O}$  and  $\text{NaCl}+\text{NaNO}_3+\text{KNO}_3+\text{H}_2\text{O}$ ." Report UCRL-TR-207054. Livermore, California: Lawrence Livermore National Laboratory. 2004.

Rard, J.A., K.J. Staggs, S.D. Day, and S.A. Carroll. "Boiling Temperature and Reversed Deliquescence Relative Humidity Measurements for Mineral Assemblages in the  $\text{NaCl}+\text{NaNO}_3+\text{KNO}_3+\text{Ca}(\text{NO}_3)_2+\text{H}_2\text{O}$  System." *Journal of Solution Chemistry*. Vol. 35. pp. 1,187-1,215. 2006.

Sandia National Laboratories. "Analysis of Dust Deliquescence for FEP Screening." Report ANL-EBS-MD-000074. Rev. 01, AD 01. Las Vegas, Nevada: Sandia National Laboratories. 2007a.

———. “Multiscale Thermohydrologic Model.” Report ANL–EBS–MD–00004. Rev. 03. Las Vegas, Nevada: Sandia National Laboratories. 2007b.

Yang, L., R.T. Pabalan, L. Browning, and D.S. Dunn. “Corrosion Behavior of Carbon Steel and Stainless Steel Materials Under Salt Deposits in Simulated Dry Repository Environments.” Scientific Basis for Nuclear Waste Management XXVII. Symposium Proceedings 757. R.J. Finch and D.B. Bullen, eds. Pittsburgh, Pennsylvania: Materials Research Society. pp. 791–797. 2003.

## 2 YUCCA MOUNTAIN DUSTS AND BRINE FORMATION AT ELEVATED TEMPERATURES

Deliquescence is a process in which a soluble substance sorbs water vapor from the air to form a saturated aqueous solution. At the potential high-level waste repository at Yucca Mountain, Nevada, deposition of aerosols and dusts entrained in ventilation air in the drifts of the potential repository could lead to the accumulation of hygroscopic salts on drip shield and waste package surfaces. The deliquescence of these salts, which would occur when the relative humidity in the environment is at or above the deliquescence relative humidity of the salt or the mutual deliquescence relative humidity of the salt mixture, could form brines potentially corrosive to the metallic engineered barriers. Formation of these brines could affect the performance of the waste package during the thermal period when the drift wall temperature is above the boiling point of water and seepage water is unlikely to enter the repository drift. During this time period (see Figure 2-1 for a typical illustration), localized corrosion of the Alloy 22 waste package outer container due to dust deliquescence could be facilitated by the elevated system temperature if corrosive brine contacts the waste package surface.

This chapter assesses the potential for deliquescence brines to form in the potential repository drift environment, to contact the waste package surface, and to initiate localized corrosion of the Alloy 22 waste package material. The assessment is based on geochemical data on dust samples taken from Yucca Mountain and its vicinity (e.g., Bechtel SAIC Company, 2004). The geochemical information is used in thermodynamic calculations to determine whether deliquescence brines can potentially form at elevated temperatures—corresponding to the dust deliquescence period indicated in Figure 2-1—and whether the brines that do form would have chemical compositions that could initiate localized corrosion of the Alloy 22 waste package outer container. In addition, experiments were conducted to determine whether capillary retention by nondeliquescent dust particles could prevent brines from contacting the waste package surface and mitigate localized corrosion degradation of the material.

### 2.1 Overview of Salt Deliquescence

The concept of deliquescence relative humidity for salt mixtures is illustrated in Figure 2-2, which shows the calculated relative humidity at 25 °C [77 °F] over an aqueous solution saturated with NaCl, NaNO<sub>3</sub>, or both. Consider, for instance, a dry mixture of NaCl and NaNO<sub>3</sub> salts with bulk composition  $x_A$ . If the ambient relative humidity, initially below the mutual deliquescence relative humidity, is increased, no significant uptake of water by the salt mixture occurs until the mutual deliquescence relative humidity is reached. At the mutual deliquescence relative humidity, deliquescence occurs, and the salt mixture dissolves—NaCl completely and NaNO<sub>3</sub> partially. As the ambient relative humidity is raised further, the amount of solid decreases, and the amount of liquid increases, with the liquid becoming richer in dissolved NaNO<sub>3</sub> relative to dissolved NaCl. At a relative humidity slightly higher than  $RH_A$ , the NaNO<sub>3</sub> solid is dissolved completely and the aqueous composition will have changed from  $x_C$  at the mutual deliquescent relative humidity to  $x_A$ . Raising the ambient relative humidity further will cause the aqueous phase to be diluted. Likewise, for a mixture of NaCl and NaNO<sub>3</sub> having a bulk composition of  $x_B$ , the salt mixture dissolves at the mutual deliquescence relative humidity—NaCl partially and NaNO<sub>3</sub> completely. As the ambient relative humidity is raised above the mutual deliquescence relative humidity, the aqueous phase becomes richer in

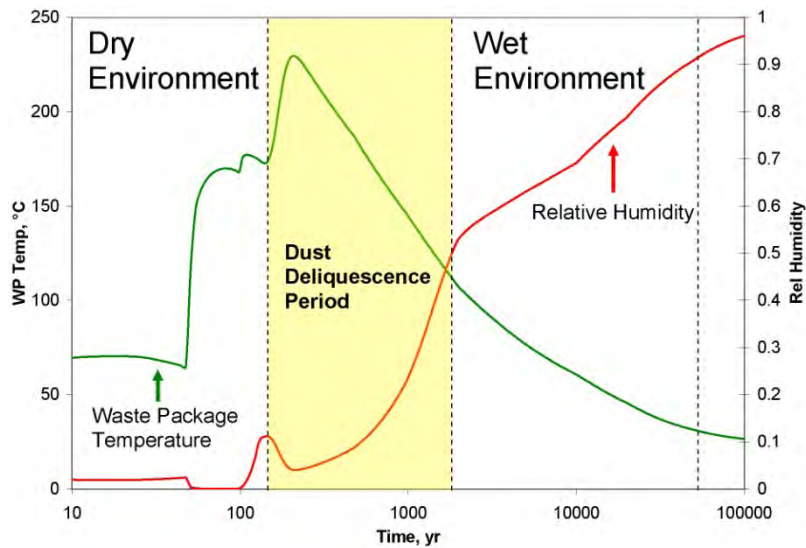


**Figure 2-1. Plot of Calculated Waste Package Temperature and Relative Humidity at the Potential Yucca Mountain Repository (Pensado, 2006). The Temperature and Relative Humidity Are Kept Low by Ventilation During the Preclosure Period (Assumed to be 50 Years).**

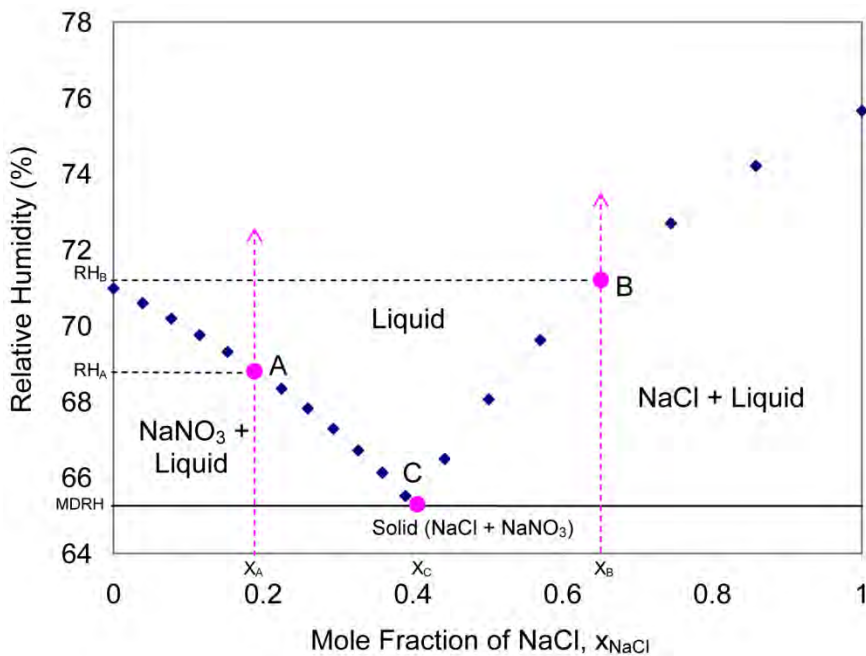


**Figure 2-2. Calculated Relative Humidity at 25 °C [77 °F] Over an Aqueous Solution Saturated With Either NaCl, NaNO<sub>3</sub>, or Both as a Function of Salt Mixture Composition.  $x_c$  is the Eutonic Composition of the NaCl–NaNO<sub>3</sub> Mixture.**

dissolved NaCl relative to dissolved NaNO<sub>3</sub> until NaCl is dissolved completely at RH<sub>B</sub>. A salt mixture with bulk composition  $x_C$  will dissolve completely when the ambient relative humidity is raised to values at or above the mutual deliquescence relative humidity.

The deliquescence relative humidity of salts and the mutual deliquescence relative humidity of salt mixtures depend on composition. Figure 2-3 shows the calculated deliquescence relative humidity and mutual deliquescence relative humidity for salts and salt mixtures in the system NaCl–KCl–MgCl<sub>2</sub> at 90 °C [194 °C]. The deliquescence relative humidity for the single salts NaCl, KCl, and MgCl<sub>2</sub> are 74.3, 76.2, and 24.7 percent, respectively. For the mixture of NaCl and KCl, which both have relatively high deliquescence relative humidity, the depression of the deliquescence point due to the other salt is not large (less than 10 percent relative humidity). In contrast, the deliquescence point of NaCl or KCl is substantially reduced when mixed with MgCl<sub>2</sub>, and the mutual deliquescence relative humidity is lowest (24.2 percent) when the brine is saturated with the three salts NaCl (halite), MgCl<sub>2</sub>·6H<sub>2</sub>O (bishofite), and KMgCl<sub>3</sub>·6H<sub>2</sub>O (carnallite).

The deliquescence relative humidity of salts and the mutual deliquescence relative humidity of salt mixtures also depend on temperature. Figure 2-4 shows the calculated deliquescence relative humidity as a function of temperature of different salts and salt mixtures in the system Na–K–Cl–NO<sub>3</sub>. The NaCl–NaNO<sub>3</sub>–KNO<sub>3</sub> salt mixture is important because it has low deliquescence relative humidity and the U.S. Department of Energy (DOE) considers it to be a salt assemblage that could control the deliquescence of dusts deposited inside the drift of the potential Yucca Mountain repository (Bechtel SAIC Company, LLC, 2005). DOE experiments suggest that NaCl–NaNO<sub>3</sub>–KNO<sub>3</sub> brines can form at temperatures exceeding 190 °C [374 °F] (Bechtel SAIC Company, LLC, 2005).

## **2.2 Characterization Data on Dusts Sampled From Yucca Mountain and Vicinity**

DOE sampled dusts on the surface of Yucca Mountain, in the Yucca Mountain tunnels, and at remote locations near the Yucca Mountain site {within 20 mi [32 km]}. These dusts provided mineralogical, geochemical, and leachate data that contributed to an analysis of the potential effect of dust deliquescence brines on the localized corrosion of the Alloy 22 waste package outer container (Bechtel SAIC Company, LLC, 2005).

### **2.2.1 Yucca Mountain Crest Data**

The U.S. Geological Survey staff collected samples from the ground surface of the Yucca Mountain crest {approximately 1,494 m [4,900 ft] elevation} in June 2004 on the lee of large rocks and bushes and from bedrock depressions (Peterman, 2006). These samples were collected using a brush and a collection tray and then were transferred to a sample bottle. Approximately 200 g [7 oz] of these samples were collected, and 10-g [0.4-oz] splits of these samples were provided to the Center for Nuclear Waste Regulatory Analyses (CNWRA<sup>®</sup>) for replicate analysis. The dust leachate compositions analyzed by the CNWRA are listed in Table 2-1. DOE data on the split samples are reported in Bechtel SAIC Company, LLC (2007, 2004). The CNWRA data are for the leachates of the whole dust samples, whereas DOE analyses were conducted on leachates of sized fractions of the dust samples.

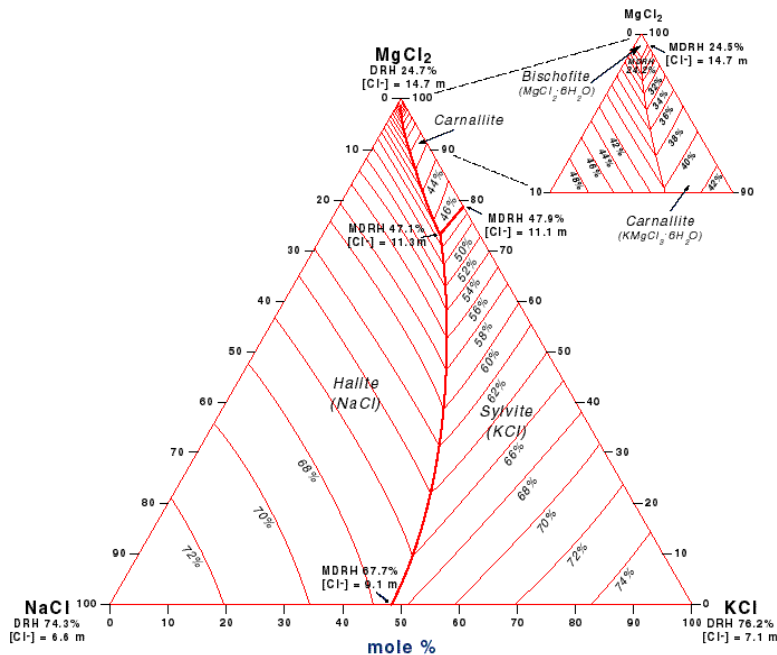


**Figure 2-3. Calculated Deliquescence Relative Humidity Shown as Contour Lines of Different Salts and Salt Mixtures in the System NaCl–KCl–MgCl<sub>2</sub> at 90 °C [194 °F]. The Solutions Are Saturated With the Indicated Salts. Also Shown for Some Compositions Is the Stoichiometric Chloride Concentration [Cl<sup>-</sup>] (moles/kg H<sub>2</sub>O) of the Saturated Solutions. Figure Taken From Pabalan, et al. (2002).**

As shown in Table 2-1, calcium is present in all samples in significant amounts as compared to sodium, and all samples show a nitrate-to-chloride molar ratio of less than 1. All samples have a very low relative amount (<0.1 percent) of soluble salts. The U.S. Geological Survey stated that samples taken from the Yucca Mountain crest were leached by rainfall and, therefore, had low amounts of soluble salts. CNWRA powder x-ray diffraction data on four surface samples (Table 2-2) indicated the presence of feldspars and quartz; one sample had calcite as a major phase.

### 2.2.2 Yucca Mountain Tunnel Data

The U.S. Geological Survey staff collected samples from inside the tunnel by vacuuming dust from tunnel walls and by trapping dust using a cyclone. Vacuuming several square meters of surface yielded 250 to 400 g [8.8 to 14 oz] of dust per sample (Peterman, 2006). Splits of samples collected in the Exploratory Studies Facility portion of the tunnel in February 2002 were provided to CNWRA for analysis. CNWRA data on dust leachate compositions are listed in Table 2-3. DOE data on the split samples are reported in Bechtel SAIC Company, LLC (2007, 2004). The CNWRA data are for leachates of whole dust samples, whereas DOE analyses were conducted on leachates of sized fractions of the dust samples. All tunnel samples showed close to 1 percent soluble material.

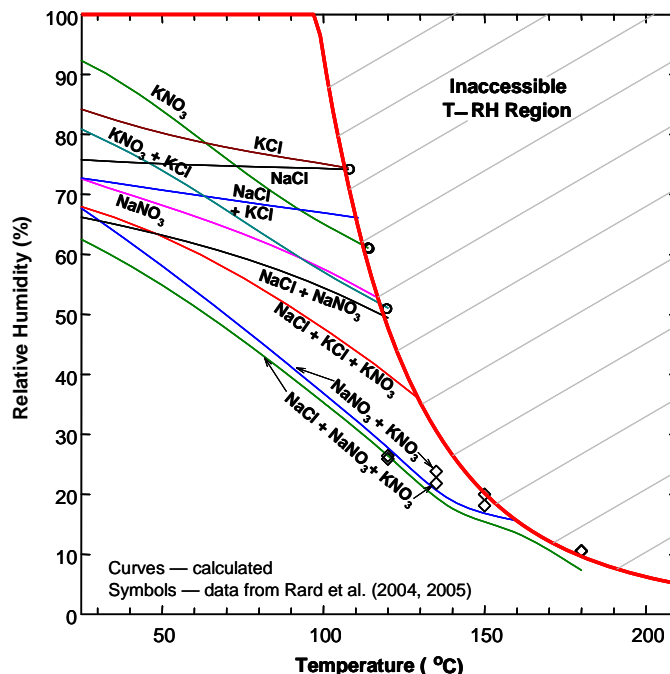


**Figure 2-4. Calculated Deliquescence Relative Humidity of Different Salts and Salt Mixtures in the System Na–K–Cl–NO<sub>3</sub> as a Function of Temperature. The Red Curve Is Calculated for a Total Pressure of 89 kPa [12.9 psi], Which Is the Approximate Atmospheric Pressure at the Elevation of Yucca Mountain. The Region Above the Red Curve Is Inaccessible (i.e., There Would Be No Film of Water on the Surface of the Engineered Barrier). The Symbols Represent Experimental Data From Rard (2005, 2004).**

Table 2-1. Center for Nuclear Waste Regulatory Analyses Data on the Composition of Leachates of Dusts Sampled From the Surface of Yucca Crest (mg/L)*											
Sample Number	Ca <sup>2+</sup>	Mg <sup>2+</sup>	K <sup>+</sup>	Na <sup>+</sup>	SiO <sub>2</sub>	Cl <sup>-</sup>	Br <sup>-</sup>	F <sup>-</sup>	NO <sub>3</sub> <sup>-</sup>	SO <sub>4</sub> <sup>2-</sup>	$\frac{NO_3}{Cl^-}$ Molar Ratio
030800	61.5	5.7	58.1	157.0	119.0	8.0	<1.49	2.6	10.2	33.5	0.73
030803	28.1	5.2	19.4	<14.9	64.7	4.2	<1.49	3.1	4.1	10.2	0.56
030805	76.0	12.3	55.7	15.1	63.1	7.9	<1.49	3.6	4.1	20.2	0.30
030807	83.5	12.7	161.0	38.4	49.5	52.4	<1.49	3.2	21.6	67.5	0.24

\*DOE data on split samples are reported in Bechtel SAIC Company, LLC. "Environment on the Surfaces of the Drip Shield and Waste Package Outer Barrier." ANL-EBS-MD-000001. Rev. 01. Las Vegas, Nevada: Bechtel SAIC Company, LLC. 2004.

Table 2-4 gives CNWRA x-ray diffraction data for the tunnel samples, each of which has feldspar and silica minerals as major components. Calcite is also a major phase in one sample.

### 2.2.3 Atmospheric (Cyclone) Dust Data

DOE collected atmospheric dust samples using a Torit<sup>®</sup> cyclone, which was located near the South Portal until its relocation to a different site in March 2007. The cyclone was set up to

Mineral	Sample Number			
	030800	030803	030805	030807
Albite, calcian, ordered (Na,Ca)Al(Si,Al) <sub>3</sub> Si <sub>3</sub> O <sub>8</sub>	Major		Major	
Albite, ordered NaAlSi <sub>3</sub> O <sub>8</sub>	Major	Minor	Major	Major
Anorthite, ordered CaAl <sub>2</sub> Si <sub>2</sub> O <sub>8</sub>	Major	—	—	—
Anorthoclase, disordered (Na,K)(Si <sub>3</sub> Al)O <sub>8</sub>	—	—	Major	Minor
Anorthite, sodian, disordered (Ca,Na)(Si,Al) <sub>4</sub> O <sub>8</sub>	—	—	—	Major
Calcite CaCO <sub>3</sub>	Major	—	—	—
Microcline, intermediate KAISi <sub>3</sub> O <sub>8</sub>	—	Major	Major	—
Augite, aluminian Ca(Mg,Fe <sup>3+</sup> , Al)(Si,Al) <sub>2</sub> O <sub>6</sub>	—	Minor	—	—
Diopside CaMg(SiO <sub>3</sub> ) <sub>2</sub>	—	Minor	—	—
Quartz SiO <sub>2</sub>	Major	Major	—	Major

Sample Number	Ca <sup>2+</sup>	Mg <sup>2+</sup>	K <sup>+</sup>	Na <sup>+</sup>	SiO <sub>2</sub>	Cl <sup>-</sup>	Br <sup>-</sup>	F <sup>-</sup>	NO <sub>3</sub> <sup>-</sup>	SO <sub>4</sub> <sup>2-</sup>	PO <sub>4</sub> <sup>3-</sup>	$\frac{\text{NO}_3^-}{\text{Cl}^-}$ Molar Ratio
574980	389	44.1	89.8	107	134	73.6	4.66	2.7	59.9	310	—	0.47
574982	737	104	196	518	95.2	178	12.5	13.5	176	926	—	0.57
574983	1010	98.5	253	710	60.6	364	15.7	20.2	194	1170	—	0.31
574987	1390	58.3	247	622	180	366	44.5	21	120	1510	—	0.19

\*DOE data on split samples are reported in the following references: (i) Bechtel SAIC Company, LLC. "Analysis of Dust Deliquescence for FEP Screening." ANL-EBS-MD-000074. Rev 01, Addendum 01. Las Vegas, Nevada: Bechtel SAIC Company, LLC. 2007; and (ii) Bechtel SAIC Company, LLC. "Environment on the Surfaces of the Drip Shield and Waste Package Outer Barrier." ANL-EBS-MD-000001. Rev 01. Las Vegas, Nevada: Bechtel SAIC Company, LLC. 2004.

Mineral	Sample Number			
	574980	574982	574983	574987
Albite, calcian, ordered (Na,Ca)Al(Si,Al) <sub>3</sub> Si <sub>3</sub> O <sub>8</sub>	Major	Major	—	—
Albite, ordered NaAlSi <sub>3</sub> O <sub>8</sub>	Major	—	Major	—
Anorthite, sodian, ordered (Ca,Na)(Al,Si) <sub>2</sub> Si <sub>2</sub> O <sub>8</sub>	—	—	Major	—
Anorthoclase, disordered (Na,K)(Si <sub>3</sub> Al)O <sub>8</sub>	—	Major	—	Major
Calcite CaCO <sub>3</sub>	—	—	—	Major
Cristobalite SiO <sub>2</sub>	Major	Major	Major	Major
Microcline, intermediate KAISi <sub>3</sub> O <sub>8</sub>	—	—	Major	Minor
Orthoclase KAISi <sub>3</sub> O <sub>8</sub>	—	Major	Major	Major
Stellerite Ca <sub>2</sub> Al <sub>4</sub> Si <sub>14</sub> O <sub>36</sub> -14H <sub>2</sub> O	—	—	Major	—
Quartz SiO <sub>2</sub>	Major	Major	Major	Major

exclude particles greater than  $0.5 \mu\text{m}$  [ $2 \times 10^{-5}$  in] in size. Sampling was conducted from June 2005 until March 2007 approximately monthly and yielded approximately 1.5 g [0.053 oz] per sample (Peterman, 2006), although the exact amounts collected are not available in published literature. Splits of samples collected between March 2006 and March 2007 were provided to CNWRA for analysis. CNWRA leachate data are given in Table 2-5. DOE data are reported in Bryan (2006) and Bechtel SAIC Company, LLC (2007). Soluble fractions in the samples provided to CNWRA ranged from 8 to 13 percent.

The CNWRA x-ray diffraction data listed in Table 2-6 indicate that all atmospheric samples contained calcite, quartz, and feldspars as major mineral components.

#### **2.2.4 Remote Dust Data**

The U.S. Geological Survey and the National Atmospheric Deposition Program have several dust sampling locations near the Yucca Mountain site. The dusts from these sampling locations are called remote dusts in this report. The remote dusts might be informative to the project, although they are not directly from the Yucca Mountain site. Remote dust sampling captured airborne dusts using specialized dust traps approximately 2 m [6.6 ft] above the ground surface, as Reheis (2003) described. The samples were collected semiannually, and the particular samples that the U.S. Geological Survey provided to CNWRA for analysis were collected in April 2004. Sample T3 was collected at a location a few miles north of Yucca Mountain, and T14 was collected in Crater Flat, west of the southern end of Yucca Mountain. These samples primarily contain dust from playas and alluvial fans in the area. Remote dusts contained approximately 10 percent soluble fraction based on CNWRA analyses. CNWRA analyses of the leachate of the combined T3 and T14 samples showed calcium as the primary cation (55 mole percent) and sulfate as the primary anion (69 mole percent), with sodium and chloride as the secondary cation and anion, respectively. The nitrate-to-chloride molar ratio of the combined T3 and T14 leachate sample is 0.81. For comparison, data for regional precipitation (rain out) in the same area taken from the National Atmospheric Deposition Program are given in Table 2-7.

The CNWRA x-ray diffraction analysis results for the remote samples T3 and T14 are listed in Table 2-8. The two remote samples have calcite, quartz, and feldspars as the major mineral components, similar to the other dust samples.

### **2.3 Potential Composition of Brines Formed by Deliquescence of Salts Present in Yucca Mountain Dusts**

A useful indicator of the composition of salts that may deliquesce and form brines on the surface of drip shields and waste packages at the potential repository is the composition of salts present in dusts sampled from Yucca Mountain. However, there is no direct information regarding the identity of salt minerals present in dust samples taken from Yucca Mountain and the vicinity. The dust samples generally have salt amounts too low for phase identification using powder x-ray diffraction analysis.

**Table 2-5. Center for Nuclear Waste Regulatory Analyses Data on the Composition of Leachates of Atmospheric Dusts Collected With the Torit Cyclone (mg/L)\***

Sample Number	Ca <sup>2+</sup>	Mg <sup>2+</sup>	K <sup>+</sup>	Na <sup>+</sup>	Si <sup>4+</sup>	Cl <sup>-</sup>	F <sup>-</sup>	NO <sub>3</sub> <sup>-</sup>	SO <sub>4</sub> <sup>2-</sup>	PO <sub>4</sub> <sup>3-</sup>	$\frac{NO_3^-}{Cl^-}$ Molar Ratio
1037535	4960	1110	1510	4750	160	1850	30.3	3790	6480	31.3	1.17
2043004	3940	835	1520	3280	203	1470	50.9	2610	4590	<8.31	1.02
2043008	6920	1440	3270	4770	408	1550	47.6	4830	7170	53.9	1.78
2043025	5750	1290	2210	5100	235	1510	38.7	5260	5960	11	1.99
2043027	4630	986	1700	3910	245	1620	39.4	3690	5040	11.3	1.30
2043031	4340	1150	2100	3490	260	1500	40.7	2970	4490	173	1.13
2043033	5330	1190	1720	5270	275	1290	41.9	4260	8210	49.4	1.89
2043037	3690	980	1410	4910	365	2860	21.3	2800	4770	17.6	0.56

\*DOE data on split samples are reported in the following references: (i) Bechtel SAIC Company, LLC. "Analysis of Dust Deliquescence for FEP Screening." ANL-EBS-MD-000074. Rev. 01, Addendum 01. Las Vegas, Nevada: Bechtel SAIC Company, LLC. 2007; and (ii) Bryan, C. "Evolution of Waste Package Environments in a Repository at Yucca Mountain." Nuclear Waste Technical Review Board Meeting, September 25-26, 2006, Las Vegas, Nevada. 2006. <<http://www.nwtrb.gov/meetings/2006/sept/bryan.pdf>>. (7 April 2008).

**Table 2-6. Mineralogical Composition of Atmospheric Samples Based on Center for Nuclear Waste Regulatory Analyses Powder X-Ray Diffraction Analysis**

Mineral	Sample Number							
	1037535	2043004	2043008	2043025	2043027	2043031	2043033	2043037
Albite, calcian, ordered (Na,Ca)Al(Si,Al) <sub>3</sub> Si <sub>3</sub> O <sub>8</sub>	Major	Major	—	Major	Major	Major	Major	Major
Albite, ordered NaAlSi <sub>3</sub> O <sub>8</sub>	Major	—	Major	Major	Major	Major	Major	Major
Anorthite, sodian, ordered (Ca,Na)(Al,Si) <sub>2</sub> Si <sub>2</sub> O <sub>8</sub>	—	—	Major	Major	—	—	Major	—
Anorthite, sodian, intermediate (Ca,Na)(Si,Al) <sub>4</sub> O <sub>8</sub>	Minor	—	—	—	—	Minor	—	—
Anorthoclase, disordered (Na,K)(Si <sub>3</sub> Al)O <sub>8</sub>	—	—	—	—	—	—	—	Major
Calcite CaCO <sub>3</sub>	Major	Major	Major	Major	Major	Major	Major	Major
Cristobalite SiO <sub>2</sub>	Minor	—	—	—	—	—	—	—
Anorthite ordered CaAl <sub>2</sub> Si <sub>2</sub> O <sub>8</sub>	—	Major	—	—	—	—	—	—
Gismondine CaAl <sub>2</sub> Si <sub>2</sub> O <sub>8</sub> -4H <sub>2</sub> O	—	Major	Major	—	—	—	—	—
Quartz SiO <sub>2</sub>	Major	Major	Major	Major	Major	Major	Major	Major

<b>Sample Number</b>	<b>Ca<sup>2+</sup></b>	<b>Mg<sup>2+</sup></b>	<b>K<sup>+</sup></b>	<b>Na<sup>+</sup></b>	<b>NO<sub>3</sub><sup>-</sup></b>	<b>Cl<sup>-</sup></b>	<b>SO<sub>4</sub><sup>2-</sup></b>	<b><math>\frac{NO_3^-}{Cl^-}</math> Molar Ratio</b>
NV00-2002	0.48	0.044	0.013	0.059	1.14	0.09	0.46	7.3
NV00-2001	0.66	0.068	0.042	0.133	2.15	0.16	1.01	7.7
NV00-2000	1.21	0.137	0.055	0.263	3.24	0.36	1.35	5.2

<b>Mineral</b>	<b>Sample Number</b>	
	<b>T3</b>	<b>T14</b>
Albite, calcian, ordered (Na,Ca)Al(Si,Al) <sub>3</sub> Si <sub>3</sub> O <sub>8</sub>	Major	Major
Albite, ordered NaAlSi <sub>3</sub> O <sub>8</sub>	Major	Major
Anorthite ordered CaAl <sub>2</sub> Si <sub>2</sub> O <sub>8</sub>	Major	Major
Anorthite, sodian, intermediate (Ca,Na)(Si,Al) <sub>4</sub> O <sub>8</sub>		Minor
Calcite CaCO <sub>3</sub>	Major	Major
Halite NaCl	Minor	
Quartz SiO <sub>2</sub>	Major	Major

Thermodynamic simulations of the evaporation of dust leachates were conducted using StreamAnalyzer Version 2.0 (Gerbino, 2006). The software can be used to simulate aqueous chemical systems for temperatures up to 300 °C [572 °F], pressures up to 150 bar [2,205 psi], and ionic strengths as high as 30 molal. Higher ionic strengths—up to pure molten salts or pure acids—can be simulated with the software using a mixed-solvent electrolyte model (Wang, et al., 2002). Salt solubilities and aqueous solution water activities calculated using the mixed-solvent electrolyte model are consistent with experimental data (Gruskiewicz, et al., 2007), including those that Rard (2005, 2004) recently reported for the systems that contain NaCl, KNO<sub>3</sub>, and NaNO<sub>3</sub>. This latter model was applied in the calculations reported here to enable the evaporation simulations to extend to dry out conditions. The dust leachate compositions used as input to the StreamAnalyzer calculations were taken from Bechtel SAIC Company, LLC. (2004) and are tabulated in Table 2-9.

The StreamAnalyzer evaporation simulations yielded six potential deliquescent salt assemblages, which are listed in Table 2-10. More than 80 percent of the dust leachate compositions resulted in either NaCl–KNO<sub>3</sub> or NaCl–NaNO<sub>3</sub>–KNO<sub>3</sub> salt mixtures. The dominant salt assemblages are NaCl–KNO<sub>3</sub> and NaCl–NaNO<sub>3</sub>–KNO<sub>3</sub> (neglecting KBr), and an infrequent salt assemblage resulting from the evaporation simulations includes a calcium nitrate salt. Note that nondeliquescent solid phases also are present in the mineral assemblage. For example, Figure 2-5 illustrates the mineral phases—deliquescent and nondeliquescent—that form upon evaporation of six dust leachate samples.

**Table 2-9. Composition of Leachable Portion of Dust Samples Taken From Yucca Mountain Tunnels\***

Laboratory Sample Number	Ca <sup>2+</sup>	Mg <sup>2+</sup>	Na <sup>+</sup>	K <sup>+</sup>	Si <sup>4+</sup>	Cl <sup>-</sup>	F <sup>-</sup>	NO <sub>3</sub> <sup>-</sup>	so <sub>4</sub> <sup>2-</sup>	Br <sup>-</sup>
	ppm	ppm	ppm	ppm	ppm	ppm	ppm	ppm	ppm	ppm
C-186098	268	26.7	346	126	34.5	184	10	240	360	38
C-186091	980	83.6	358	183	43.5	182	6	800	1,120	10
C-186099	392	42	344	149	27.9	196	8	280	480	28
C-186092	638	79.7	431	193	46.6	180	6	580	980	22
C-186093	332	35.7	386	128	14.9	240	10	280	340	54
C-186100	630	31.4	389	150	82.5	220	40	260	640	64
C-186094	974	79.1	617	260	58.7	300	8	680	1,340	26
C-186101	229	18.9	262	101	42.3	220	8	114	300	28
C-186102	543	9.76	158	80	97.5	114	18	62	320	22
C-186095	575	34.3	415	206	94.9	200	14	400	660	26
C-186096	394	53.4	511	237	65	260	32	420	1,020	34
C-186097	480	34.8	287	142	61.2	160	8	380	620	18
C-186090	226	10.6	157	101	79.1	56	4	82	162	6
C-186089	635	43.6	397	214	100	200	24	420	720	22
C-186088	439	13.7	345	479	120	114	12	300	400	16
C-186087	919	32.8	332	221	96.4	140	18	440	1,180	20
C-186086	893	35.7	374	248	107	130	12	400	1,480	26
C-186085	863	25.9	369	220	134	162	12	380	740	22
C-186084	939	27.1	343	219	121	130	12	380	1,160	24
C-186082	630	28.3	388	231	95.1	154	10	340	1,060	50
C-186081	941	6.32	378	242	213	200	30	340	840	56
C-186080	430	19.4	304	221	89.2	162	24	220	640	34
C-186077	2,490	12.8	455	350	173	260	8	1,820	2,200	14
C-203112	147	16.3	55.4	159	161	<24	8	<7	<32	<1.6
C-203113	91.7	9.47	46.4	127	96.5	<24	4	10	<32	<1.6
C-203114	119	12.6	66	174	144	<24	8	24	<32	<1.6
C-203115†	270	34.3	115	193	169	76	18	220	220	<1.6
C-203116†	466	49.3	124	181	76.6	98	4	400	360	4
C-203117†	1,080	80.1	195	206	176	154	12	640	840	8
C-203118	772	44.1	188	280	33.4	74	8	116	3,800	4
C-203119	1,060	39.5	471	389	287	280	22	360	1,000	44
C-203120	2,340	130	392	389	42.8	320	8	1,760	4,600	6
C-203121†	246	39.6	262	196	164	86	20	240	320	4
C-203122†	458	64.1	339	244	51.6	118	4	520	520	6
C-203123†	1,010	99.6	556	345	99.2	170	6	1,000	1,060	12
C-203124†	262	23.7	296	281	94.9	114	12	198	380	8
C-203125†	770	50.8	425	303	57.3	260	4	540	720	10
C-203126†	1,240	85.9	666	369	62.7	360	10	980	1,200	10

**Table 2-9. Composition of Leachable Portion of Dust Samples Taken From Yucca Mountain Tunnels\* (continued)**

Laboratory Sample Number	Ca <sup>2+</sup>	Mg <sup>2+</sup>	Na <sup>+</sup>	K <sup>+</sup>	Si <sup>4+</sup>	Cl <sup>-</sup>	F <sup>-</sup>	NO <sub>3</sub> <sup>-</sup>	so <sub>4</sub> <sup>2-</sup>	Br <sup>-</sup>
	ppm	ppm	ppm	ppm	ppm	ppm	ppm	ppm	ppm	ppm
C-203127	335	49.4	265	339	87.3	128	10	220	440	10
C-203130	994	65.4	349	303	248	170	18	340	880	20
C-203131	1,260	52.4	461	333	181	168	22	480	1,180	14
C-203132	1,030	54.7	480	275	130	166	22	500	1,220	16
C-203133	248	23.4	222	234	75.4	96	6	146	320	6
C-203134	806	38	292	220	131	170	12	300	740	10
C-203135	1,190	51.4	408	260	159	220	18	440	1,140	14
C-203136†	1,290	84.6	201	257	21.8	188	8	600	5,800	2
C-203137†	1,180	64.1	564	313	135	360	22	540	1,400	42
C-203138†	1,280	70.5	570	288	143	320	24	520	1,480	32
C-203139	274	19.8	149	186	44.7	88	8	170	500	10
C-203140	434	25.9	186	151	38.9	102	6	220	760	16
C-203141	689	34.7	370	251	82.2	136	14	300	940	22
C-203142	281	55.4	128	139	161	88	22	122	440	12
C-203143	319	56.8	121	114	79.4	76	4	156	520	10
C-203144	622	53.6	196	177	215	82	10	164	700	12
C-203145	122	10.3	171	155	57.4	98	8	70	116	6
C-203146	110	9.48	126	121	12.3	82	2	68	124	<1.6
C-203147	305	19.8	187	173	60.2	166	6	150	280	2

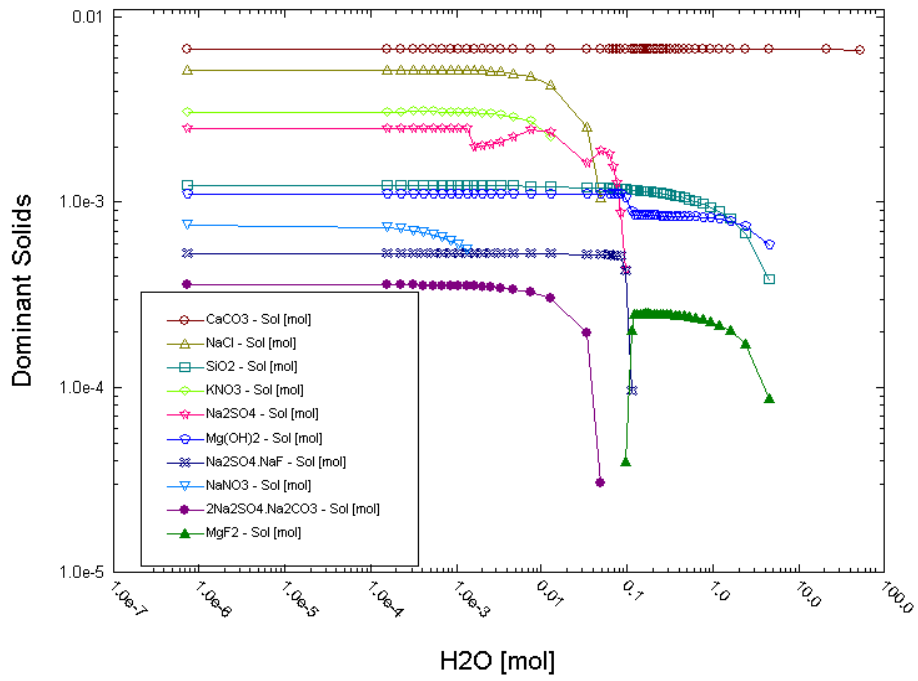
\*Values for phosphate, arsenic, and lead are reported also in Bechtel SAIC Company, LLC. "Environment on the Surfaces of the Drip Shield and Waste Package Outer Barrier." ANL-EBS-MD-000001. Rev. 01. Las Vegas, Nevada: Bechtel SAIC Company, LLC. 2004. However, these are not included in the evaporation simulations. Where "<x" values are listed, x is used as input in the StreamAnalyzer calculations.

†The laboratory sample numbers identified in this table correspond to the following field sample numbers tabulated in Table 2-3: C-203115 (574980A), C-203116 (574980B), C-203117 (574980C), C-203121(574982A), C-203122 (574982B), C-203123 (574982C), C-203124 (574983A), C-203125 (574983B), C-203126 (574983C), C-203136 (574987A), C-203137 (574987B), C-203138 (574987C).

**Table 2-10. Salt Assemblages Derived From Evaporation of Dust Leachates With Compositions Listed in Table 2-9. The Evaporation Was Simulated Using StreamAnalyzer Version 2.0.**

Salt Assemblage	Total Percentage of Occurrence	Sample Number of Representative Leachate Composition
NaCl-NaNO <sub>3</sub> -KNO <sub>3</sub>	43.9	C-186098
NaCl-KNO <sub>3</sub>	40.3	C-186101
KCl-KNO <sub>3</sub>	5.3	C-203112
NaCl-KCl-KNO <sub>3</sub>	5.3	C-186088
NaCl-NaNO <sub>3</sub> -Ca(NO <sub>3</sub> ) <sub>2</sub> -Ca(NO <sub>3</sub> ) <sub>2</sub> ·4KNO <sub>3</sub>	3.5	C-203120
NaCl-NaNO <sub>3</sub> -KNO <sub>3</sub> -Ca(NO <sub>3</sub> ) <sub>2</sub> ·4KNO <sub>3</sub>	1.7	C-203117

C-186098



C-186101

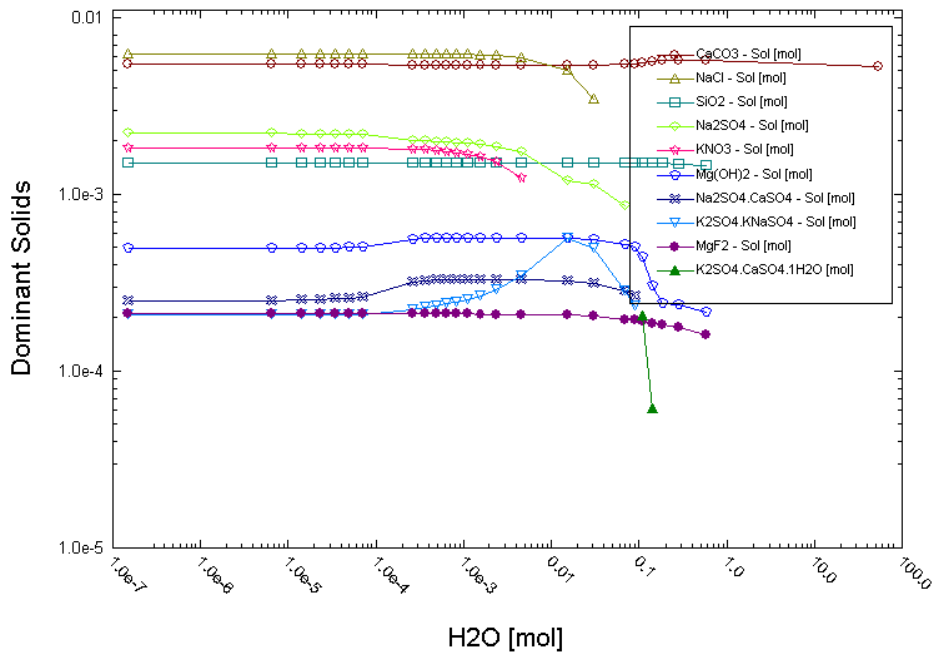
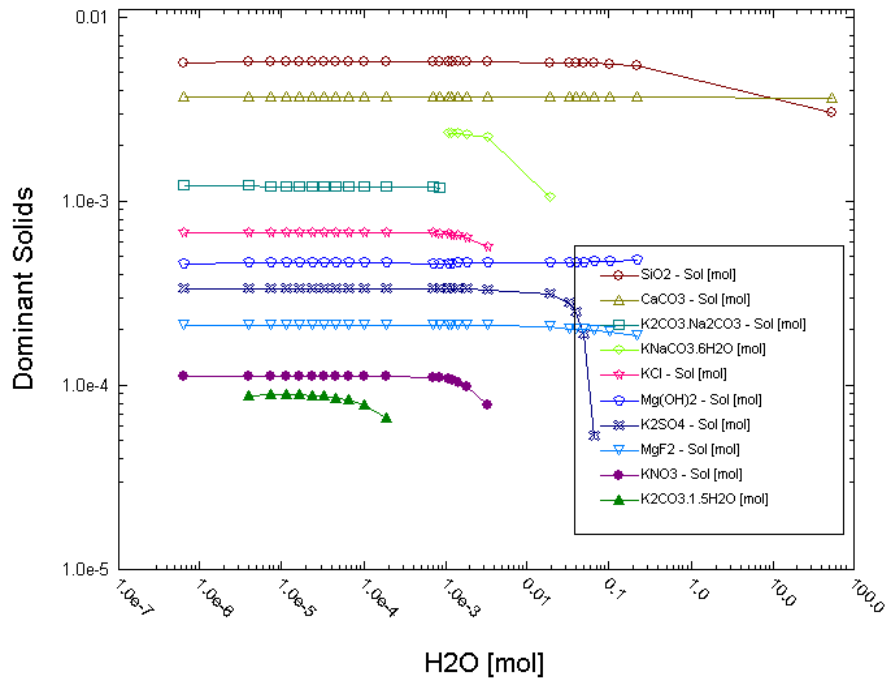


Figure 2-5. Mineral Precipitates Calculated to Form Upon Evaporation of Initially Dilute Dust Leachates. Decreasing Amount of H<sub>2</sub>O (Leftward on the X-Axis) Corresponds to Increasing Degree of Evaporation.

C-203112



C-186088

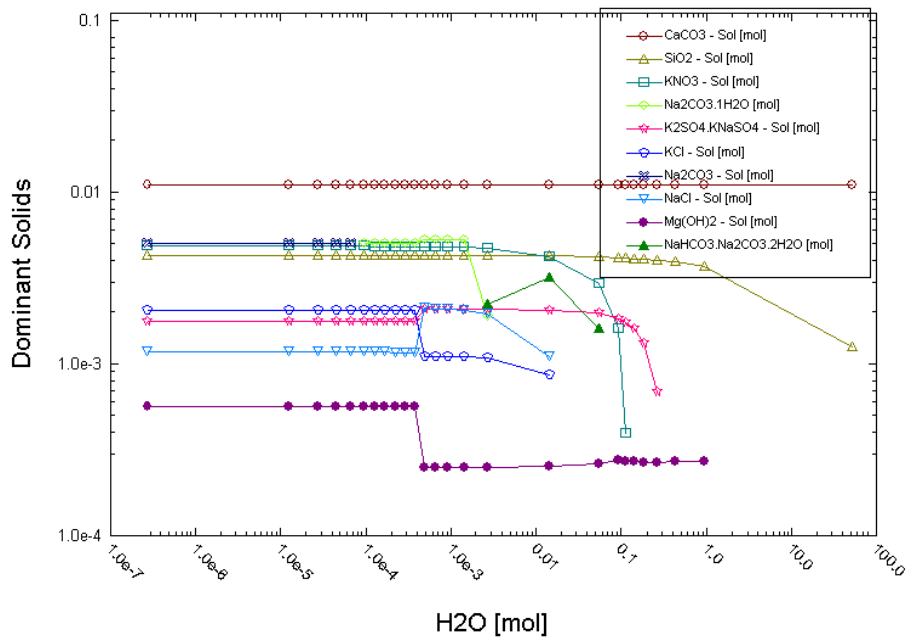
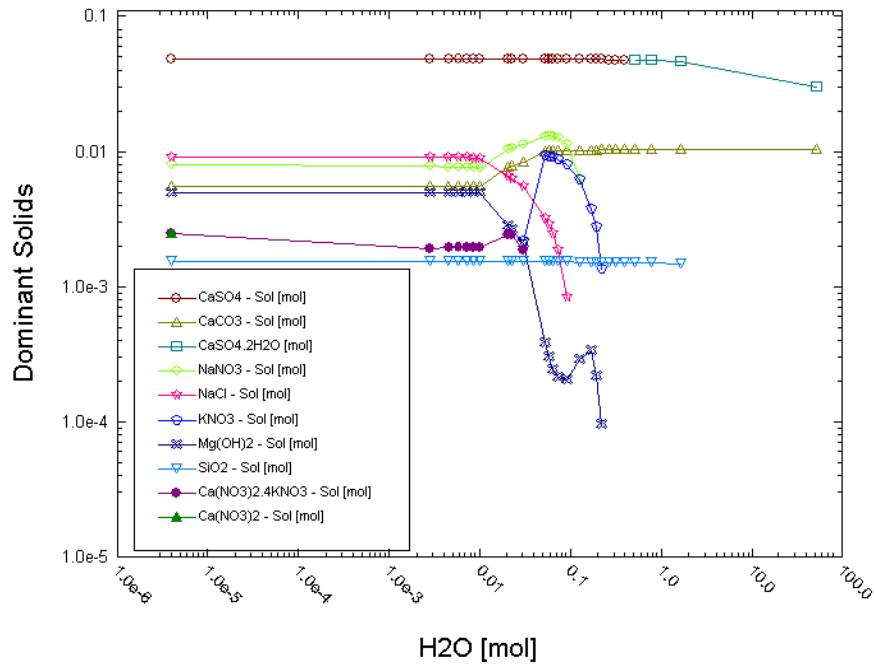


Figure 2-5. Mineral Precipitates Calculated to Form Upon Evaporation of Initially Dilute Dust Leachates. Decreasing Amount of H<sub>2</sub>O (Leftward on the X-Axis) Corresponds to Increasing Degree of Evaporation. (continued)

C-203120



C-203117

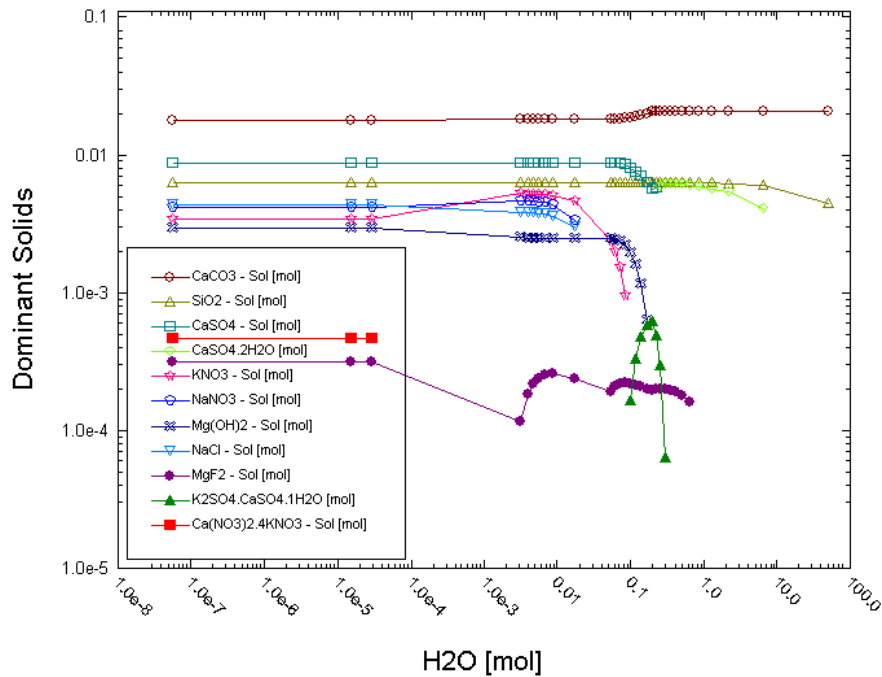


Figure 2-5. Mineral Precipitates Calculated to Form Upon Evaporation of Initially Dilute Dust Leachates. Decreasing Amount of H<sub>2</sub>O (Leftward on the X-Axis) Corresponds to Increasing Degree of Evaporation. (continued)

To determine whether the resulting mineral assemblages can deliquesce and form brines at elevated temperatures, their mutual deliquescence relative humidity was calculated as a function of temperature using StreamAnalyzer. Not all 57 mineral assemblages derived from the evaporation simulations were used in this analysis. Instead, each key salt assemblage was represented by one leachate sample, as identified in Table 2-10. The mutual deliquescence relative humidity of each sample was derived by running isothermal, bubble point StreamAnalyzer calculations, incrementally adding small amounts of water to the system until an aqueous phase is first formed. The resulting activity of water when an aqueous phase first forms is taken as the mutual deliquescence relative humidity of the salt assemblage.

The calculated mutual deliquescence relative humidity as a function of temperature for the six representative samples is listed in Table 2-11. The tabulated values indicate that all the resulting salt assemblages have very low deliquescence points, particularly at temperatures above 100 °C [212 °F]. To place the calculated mutual deliquescence relative humidity into perspective, those values can be compared to the in-drift relative humidity predicted for the potential Yucca Mountain repository, which are shown in Figure 2-1. A comparison of the mutual deliquescence relative humidity listed in Table 2-11 and the relative humidity in Figure 2-1 indicates that brines can potentially form on the waste package surface by deliquescence of salts when the waste package is relatively hot (>100 °C [>212 °F]).

The potential for these deliquescence brines to initiate localized corrosion will depend on the ratio of the molar concentration of chloride to corrosion-inhibiting oxyanions (nitrate, sulfate, bicarbonate, and carbonate), relative humidity, and temperature (Dunn, et al., 2005). The compositions of the deliquescence brines at the mutual deliquescence relative humidity of the salt assemblages were derived from the output file of the StreamAnalyzer runs described in the preceding paragraphs. Table 2-12 lists the calculated chloride-to-nitrate molar ratios for the six key salt assemblages that may deliquesce at temperatures above 100 °C [212 °F] at ambient pressure. When the temperature is at or above 120 °C [248 °F], the calculated chloride-to-nitrate ratios of these deliquescence brines are low—less than 0.2 (or higher than 5 for the nitrate-to-chloride ratios) under environmental conditions in which deliquescence brine-induced corrosion could occur (Figure 2-1). When the temperature is below 120 °C [248 °F] and above the normal boiling temperature, the calculated chloride-to-nitrate ratio for the KCl–KNO<sub>3</sub> salt assemblage (represented by sample C–203112) is high—13 to 18 [0.077 to 0.056] for the nitrate-to-chloride ratio. But the brine formed by deliquescence of this salt assemblage would have a ratio of chloride to localized corrosion inhibitors (nitrate + sulfate + bicarbonate + carbonate) less than 0.3 (or 3.6 for the inhibiting anions-to-chloride molar ratio).

Figure 2-6 shows the calculated evolution of the brine chloride-to-nitrate molar ratio as more water is taken up by the salt assemblages at a temperature of 110 °C [230 °F]. The chloride-to-nitrate molar ratio initially remains constant as water is added and the soluble nitrate salts dissolve, but the ratio subsequently increases as the less soluble chloride salts start to dissolve. With further increases in the amount of water, the nitrate and chloride salts completely dissolve and the chloride-to-nitrate molar ratio becomes constant. Note that this report is concerned only with the chloride-to-nitrate molar ratio near the mutual deliquescence relative humidity because dilute solutions would occur only after the temperature has dropped below boiling points and the relative humidity has increased above the corresponding deliquescence relative humidity.

**Table 2-11. Calculated Mutual Deliquescence Relative Humidity Percent As a Function of Temperature of Six Samples Representing Six Key Salt Assemblages\***

Temp (°C)	Sample Number					
	C-186098	C-186101	C-203112	C-186088	C-203120	C-203117
25	64.4	65.1	70.6	65.0	4.5	37.5
30	63.2	63.8	67.4	64.7	5.1	38.2
40	60.0	61.0	57.2	63.5	6.4	39.1
50	55.9	57.8	56.7	61.7	7.7	39.3
60	51.3	54.2	56.1	59.2	9.0	38.8
70	47.6	50.2	55.3	56.3	10.2	37.6
80	43.7	45.9	54.4	53.1	11.1	35.8
90	39.6	41.5	52.9	49.7	11.7	33.4
100	35.4	36.8	51.2	46.0	12.1	30.6
110	31.1	32.0	49.2	42.2	12.2	27.4
120	26.7	27.0	47.1	38.1	12.4	23.9
130	22.3	22.3	44.8	33.9	12.5	20.0
140	18.3	18.3	42.4	29.5	12.5	16.4
150	17.3	17.2	39.8	25.0	12.2	15.7

\*Each sample number represents a key salt assemblage:  
C-186098: NaCl-NaNO<sub>3</sub>-KNO<sub>3</sub>  
C-186101: NaCl-KNO<sub>3</sub>  
C-203112: KCl-KNO<sub>3</sub>  
C-186088: NaCl-KCl-KNO<sub>3</sub>  
C-203120: NaCl-NaNO<sub>3</sub>-Ca(NO<sub>3</sub>)<sub>2</sub>- Ca(NO<sub>3</sub>)<sub>2</sub>·4KNO<sub>3</sub>  
C-203117: NaCl-NaNO<sub>3</sub>-KNO<sub>3</sub>- Ca(NO<sub>3</sub>)<sub>2</sub>·4KNO<sub>3</sub>

The results of these analyses suggest that deliquescence brines could form on the waste package surface at elevated temperatures. However, at temperatures at or above 120 °C [248 °F], the nitrate-to-chloride molar ratio of the brines are expected to be high (>5) under the potential drift conditions during the deliquescence period. The high nitrate-to-chloride molar ratios are consistent with the values Felker, et al. (2006) reported. At temperatures between 100 and 120 °C [212 and 248 °F], the nitrate-to-chloride ratio may be low (less than 0.1), but the ratio of total inhibitors (nitrate + sulfate + bicarbonate + carbonate) to chloride is still higher than 3.3 for the KCl-KNO<sub>3</sub> salt assemblage.

Section 2.2 noted that the U.S. Geological Survey provided split samples of dusts sampled from Yucca Mountain to CNWRA for replicate chemical analysis and that DOE data on leachate compositions are reported by Bryan (2006) and Bechtel SAIC Company, LLC (2007, 2004). To determine whether the CNWRA leachate data would yield different salt assemblages compared to DOE leachate compositions, additional StreamAnalyzer evaporation simulations were conducted. The CNWRA leachate data for Yucca Mountain tunnel samples 574980, 574982, 574983, and 574987 listed in Table 2-3 were used as input to the calculations, which all yielded the salt assemblage NaCl-KNO<sub>3</sub>. This assemblage is consistent with the simulation results for DOE leachate samples C-203115, C-203121, and C-203136, but not for samples C-203116, C-203122, C-203123, C-203124, C-203125, C-203126, C-203137, and C-203138, which resulted in an NaCl-NaNO<sub>3</sub>-KNO<sub>3</sub> assemblage, and sample C-203117, which yielded a salt

Table 2-12. Calculated Molar Concentration Ratio of Chloride-to-Nitrate Ions As a Function of Temperature of Six Samples Representing Six Key Salt Assemblages*						
Temp (°C)	Sample Number					
	C-186098	C-186101	C-203112	C-186088	C-203120	C-203117
25	0.56	0.60	0.15 (0.48)†	2.1	$2.59 \times 10^{-04}$	0.042
30	0.45	0.50	3.4 (0.37)	1.9	$3.24 \times 10^{-04}$	0.040
40	0.28	0.34	4.2 (0.15)	1.3	$4.82 \times 10^{-04}$	0.036
50	0.17	0.24	4.8 (0.19)	0.85	$6.77 \times 10^{-04}$	0.032
60	0.11	0.16	5.5 (0.22)	0.59	$9.13 \times 10^{-04}$	0.028
70	0.081	0.12	6.4 (0.25)	0.44	$1.19 \times 10^{-03}$	0.025
80	0.063	0.084	7.7 (0.28)	0.33	$1.53 \times 10^{-03}$	0.022
90	0.051	0.063	9.7 (0.28)	0.26	$1.94 \times 10^{-03}$	0.021
100	0.042	0.049	13 (0.28)	0.20	$2.44 \times 10^{-03}$	0.020
110	0.036	0.039	18 (0.27)	0.16	$3.07 \times 10^{-03}$	0.020
120	0.031	0.032	0.18 (0.18)	0.13	$3.87 \times 10^{-03}$	0.021
130	0.028	0.028	0.16 (0.15)	0.11	$4.89 \times 10^{-03}$	0.022
140	0.027	0.027	0.14 (0.14)	0.097	$6.17 \times 10^{-03}$	0.023
150	0.032	0.033	0.13 (0.13)	0.088	$7.75 \times 10^{-03}$	0.028

\*Each sample number represents a key salt assemblage:  
C-186098: NaCl-NaNO<sub>3</sub>-KNO<sub>3</sub>  
C-186101: NaCl-KNO<sub>3</sub>  
C-203112: KCl-KNO<sub>3</sub>  
C-186088: NaCl-KCl-KNO<sub>3</sub>  
C-203120: NaCl-NaNO<sub>3</sub>-Ca(NO<sub>3</sub>)<sub>2</sub>-Ca(NO<sub>3</sub>)<sub>2</sub>·4KNO<sub>3</sub>  
C-203117: NaCl-NaNO<sub>3</sub>-KNO<sub>3</sub>-Ca(NO<sub>3</sub>)<sub>2</sub>·4KNO<sub>3</sub>  
†Values in parentheses are the concentration ratios of Cl<sup>-</sup>/(NO<sub>3</sub><sup>-</sup>-SO<sub>4</sub><sup>2-</sup>-HCO<sub>3</sub><sup>-</sup>-CO<sub>3</sub><sup>2-</sup>)

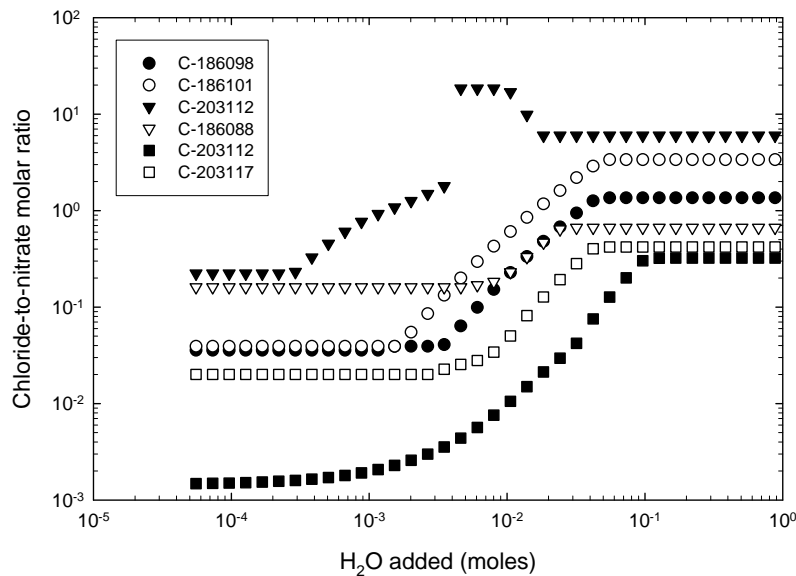


Figure 2-6. Evolution of the Nitrate-to-Chloride Molar Ratio as More Water Is Taken up by the Deliquescent Salt Assemblage at 110 °C [230 °F]

mixture of NaCl–NaNO<sub>3</sub>–KNO<sub>3</sub>– Ca(NO<sub>3</sub>)<sub>2</sub>·KNO<sub>3</sub>. Although the resulting salt assemblages based on the CNWRA leachate chemistry are generally different than those based on the DOE leachate data, the conclusion stated in the previous paragraph still holds true. This is because brines formed by deliquescence of a NaCl–KNO<sub>3</sub> salt mixture would have chloride-to-nitrate ratios much lower than the critical value that could lead to initiation of localized corrosion of Alloy 22.

## **2.4 Effect of Capillary Retention by Dusts on the Corrosivity of Deliquescence Brines**

The deliquescent salts that may deposit on the waste package surface likely would be mixed with nondeliquescent rock dusts produced during potential repository construction. A DOE numerical analysis indicates that rock dusts would retain by capillarity any brine formed by deliquescence, thereby limiting brine contact with and potential corrosion of the waste package (Bechtel SAIC Company, LLC, 2005). Experiments discussed in this section (i) evaluated the effect of capillary retention by dusts on the corrosivity of deliquescence brines and (ii) assessed Alloy 22 corrosion in brines formed by deliquescence of salts mixed with rock dusts.

### **2.4.1 Test Methods**

The experiments were conducted at 70 °C [158 °F] inside a chamber with controlled temperature and relative humidity using mixtures with varying mass ratios of NaCl to quartz or rock dust in contact with the metals of interest. Quartz powder, which was sieved to <250 μm [<0.01 in] and acid washed to remove soluble impurities, was used for comparison with the rock dust. Simulated rock dust was made by crushing specimens of Topopah Spring tuff, which is the potential repository host rock at Yucca Mountain, and by sieving the crushed material to <74 μm [<0.003 in]. To determine the composition of the soluble components of the rock dust, 5-g [0.18-oz] samples of the rock dust were leached in 50 mL [1.7 fluid oz] of deionized water at 25 and 70 °C [77 and 158 °F] for various durations. The leachates were analyzed for soluble composition using inductively coupled plasma emission spectrometry for cations and ion chromatography for anions. The leachate compositions, which are shown in Table 2-13, indicate that the soluble constituents of the rock dust are primarily sodium salts of chloride, fluoride, nitrate, and sulfate. The molar ratio of chloride and sulfate to chloride is less than or equal to 0.30. The charge imbalance between cations and anions shown in Table 2-13 could be due to analytical error and to the lack of data on carbonate species, which was not analyzed in this study.

The corrosivity of the deliquescence brines was monitored using coupled multielectrode array sensor probes (Yang, et al., 2002a). Each probe has 16 electrodes of the same material with a diameter of 1 mm [39 mil]. The electrode material was either carbon steel or Alloy 22. The carbon steel electrodes were used for their high sensitivity to the corrosivity of the brine. The deliquescent salts used were NaCl and a mixture of NaCl, KNO<sub>3</sub>, and NaNO<sub>3</sub>. Figure 2-7 shows the schematic of the test setup. The tests were conducted by setting four probes vertically in the humidity chamber. The salt-dust mixtures, each with a total mass of 10 g [0.35 oz], were placed inside Tygon<sup>®</sup> sleeves above the probes. The relative humidity inside the chamber was raised stepwise from 20 percent to above the deliquescence point of NaCl, which is 75 percent at 70 °C [158 °F] (Yang, et al., 2002b). Four tests were conducted at 70 °C [158 °F] using carbon steel probes and mixtures of NaCl–dust or NaCl–quartz. These four tests were designed to evaluate the effect of capillary retention by dusts on the corrosivity of deliquescence

Table 2-13. Chemical Compositions of Dust Leachate (ppm)							
Leaching Time (Days)	Cl <sup>-</sup>	F <sup>-</sup>	NO <sub>3</sub> <sup>-</sup>	SO <sub>4</sub> <sup>2-</sup>	Na <sup>+</sup>	Molar Ratio [Na <sup>+</sup> ]	Molar Ratio
						$\frac{[Cl^-] + [NO_3^-] + [F^-] + 2[SO_4^{2-}]}{[Cl^-]}$	$\frac{[NO_3^-] + [SO_4^{2-}]}{[Cl^-]}$
5	39.3	12	<2	18.4	376	8	0.19
12	37.8	13.2	<2	18.0	348	7	0.19
52	35.4	13.9	<2	17.5	352	7	0.20
Leaching at 70 °C [158 °F]							
5	55.4	19.6	12.0	19.0	407	6	0.25
14	39.3	20.5	9.08	18.4	413	7	0.30

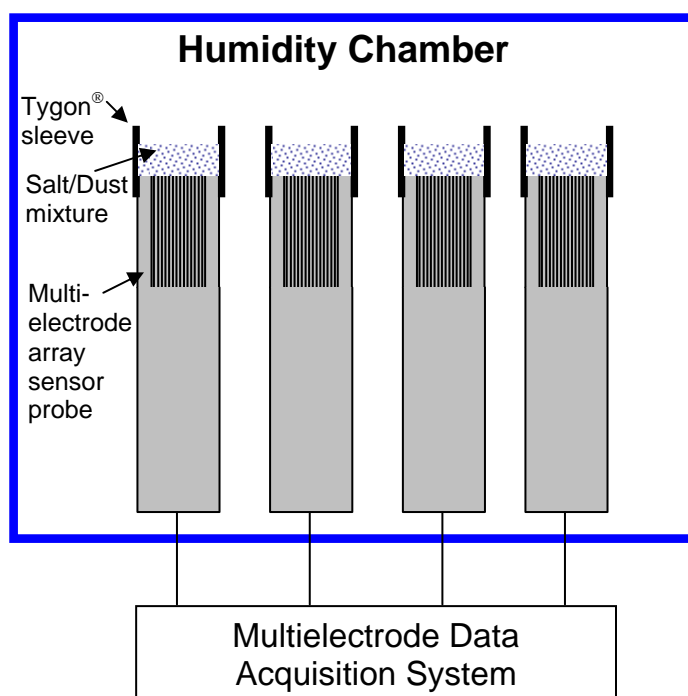


**Figure 2-7. Schematic of Test Setup Used in Studying the Effect of Capillary Retention by Dusts on the Corrosivity of Deliquescence Brines**

brines. An additional test was conducted at 125 °C [257 °F] using both Alloy 22 and carbon steel probes to assess the corrosion of Alloy 22 material relative to that of carbon steel in brines formed by the deliquescence of NaCl–KNO<sub>3</sub>–NaNO<sub>3</sub> salts mixed with rock dusts.

## 2.4.2 Test Results

### 2.4.2.1 Test 1—NaCl–Quartz Mixture at 70 °C [158 °F]

Figure 2-8 shows the maximum corrosion current measured from the four carbon steel probes at 70 °C [158 °F] with the following solid phase compositions: (i) 100 percent NaCl on Probe 1, (ii) 30 percent NaCl–70 percent quartz on Probe 2, (iii) 10 percent NaCl–90 percent quartz on

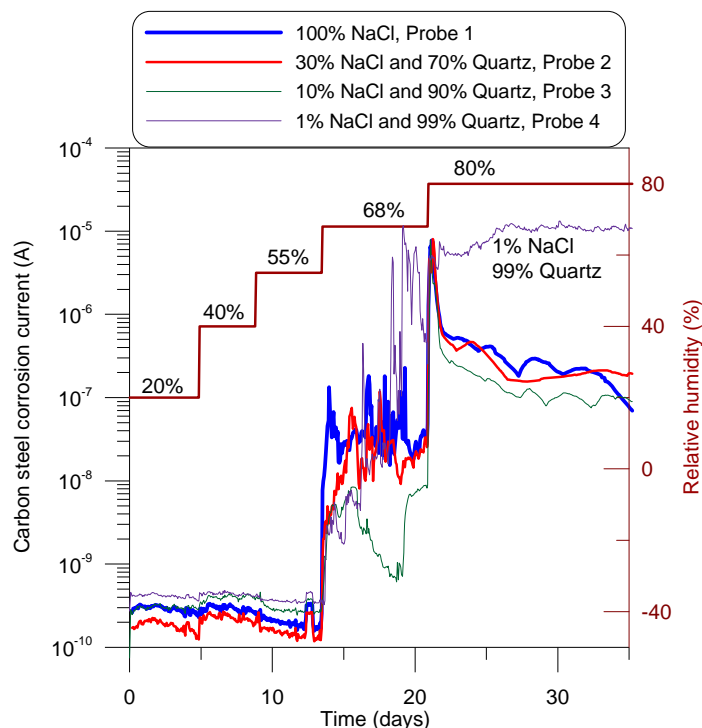


**Figure 2-8. Maximum Corrosion Current Measured From Test 1 Carbon Steel Probes. Test 1 Was Conducted at 70 °C [158 °F] With the Following Solid Phase Compositions: (i) 100 Percent NaCl on Probe 1, (ii) 30 Percent NaCl–70 Percent Quartz on Probe 2, (iii) 10 Percent NaCl–90 Percent Quartz on Probe 3, and (iv) 1 Percent NaCl–99 Percent Quartz on Probe 4.**

Probe 3, and (iv) 1 percent NaCl–99 percent quartz on Probe 4. The relative humidity was raised stepwise from 20 percent to 40 percent, 55 percent, 68 percent, and 80 percent.

At relative humidities of 20 percent, 40 percent, and 55 percent, the carbon steel corrosion current was below  $10^{-9}$  A, which is the background noise level, indicating that the system was dry at those relative humidities. However, at a relative humidity of 68 percent, which is below the deliquescence relative humidity of NaCl (75 percent), the corrosion currents increased by 1 to 2 orders of magnitude, which was probably due to the adsorption of water molecules on the salt crystals (Yang, et al., 2002b). At a relative humidity of 80 percent, brine was formed and overflowed from Probes 1, 2, and 3. At 80 percent relative humidity, the corrosion current from Probes 1, 2, and 3 decayed with time, whereas the corrosion current from Probe 4 remained high. The decrease in corrosion current observed for Probes 1, 2, and 3 was likely due to the brine solution slowing down oxygen transport and the salting out effect, which decreases the oxygen concentration in the solution. The brine solution was not present in Probe 4, so that oxygen transport was not a limiting factor for the carbon steel corrosion process. No significant difference was observed in the NaCl–quartz tests with 100, 30, and 10 percent NaCl (Probes 1, 2, and 3, respectively).

Figure 2-9 shows posttest photographs of the Test 1 carbon steel probes. Corrosion was evident on each carbon steel probe indicating brine contacted the metal surface, which is consistent with the observed corrosion current in Figure 2-8.



**Figure 2-9. Posttest Photographs of the Test 1 Carbon Steel Probes**

#### 2.4.2.2 Test 2—NaCl–Dust Mixture at 70 °C [158 °F]

Because no significant difference in corrosion current was observed in the NaCl–quartz tests with 100, 30, and 10 percent NaCl, the tests involving NaCl–dust mixtures used smaller relative amounts of NaCl. Figure 2-10(a) shows the maximum corrosion current measured from the four carbon steel probes with the following solid phase compositions: (i) 10 percent NaCl–90 percent dust on Probe 1, (ii) 1 percent NaCl–99 percent dust on Probe 2, (iii) 0.4 percent NaCl–99.6 percent dust on Probe 3, and (iv) 100 percent dust on Probe 4. The relative humidities used in the tests were the same as those in Test 1.

The results in Figure 2-10(a) show that the corrosion current increased above background level at a relative humidity of 55 percent, even for the probe with no salt added (100 percent dust), indicating an aqueous solution formed at a relative humidity of 55 percent. This relative humidity is much lower than the NaCl deliquescence point, and the brine formation might have been caused by the lowering of the deliquescence relative humidity by the small amount of nitrate in the dust (Table 2-13). The corrosion rate of carbon steel, which was calculated from the measured corrosion current by assuming uniform corrosion on each electrode, is shown in Figure 2-10(b). For all mixtures, including the mixture with a dust-to-NaCl weight ratio of 249 (Probe 3 with 0.4 percent NaCl–99.6 percent dust) and pure dust, the carbon steel corrosion rate increased above 1  $\mu\text{m}/\text{yr}$  [0.04 mil/yr] once relative humidity reached 55 percent. This result suggests the brine that formed by deliquescence at 55 percent relative humidity would be sufficient to support ionic transport on the carbon steel surface and the leachable salt in pure rock dust would be sufficient to initiate corrosion of carbon steel. At a relative humidity of 80 percent, the current decreased with time for Probes 2, 3, and 4. The small amount of nitrate present in the dust (Table 2-13) could have leached into the solution during the test and acted as a corrosion inhibitor, causing the observed decrease in corrosion current.

Figure 2-11 shows posttest photographs of the probes. No visible liquid formed even at a relative humidity of 80 percent, but the solid mixtures were damp, indicating absorption of liquid

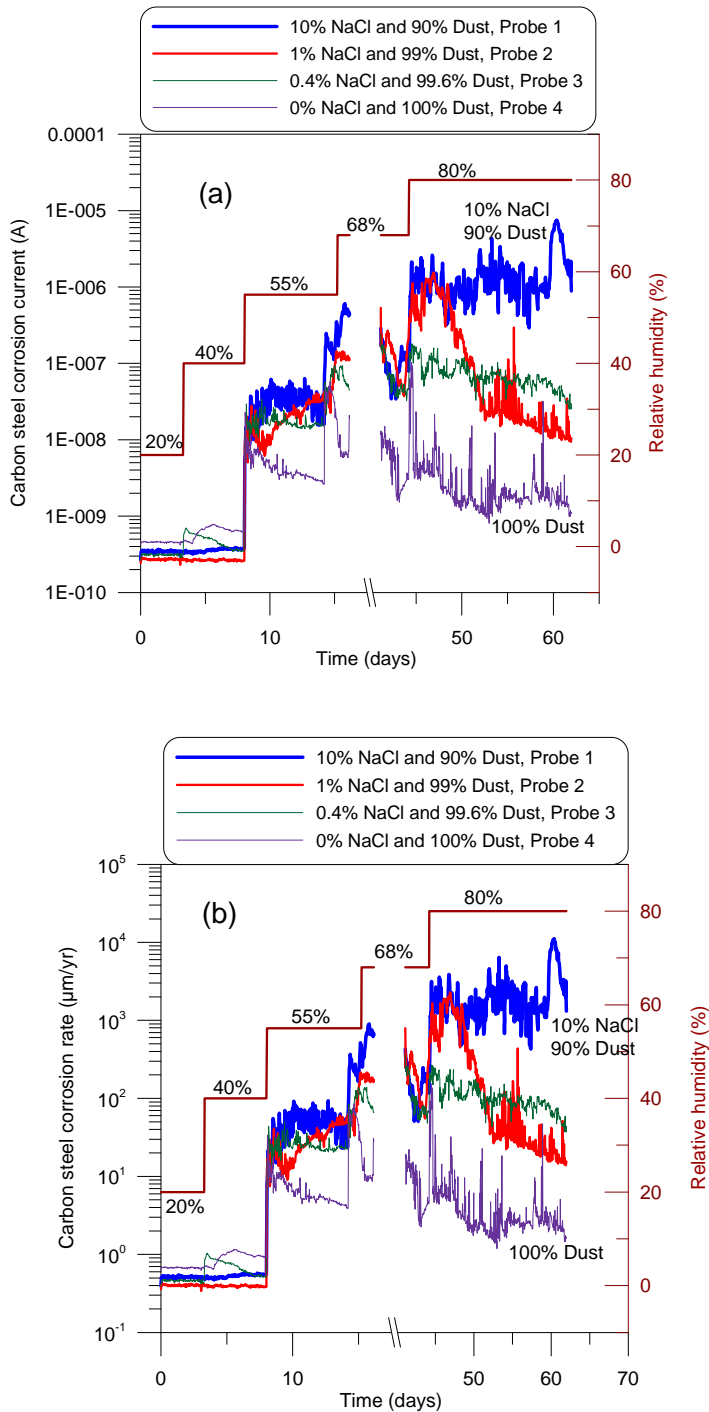


**Figure 2-10. (a) Measured Maximum Corrosion Current and (b) Calculated Corrosion Rate for Test 2 Carbon Steel Probes. Test 2 Was Conducted at 70 °C [158 °F] Using the Following Solid Phase Compositions: (i) 10 Percent NaCl–90 Percent Dust On Probe 1, (ii) 1 Percent NaCl–99 Percent Dust on Probe 2, (iii) 0.4 Percent NaCl–99.6 Percent Dust on Probe 3, and (iv) 100 Percent Dust on Probe 4.**

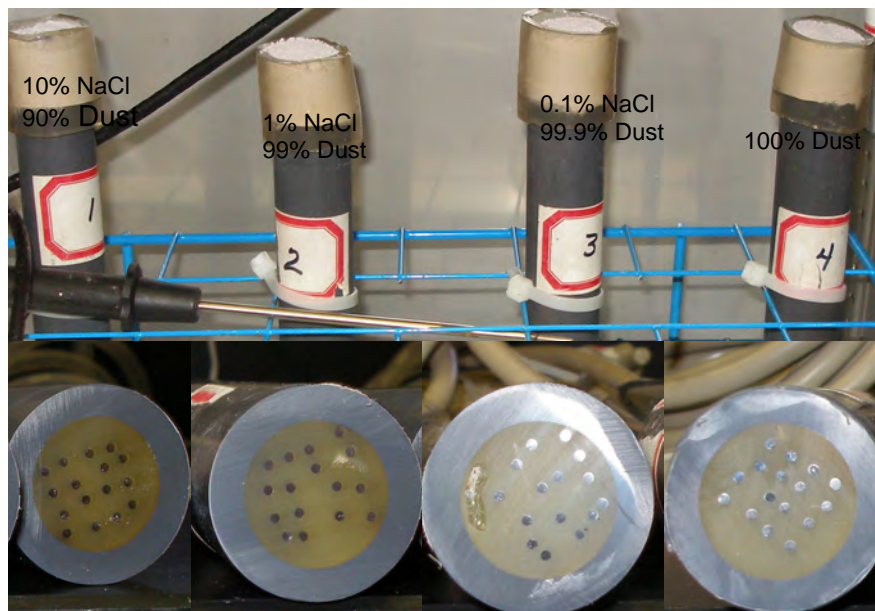


**Figure 2-11. Posttest Photographs of the Carbon Steel Probes From Test 2**

by dust. Corrosion was observed on each carbon steel probe even for the 100 percent dust system, but the number of corrosion sites decreased with decreasing percentage of NaCl in the mixture.

#### 2.4.2.3 Test 3—NaCl–Quartz and NaCl–Dust Mixtures at 70 °C [158 °F]

To compare directly the results for pure dust, pure quartz, and mixtures with a very small amount of NaCl, Test 3 was conducted with the following solid phase compositions: (i) 0.4 percent NaCl–99.6 percent quartz on Probe 1, (ii) 100 percent quartz on Probe 2, (iii) 0.4 percent NaCl–99.6 percent dust on Probe 3, and (iv) 100 percent dust on Probe 4. Figure 2-12 shows the measured corrosion current from all probes. The measured currents indicate that no deliquescence brine formed at all relative humidity in the test with 100 percent quartz, whereas brine formed in the test with 100 percent rock dust. Consistent with the observations in Test 2, deliquescence brine formed at a lower relative humidity (55 percent) in the NaCl–dust mixture compared to the NaCl–quartz mixture. At a relative humidity of 80 percent, for both the 0.4 percent NaCl–99.6 percent dust and 100 percent dust tests, the measured current reached a peak then decayed with time. In contrast, the current from the test with NaCl–quartz continued to increase and resulted in higher current compared to the tests involving a dust component.

The results suggest that the presence of dust reduced the corrosion current by a capillary retention effect and/or by the leaching of a corrosion-inhibiting species from the dust. However, the results also indicate that the presence of dust did not prevent brine from contacting the metal surface.

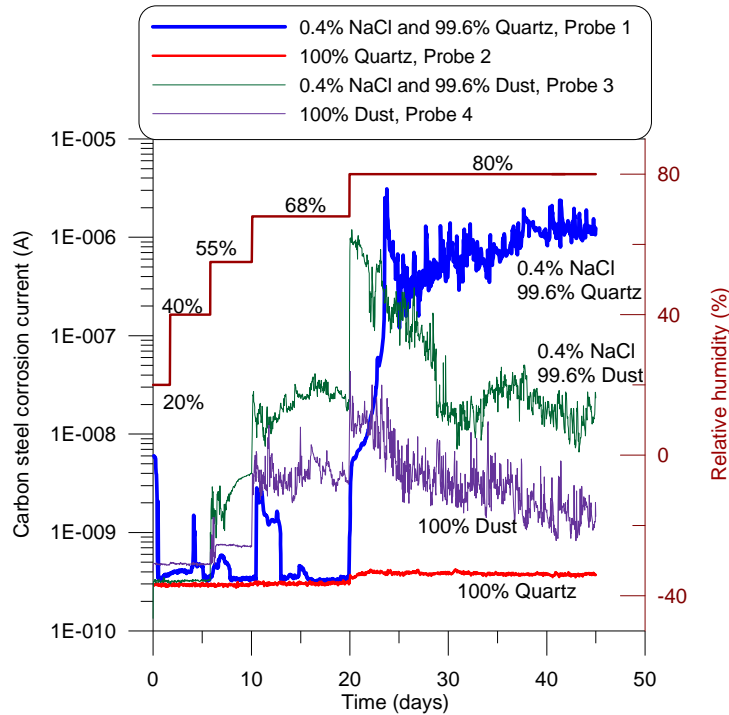


**Figure 2-12. Maximum Corrosion Current Measured From the Test 3 Carbon Steel Probes. Test 3 Was Conducted at 70 °C [158 °F] With the Following Solid Phase Compositions: (i) 0.4 Percent NaCl–99.6 Percent Quartz on Probe 1, (ii) 100 Percent Quartz on Probe 2, (iii) 0.4 Percent NaCl–99.6 Percent Dust on Probe 3, and (iv) 100 Percent Dust on Probe 4.**

#### 2.4.2.4 Test 4—Effect of Dust Particle Sizes

To understand the effect of particle size on the capability of dusts to retain moisture by capillary retention, Test 4 was conducted with 1 percent NaCl–99 percent dust mixtures and the following dust particle size ranges: (i)  $>149\ \mu\text{m}$  [ $>5.87\ \text{mil}$ ] on Probe 1, (ii)  $149\text{--}74\ \mu\text{m}$  [ $5.87\text{--}2.9\ \text{mil}$ ] on Probe 2, (iii)  $74\text{--}44\ \mu\text{m}$  [ $2.9\text{--}1.7\ \text{mil}$ ] on Probe 3, and (iv)  $<44\ \mu\text{m}$  [ $<1.7\ \text{mil}$ ] on Probe 4. Figure 2-13 shows the corrosion current from all four probes. Consistent with previous tests, brines formed at a relative humidity of 55 percent. Except for the largest dust particles [ $>149\ \mu\text{m}$  [ $>5.87\ \text{mil}$ ]], no significant difference in corrosion current between the tests was observed, which suggests a negligible effect of particle size on capillary retention of brine. Figure 2-13 shows that large size particles delayed the current increase. This delay could result from the smaller surface area of large particles to absorb moisture compared to other smaller particles less than  $149\ \mu\text{m}$  [ $5.87\ \text{mil}$ ]. Approximation showed that the total surface areas of particles from Probes 1, 2, and 3 were at the same order; however, the total surface area of particles from Probe 1 was one order of magnitude smaller than other smaller particles.

#### 2.4.2.5 Test 5—Alloy 22 and Carbon Steel Corrosion in NaCl–NaNO<sub>3</sub>–KNO<sub>3</sub> Dust Mixture at 125 °C [257 °F]

This test assessed the corrosion at high temperature of Alloy 22 in comparison with carbon steel. The test used a mixture of NaCl, NaNO<sub>3</sub>, and KNO<sub>3</sub> salts to allow deliquescence to occur above 100 °C [212 °F]. Because of the limited operational temperature range of the humidity chamber, a temperature of 125 °C [257 °F] was selected for the test. At this temperature, the

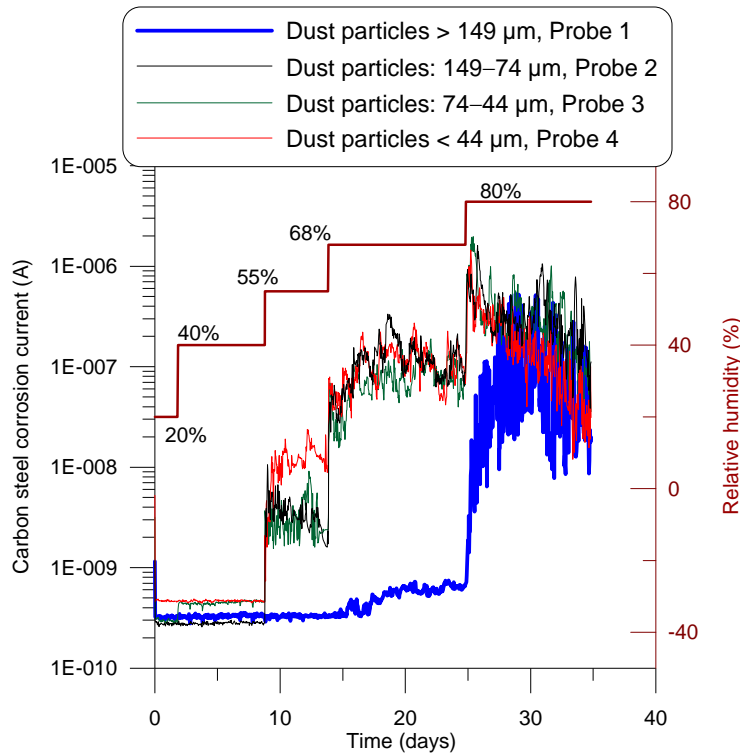


**Figure 2-13. Maximum Corrosion Current Measured From the Test 4 Carbon Steel Probes. Test 4 Was Conducted at 70 °C [158 °F] Using Mixtures of 1 Percent NaCl–99 Percent Dust. The Dust Had the Following Particle Size Ranges: (i) >149  $\mu\text{m}$  [5.87 mil] on Probe 1, (ii) 149–74  $\mu\text{m}$  [5.87–2.9 mil] on Probe 2, (iii) 74–44  $\mu\text{m}$  [2.9–1.7 mil] on Probe 3, and (iv) <44  $\mu\text{m}$  [<1.7 mil] on Probe 4.**

mutual deliquescence relative humidity for a NaCl–NaNO<sub>3</sub>–KNO<sub>3</sub> mixture calculated using StreamAnalyzer Version 2.0 is 24.5 percent (Figure 2-4), and the calculated composition of the deliquescence brine is listed in Table 2-14. The calculated brine composition was used to estimate the weight ratios of reagent grade NaCl, NaNO<sub>3</sub>, and KNO<sub>3</sub> salts that were used in the test (column 4 in Table 2-14).

Four probes were used in the test—two with Alloy 22 electrodes and another two with carbon steel electrodes. Two weight ratios of dust to salt mixtures (3:7 and 5:5) were used, which yielded the following four probes: (i) 30 percent dust–70 percent salt mixture on carbon steel Probe 1, (ii) 50 percent dust–50 percent salt mixture on carbon steel Probe 2, (iii) 30 percent dust–70 percent salt mixture on Alloy 22 Probe 3, and (iv) 50 percent dust–50 percent salt mixture on Alloy 22 Probe 4.

Figure 2-14(a) shows the corrosion current measured from the four probes. Data from the day-15 to day-40 portion of the test are not shown in this figure, because the humidity chamber did not function well during that period. The results show that under the same test conditions, the carbon steel corrosion current was much higher than that measured from Alloy 22 probes.

The corrosion rate calculated for carbon steel was about 20 times that of Alloy 22. Because the coupled multielectrode probe measures the rate of nonuniform corrosion, which

**Table 2-14. Chemical Composition of Brine Formed by Deliquescence of a NaCl–NaNO<sub>3</sub>–KNO<sub>3</sub> Salt Mixture at a Temperature of 125 °C [257 °F] and Weight Ratio of Reagent Grade Salts in Salt Mixture Used in Test 5**

Salt	Moles Per kg H <sub>2</sub> O	Mass (g) Per kg H <sub>2</sub> O	Weight Ratio in Salt Mixture
NaCl	2.69	157	0.018
NaNO <sub>3</sub>	39.2	3,332	0.381
KNO <sub>3</sub>	52.0	5,252	0.601

includes localized corrosion, the low measured currents from the Alloy 22 probe also indicate that the penetration rate due to localized corrosion of Alloy 22 in the mixture of dust and NaCl–KNO<sub>3</sub>–NaNO<sub>3</sub> was very low at 125 °C [257 °F].

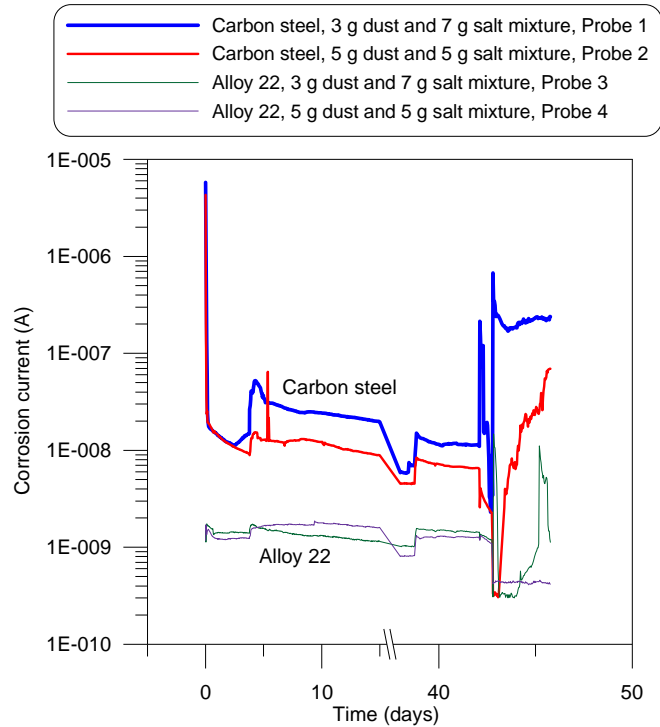
Figure 2-14(b) shows the posttest probes. No localized corrosion was observed on Alloy 22 with the unaided eye and under an optical microscope with × 20 magnification, which is consistent with the low nonuniform corrosion current measured with the probe. Table 2-13 shows that the molar ratio of chloride plus sulfate to chloride in the dust leachate is less than or equal to 0.30. However, previous tests in bulk solution at 110 °C [230 °F] (Dunn, et al., 2005) indicated that localized corrosion is inhibited when the nitrate to chloride molar ratio is at least 0.3. Thus, the lack of evident localized corrosion on the Alloy 22 specimen from this test could be due to the short duration of the test and the small amount of brine formed during the test.

## 2.5 Summary and Conclusions

Available information on the geochemistry of dust samples taken from Yucca Mountain and the vicinity was reviewed. Dusts contain relatively small fractions of soluble salts, ranging from 10 percent as the maximum in remote locations to less than 0.1 percent in Yucca Mountain surface dusts. Leachates typically contain sodium, potassium, and calcium as major cations and chloride, nitrate, and sulfate as major anions. Nitrate-to-chloride ratios exceeded 0.1 for all samples. Feldspars, quartz, and calcite were among the minerals typically found in Yucca Mountain dusts.

The possible assemblage of deliquescent salts present in Yucca Mountain dusts was determined by simulating the evaporation of aqueous solutions derived from leaching dust samples from Yucca Mountain. The results of the thermodynamic simulations indicated that the most likely salt assemblages comprise NaCl–NaNO<sub>3</sub>–KNO<sub>3</sub> and NaCl–KNO<sub>3</sub> mixtures, with relatively uncommon occurrence of assemblages containing calcium nitrate salts. Thermodynamic calculations also were conducted to determine the mutual deliquescence relative humidity of the salt assemblages and the chemistry of the brines that could form by deliquescence. The results indicate that the mutual deliquescence relative humidity of the salt assemblages is low, particularly at temperatures above 100 °C [212 °F], such that if these salts were present in the potential repository, brines would likely form by salt deliquescence even if the waste packages were relatively hot. However, the brines that are likely to form at temperatures above 120 °C [248 °F] would have molar ratios of nitrate to chloride higher than 5. At temperatures between 100 and 120 °C [212 and 248 °F], the nitrate-to-chloride molar ratio may be low (less than 0.1), but the molar ratio of total inhibitors (nitrate + sulfate + bicarbonate + carbonate) to chloride would still be higher than 3.3 for the KCl–KNO<sub>3</sub> salt assemblage.

(a)



(b)

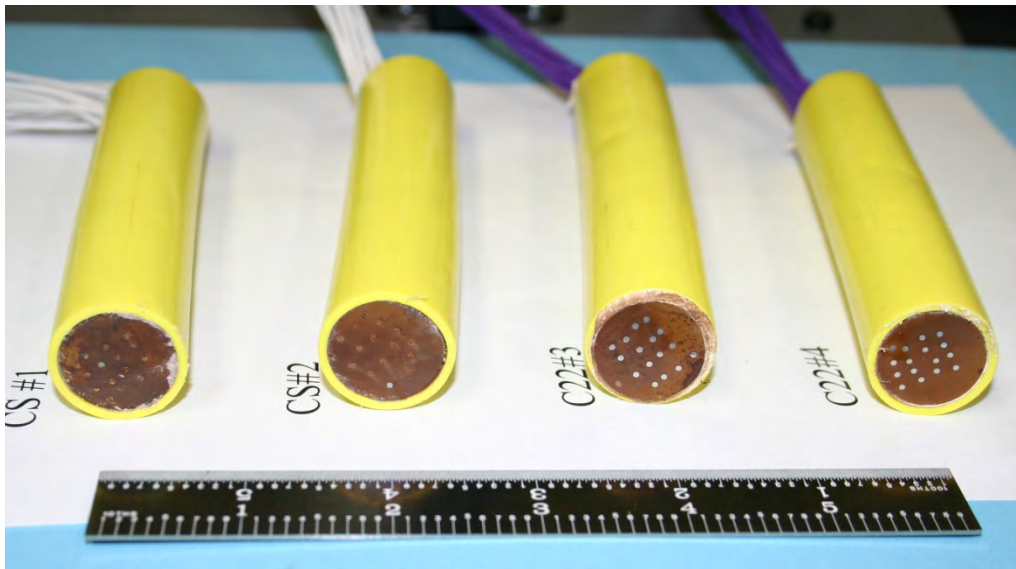


**Figure 2-14. (a) Maximum Corrosion Current Measured From Test 5 Probes. Test 5 Was Conducted at 125 °C [257 °F] and Relative Humidity of 25 Percent Using the Following Solid Phase Compositions and Probe Types: (i) 30 Percent Dust–70 Percent Salt Mixture on Carbon Steel Probe 1, (ii) 50 Percent Dust–50 Percent Salt Mixture on Carbon Steel Probe 2, (iii) 30 Percent Dust–70 Percent Salt Mixture on Alloy 22 Probe 3, and (iv) 50 Percent Dust–50 Percent Salt Mixture on Alloy 22 Probe 4. (b) Posttest Photographs of the Probes.**

The effect of capillary retention by dusts on the corrosivity of deliquescence brines was evaluated. The experiments were conducted at 70 °C [158 °F] in a temperature-and-humidity controlled chamber using solid mixtures with varying ratios of NaCl to quartz or rock dust. The results indicate that nondeliquescent quartz or rock dust reduced the amount of deliquescence brine that contacted the metal surface. However, even at a dust-to-NaCl weight ratio of 249, a brine solution still contacted and caused the corrosion of the carbon steel metal surface. No significant effect of dust particle size on capillary retention was observed, except for the largest dust particles {>149  $\mu\text{m}$  [>5.87 mil]} used in the test.

Additional experiments assessed the corrosion of Alloy 22 in brines formed by deliquescence of salts mixed with rock dust. The tests were conducted using Alloy 22 coupled multielectrode probes at a temperature of 125 °C [257 °F] and at humidity near the deliquescence point of a NaCl–KNO<sub>3</sub>–NaNO<sub>3</sub> salt mixture. The results indicate that the corrosion rate of Alloy 22 was much lower than that of carbon steel and no visible localized corrosion was observed on Alloy 22 probes. Because the coupled multielectrode probe measures the rate of nonuniform corrosion, which includes localized corrosion, the low measured currents from the Alloy 22 probe also indicate that the penetration rate due to localized corrosion for Alloy 22 in the mixture of dust and NaCl–KNO<sub>3</sub>–NaNO<sub>3</sub> was low at 125 °C [257 °F] under the test conditions.

## 2.6 References

Bechtel SAIC Company, LLC. "Analysis of Dust Deliquescence for FEP Screening." ANL–EBS–MD–000074. Rev. 01, Addendum 01. Las Vegas, Nevada: Bechtel SAIC Company, LLC. 2007.

———. "Analysis of Dust Deliquescence for FEP Screening." ANL–EBS–MD–000074. Rev. 01. Las Vegas, Nevada: Bechtel SAIC Company, LLC. 2005.

———. "Environment on the Surfaces of the Drip Shield and Waste Package Outer Barrier." ANL–EBS–MD–000001. Rev. 01. Las Vegas, Nevada: Bechtel SAIC Company, LLC. 2004.

Bryan, C. "Evolution of Waste Package Environments in a Repository at Yucca Mountain." Nuclear Waste Technical Review Board Meeting. September 25–26, 2006, Las Vegas, Nevada. 2006. <<http://www.nwtrb.gov/meetings/2006/sept/bryan.pdf>>. (7 April 2008).

Dunn, D.S., O. Pensado, Y.-M. Pan, R.T. Pabalan, L. Yang, X. He, and K.T. Chiang. "Passive and Localized Corrosion of Alloy 22—Modeling and Experiments." CNWRA 2005-02. San Antonio, Texas: CNWRA. 2005.

Felker, S., P.D. Hailey, T. Lian, K.J. Staggs, and G. Gdowski. "Alloy 22 Localized Corrosion Susceptibility in Aqueous Solutions of Chloride and Nitrate Salts of Sodium and Potassium at 110–150 °C." UCRL–TR–218195. Livermore, California: Lawrence Livermore National Laboratory. 2006.

Gerbino, A. "A Guide for Using the OLI Analyzers." Morris Plains, New Jersey: OLI Systems, Inc. 2006. <<http://support.olisystems.com/Documents/Manuals/TricksOfTheTrade.pdf>>. (7 April 2008).

Gruszkiewicz, M.S., D.A. Palmer, R.D. Springer, P. Wang, and A. Anderko. "Phase Behavior of Aqueous Na–K–Mg–Ca–Cl–NO<sub>3</sub> Mixtures: Isopiestic Measurements and Thermodynamic Modeling." *Journal of Solution Chemistry*. Vol. 36. pp. 723–765. 2007.

Pabalan, R.T., L. Yang, and L. Browning. "Deliquescence Behavior of Multicomponent Salts: Effects on the Drip Shield and Waste Package Chemical Environment of the Proposed Nuclear Waste Repository at Yucca Mountain, Nevada." P. McGrail and G.A. Cragolino, eds. *Scientific Basis for Nuclear Waste Management XXV. Symposium Proceedings 713*. Warrendale, Pennsylvania: Materials Research Society. pp. 37–44. 2002.

Pensado, O. "Corrosion Model to Support Total System Performance Assessments." Nuclear Waste Technical Review Board Meeting, September 25–26, 2006, Las Vegas, Nevada. 2006. <<http://www.nwtrb.gov/meetings/2006/sept/pensado.pdf>>. (7 April 2008).

Peterman, Z. "Effects of Temperature on the Compositions of Soluble Salts in Dust at Yucca Mountain." Nuclear Waste Technical Review Board Meeting, January 16, 2008, Las Vegas, Nevada. 2006. <<http://www.nwtrb.gov/meetings/2008/jan/peterman.pdf>>. (7 April 2008).

Rard, J.A. "Results from Boiling Temperature Measurements for Saturated Solutions in the Systems  $\text{NaCl}+\text{Ca}(\text{NO}_3)_2+\text{H}_2\text{O}$ ,  $\text{NaNO}_3+\text{KNO}_3+\text{H}_2\text{O}$ , and  $\text{NaCl}+\text{KNO}_3+\text{H}_2\text{O}$ , and Dry Out Temperatures for  $\text{NaCl}+\text{NaNO}_3+\text{KNO}_3+\text{Ca}(\text{NO}_3)_2+\text{H}_2\text{O}$ ." UCRLTR–217415. Livermore, California: Lawrence Livermore National Laboratory. 2005.

———. "Results from Boiling Temperature Measurements for Saturated Solutions in the Systems  $\text{NaCl}+\text{KNO}_3+\text{H}_2\text{O}$ ,  $\text{NaNO}_3+\text{KNO}_3+\text{H}_2\text{O}$ , and  $\text{NaCl}+\text{NaNO}_3+\text{KNO}_3+\text{H}_2\text{O}$ ." UCRL–TR–207054. Livermore, California: Lawrence Livermore National Laboratory. 2004.

Reheis, M.C. "Dust Deposition in Nevada, California, and Utah, 1984-2002." U.S. Geological Survey Open-File Report 03-138. 2003.

Wang, P., A. Anderko, and R.D. Young. "A Speciation-Based Model for Mixed-Solvent Electrolyte Systems." *Fluid Phase Equilibria*. Vol. 203. pp. 141–176. 2002.

Yang, L., N. Sridhar, and G. Cragolino. "Comparison of Localized Corrosion of Fe–Ni–Cr–Mo Alloys in Chloride Solutions Using a Coupled Multielectrode Array Sensor." CORROSION/2002. Paper No. 02545. Houston, Texas: NACE International. 2002a.

Yang, L., R.T. Pabalan, and L. Browning. "Experimental Determination of the Deliquescence Relative Humidity and Conductivity of Multicomponent Salt Mixtures." *Scientific Basis for Nuclear Waste Management XXV Symposium. Proceedings 713*. P. McGrail and G.A. Cragolino, eds. Warrendale, Pennsylvania: Materials Research Society. pp. 135–142. 2002b.

### 3 CORROSIVITY OF DELIQUESCENCE BRINES TO ALLOY 22 AT ELEVATED TEMPERATURES

General corrosion rates of Alloy 22 exposed to large quantities of concentrated brines containing NaCl, NaNO<sub>3</sub>, and KNO<sub>3</sub> in closed systems have been reported in the literature. To obtain the general corrosion rates, measurements were conducted at temperatures above 100 °C [212 °F] in autoclaves under pressurized conditions.

Because the potential repository drift would not be sealed (Sandia National Laboratory, 2007a) and the water vapor pressure could not be higher than the prevailing ambient pressure, the general corrosion rate of Alloy 22 exposed to large quantities of brines containing NaCl, NaNO<sub>3</sub>, and KNO<sub>3</sub> were also measured in open systems at the Center for Nuclear Waste Regulatory Analyses (CNWRA<sup>®</sup>). Under such conditions, the brine would have a similar composition as the brines that may be formed by deliquescence of the salt mixtures containing NaCl, NaNO<sub>3</sub>, and KNO<sub>3</sub>. Whereas some of the data from CNWRA have been reported, additional data have been recently obtained. This chapter reviews the Alloy 22 corrosion rates that were reported in the literature and presents data recently obtained in the open systems.

#### 3.1 Corrosion Rate of Alloy 22 in Nitrate–Chloride Salt Systems Measured in Closed Systems

Orme, et al. (2004) used the weight loss method to measure the corrosion rate of Alloy 22 with foil specimens exposed to both the vapor and the liquid phases of a system containing a nitrate–chloride brine inside an autoclave at temperatures between 120 and 220 °C [248 and 428 °F]. The total concentration of the salts in the brines varied from 6.7 to 9.6 molal, and the nitrate-to-chloride ratio varied from 0.05 to 6.7. The autoclaves were made of Alloy 276, and the specimens were assembled on metal racks that were fabricated from Alloy 22. Because the brines were relatively dilute {purposely controlled so that the brines were saturated at 90 °C [194 °F]}, the experiments were conducted under pressurized conditions to maintain liquid phase in addition to the vapor phase. Because the autoclave was sealed, the oxygen initially in the air space of the autoclave might have been partially consumed by the reaction with the metal surfaces inside the autoclave after the autoclave was heated up to test temperature. Therefore, the corrosion potential was probably low, even though the system was not purged with an inert gas at the start of the test. The test durations varied from 120 to 240 days.

The measured corrosion rates varied from –45 to 150 nm/yr [–0.0018 to 0.0059 mil/yr]. The negative corrosion rates were due to the difficulties in removing, by acid cleaning after the tests, the oxides formed on the specimen surfaces. These oxides led to weight gains, instead of weight losses. The accuracy of the weighing system {±30 μg [±0.001 oz]} may have introduced an error in the corrosion rate of ±30 nm/yr [±0.0012 mil/yr] for the foil specimens.

The maximum corrosion rate measured in the liquid phase under all test conditions was less than 150 nm/yr [±0.0059 mil/yr] with an uncertainty of ±60 nm/yr [±0.0024 mil/yr]; the maximum corrosion rate measured in the vapor phase under all test conditions was less than 70 nm/yr [0.0027 mil/yr] with an uncertainty of ±40 nm/yr [±0.0016 mil/yr].

Surface examination with cross-sectional transmission electron microscopy revealed that the oxide thickness varied from 0 to 60 nm [0 to 0.0024 mil] for specimens exposed at 140 °C [284 °F] for up to 270 days, but it was as high as 500 to 600 nm [0.020 to 0.024 mil] for specimens exposed at 220 °C [428 °F] for 270 days, which corresponds to corrosion rates from

667 to 800 nm/yr [0.026 to 0.031 mil/yr]. These high rates are not consistent with the maximum corrosion rate obtained from the weight loss method {150 nm/yr [0.0059 mil/yr] at 220 °C [428 °F]}, and the discrepancy was probably caused by the incomplete removal of the oxide layer with the acid cleaning method used prior to the weight loss measurement.

The experiments conducted under similar conditions (9.6 to 21 molal of salt concentration and 0.5 to 7.4 nitrate-to-chloride ratio) at temperatures ranging from 160 to 220 °C [320 to 428 °F] yielded near zero corrosion rates { $8\pm 12$  nm/yr for specimens exposed to the liquid phase and  $5\pm 11$  nm/yr [ $0.0002\pm 0.00043$  mil/yr] for specimens exposed to vapor phase} using the weight loss method (Dixit, et al., 2006). Auger depth profile analysis, however, revealed that the oxide thickness for selected specimens that were exposed to the liquid phase of the system at 220 °C [428 °F] varied from 100 to 370 nm [0.004 to 0.016 mil], which corresponds to corrosion rates ranging from 133 to 493 nm/yr [0.0052 to 0.019 mil/yr].

Considering the large uncertainties in the removal of the oxide layer on the specimens, the weight loss measurements may underestimate the corrosion rate. Because the thickest oxide layer observed was 600 nm [0.024 mil] in a 270-day test, which corresponds to a corrosion rate of 800 nm/yr [0.031 mil/yr], the maximum uncertainty is probably less than 1,000 nm/yr [0.04 mil/yr]. Therefore, the measured corrosion rates of Alloy 22 in the concentrated solution containing NaCl, NaNO<sub>3</sub>, and KNO<sub>3</sub> as Orme, et al. (2004) and Dixit, et al. (2006) reported were less than 1 μm/yr [0.04 mil/yr] at temperatures from 120 to 220 °C [248 to 428 °F].

### **3.2 Corrosion Rate of Alloy 22 in Nitrate–Chloride Salt Systems Measured in Open Systems**

Because the potential repository drift would not be sealed (Sandia National Laboratory, 2007a), rock cracks and air spaces within rubbles would allow air and water vapor to move to or from the emplacement drift during the high temperature period. Air may be present in some sections of the drift where insufficient groundwater could be available in the boiling zone as the water supply for steam generation would continuously flow outward and keep the air from entering into the drift. Two sets of experiments were conducted at CNWRA in 2005 and 2006, respectively, under conditions that simulated the unsealed system. Experiments conducted in 2005 were summarized in a previous report (Yang, 2006) and described partially in a conference paper (Yang, et al., 2007). In 2006, another set of experiments was conducted to verify the experimental results measured in 2005. This section describes the experiments conducted in 2006 and analyzes the results from the two sets of experiments.

#### **3.2.1 Test Specimens**

Alloy 22 specimens with different metallurgical conditions were used in the experiments conducted in both 2005 and 2006. The experiments include both creviced and uncreviced specimens. Alloy 22 was tested in mill-annealed, thermally aged, and as-welded conditions. The metallurgical conditions and geometry of the different specimens are provided in Table 3-1. The shape of the creviced specimens is similar to that which Dunn, et al. (2005) used and is shown in Figure 3-1. The chemical compositions of these specimens are given in Table 3-2. All specimens were polished with 600-grit silicon carbide paper before use.

The weight loss measurements were conducted according to ASTM G1–03 (ASTM International, 2005). The posttest specimens were first cleaned with soft brushes and

Table 3-1. Specimens Used in the Experiments					
Specimen Code	Heat Treatment	Heat Number of Base Metal	Heat Number of Filler Metal	Geometry (cm <sup>3</sup> ) [in <sup>3</sup> ]	Surface Area (cm <sup>2</sup> ) [in <sup>2</sup> ]
Thermally aged*	Thermally aged at 870 °C [1,598 °F] for 30 minutes	2277-1-3150	Not applicable	1.27 × 0.787 × 0.152 [0.5 × 0.31 × 0.06] or 1.27 × 1.27 × 0.152† [0.5 × 0.5 × 0.06]	2.66 [0.212] or 3.99† [0.618]
Annealed*	Mill-annealed specimens	2277-3-3266	Not applicable	1.27 × 2.54 × 0.25 [0.5 × 1.0 × 0.1]	8.48 [1.31]
Welded*	Welded specimens	2277-3-3292	WN 813	1.27 × 2.54 × 0.25 [0.5 × 1.0 × 0.1] or 1.27 × 2.54 × 0.15† [0.5 × 1.0 × 0.06]	8.48 [1.31] or 7.60† [1.18]
Annealed, creviced	Mill-annealed specimen	2277-3-3266	Not applicable	Figure 3-1	12.9 [2.00]
Welded, creviced	Welded specimen	2277-3-3292	WN 813	Figure 3-1	12.9 [2.00]

\*Specimens have a 2-mm [0.08-in]-diameter hole drilled at top for hanging in the test cells.  
†Used in the experiment conducted in 2005 only.

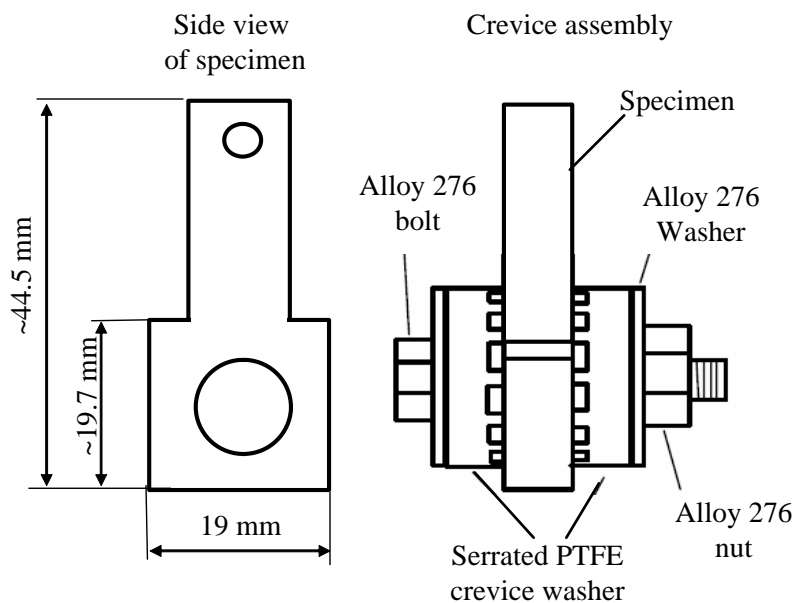


**Figure 3-1. Schematic Diagrams for the Creviced Specimens Used in the Tests (PTFE—Polytetrafluoroethylene: 1 mm = 0.04 in)**

<b>Heat Number</b>	<b>Ni*</b>	<b>Cr*</b>	<b>Co*</b>	<b>Fe*</b>	<b>Mo*</b>	<b>Mn*</b>	<b>W*</b>	<b>V*</b>	<b>Si*</b>	<b>C*</b>	<b>S*</b>	<b>P*</b>
2277-1-3150	Bal†	21.1	1.70	4.5	13.2	0.35	2.9	0.16	0.03	0.003	0.004	0.008
2277-3-3266	Bal†	21.4	1.19	3.75	13.30	0.23	2.81	0.14	0.03	0.005	0.004	0.008
2277-3-3292	Bal†	21.22	1.32	3.69	13.64	0.23	2.96	0.13	0.02	0.004	0.003	0.005
WN813	Bal†	22.24	0.41	2.37	13.7	0.34	3.13	0.01	0.02	0.003	0.001	0.003

\*Ni–Nickel, Cr–Chromium, Co–Cobalt, Fe–Iron, Mo–Molybdenum, Mn–Manganese, W–Tungsten, V–Vanadium, Si–Silicon, C–Carbon, S–Sulfur, and P–Phosphorus  
†Bal–Balance

rinsed with water and acetone, and then cleaned with a dilute HCl solution in an ultrasonically agitated bath. The specimens were then brushed with a soft brush and rinsed with acetone and water. The corrosion rates were calculated according to Eq. (3-1)

$$CR = 8.76 \times 10^7 \frac{W}{ADt} \quad (3-1)$$

where

*CR* — corrosion rate ( $\mu\text{m}/\text{yr}$ )  
*W* — weight loss (g)  
*A* — surface area ( $\text{cm}^2$ )  
*t* — time (hr)  
*D* — density ( $\text{g}/\text{cm}^3$ )

The microbalance used for the weight loss measurement had a precision of  $\pm 0.025$  mg [ $3.52 \times 10^{-5}$  oz], which corresponds to an error of  $\pm 20$  nm/yr [0.00079 mil/yr] in the corrosion rate for the specimens with the smallest surface area as shown in Table 3-1.

### **3.2.2 Test Vessels for Weight Loss Corrosion Rate Measurements**

The corrosion experiments were conducted in the same type of vessels described in the previous report (Figure 3-2) (Yang, 2006). Approximately 1,000 g [2.2 lb] of a salt mixture containing equimolar quantities of NaCl, NaNO<sub>3</sub>, and KNO<sub>3</sub> were placed in the glass vessel. The vessel was heated to a test temperature ranging from 130 to 220 °C [266 to 428 °F]. The system was kept at ambient pressure and vented to the open air through the vent bubbler, which was used to trap the vapor exiting the test vessel. The water in the bubbler was sampled periodically for pH and chemical analyses. The extra water in the bubbler that was used for chemical analysis or pH measurement was recycled back into the vessel in the experiment conducted in 2006, but not recycled in the experiment conducted in 2005.

At the start of the experiment, deionized water was added to the test vessel so that approximately half of the salts dissolved. A small amount of water {10 to 20 mL [0.34 to 0.68 oz]} was periodically added to the vessel to make up the water that evaporated and to maintain approximately the same liquid level in the test vessel. The water vapor pressure over

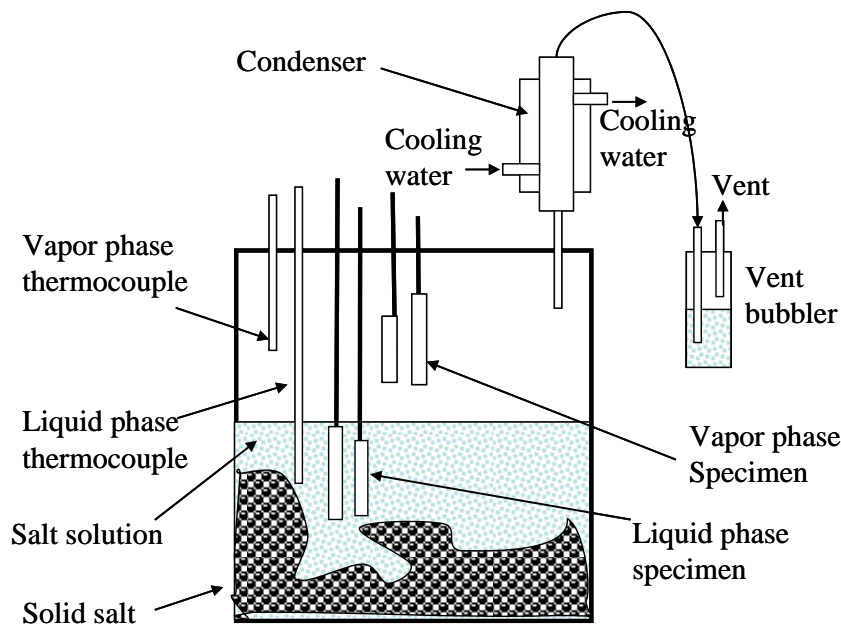


**Figure 3-2. Schematic of Typical Glass Vessels Used for the Weight Loss Experiment {Total Volume of the Vessel Is Approximately 3 L [102 oz]}**

the liquid phase in the test vessels was close to the atmospheric pressure because of the continuous and slow evaporation of the water; the chemical composition in the liquid phase is determined by the phase equilibrium.

Because the vessels were not sealed, the test systems are called “open systems.” They are designed to simulate the environmental conditions in the emplacement drift filled with water vapors produced by evaporation of groundwater and air diffusing or penetrating from the outside drift through rock cracks or rubble spaces (Sandia National Laboratories, 2007a,c). Note that such systems are not fully open, because widely open systems would not maintain the moisture required to simulate potential Yucca Mountain drift conditions.

Test specimens were placed in the vessels in contact with the vapor and liquid phases (Figure 3-2). The vessels were heated with a heating mantle, and thermocouples were used to measure the temperatures of the liquid and vapor phases.

At the end of the test and while the system was still at the test temperature, samples of known volume and weight were taken from the liquid phase for all the vessels for the experiment conducted in 2006, but for only one vessel for the experiment conducted in 2005. Because the samples crystallized as soon as the temperature decreased, the samples were redissolved and diluted with deionized water approximately 10 times the mass of the sample. The diluted solution, referred to as diluted samples in this report, was later analyzed for chemical composition and pH.

### 3.2.3 Test Vessels for Characterization of Vapor Phase Acidity

The vapor phase acidity was characterized by measuring the pH of vapor phase condensates obtained by using a distillation flask system shown in Figure 3-3. The two-stage liquid–solid

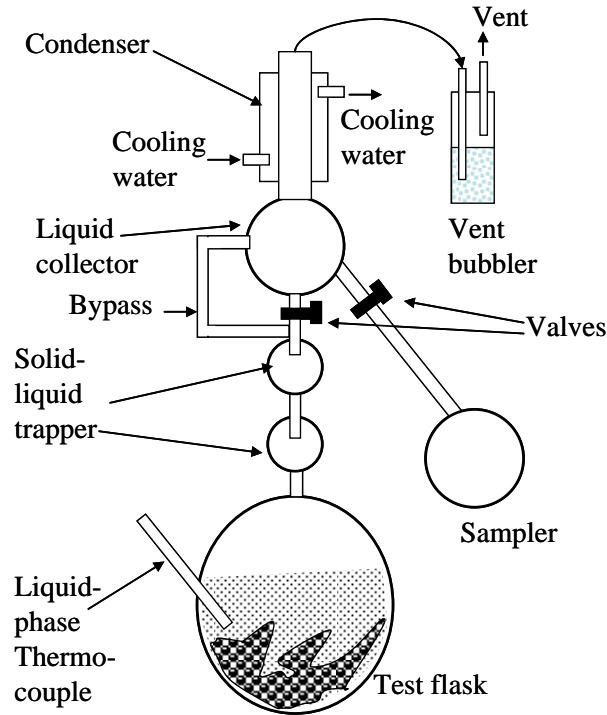


**Figure 3-3. Schematic of Typical Glass Flask Used for the Characterization of Vapor Phase pH {Volume of the Flask Is Approximately 1 L [34 oz]}**

traps were used to prevent solid particles or liquid drops formed in the test flask from entering the condenser and possibly contaminating the vapor phase condensates. During the test, the valve located between the upper trap and the liquid collector was normally open. This valve was only closed when a sample from the collector was being taken.

### 3.2.4 Weight Loss Results

Table 3-3 shows the general corrosion rates obtained at 130, 160, 190, and 220 °C [266, 320, 374, and 428 °F] from the weight loss measurements. Values are listed for the different types of specimens: (i) welded, (ii) annealed, (iii) thermally aged, (iv) annealed and creviced, and (v) welded and creviced. Note that two tests were conducted at 160 °C [320 °F] using Vessels B and E. The corrosion rates varied roughly from 0 to 500 nm/yr [0 to 0.020 mil/yr] for the specimens exposed to the liquid phase and from 0 to 80 nm/yr [0 to 0.0031 mil/yr] for the specimens exposed to the vapor phase. The small negative numbers listed in the table are due to experimental errors arising from weight loss measurements {±20 nm/yr [0.00079 mil/yr]} or from incomplete removal of the oxides by the acid cleaning method after exposure as discussed in Section 3.1.

Table 3-3 also lists the corrosion rates averaged at each temperature for specimens exposed to either the liquid phase or the vapor phase in the same test vessel and at the same temperature and the average vent bubbler pH (see below for more information). For the specimens exposed to the liquid phase, the average corrosion rate ranged from 10.8 to 462 nm/yr [0.00043 to 0.018 mil/yr]. For these samples, the average corrosion rate was low at 130 °C [266 °F], but significantly higher at 190 and 220 °C [374 and 428 °F]. Experiments conducted in Vessels B

**Table 3-3. Corrosion Rates of Alloy 22 Specimens in the Liquid and Vapor Phases and the pH of the Water in the Vent Bubbler Conducted in 2006**

	Vessel A 130 °C [266 °F]			Vessel B 160 °C [320 °F]			Vessel E 160 °C [320 °F]			Vessel C 190 °C [374 °F]			Vessel D 220 °C [428 °F]		
Coupons	Coupon ID	CR-Liq* (nm/yr)	CR-Vap† (nm/yr)												
Welded	AW3	15.6	—	BW3	22.0	—	—	—	—	CW3	130	—	DW3	218	—
	AW4	19.4	—	BW4	25.2	—	—	—	—	CW4	172	—	DW4	215	—
	AW7	—	7.5	BW7	—	25.2	—	—	—	CW7	—	36.7	DW7	—	31.0
	AW8	—	24.2	BW8	—	30.4	—	—	—	CW8	—	24.9	DW8	—	6.8
Annealed	A3	9.7	—	B3	27.8	—	—	—	—	C3	128	—	D3	135	—
	A4	-2.7	—	B4	36.2	—	—	—	—	C4	153	—	D4	148	—
	A7	—	11.3	B7	—	24.1	—	—	—	C7	—	0.0	D7	—	5.6
	A8	—	3.2	B8	—	19.9	—	—	—	C8	—	-2.2	D8	—	-6.2
Thermally aged	G44	-15.4	—	G48	23.4	—	G40	—	-4.8	G52	269	—	G56	232	—
	G45	—	—	G49	40.1	—	G41	—	1.6	G53	323	—	G57	249	—
	G46	—	—	G50	—	40.1	G42	425	—	G54	—	79.5	G58	—	62.8
	G47	—	—	G51	—	21.7	G43	499	—	G55	—	65.5	G59	—	77.2
Annealed Creviced	A9	—	30.9	B9	—	4.5	—	—	—	C9	—	-4.3	D9	—	-10.4
	A10	—	46.3	B10	24.5	—	—	—	—	C10	162	—	D10	106	—
Welded Creviced	AW9	—	37.2	BW9	—	21.0	—	—	—	CW9	—	33.3	DW9	—	4.4
	AW10	20.2	—	BW10	22.4	—	—	—	—	CW10	269	—	DW10	281	—
Average‡	—	10.8	23.0	—	27.7	23.4	—	462	0.8	—	201	30.0	—	198	23.5
Days	—	184	184	—	189	189	—	197	197	—	135	—	—	176	176
Points	—	6	7	—	8	8	—	2	2	—	8	8	—	8	8
Average Bubbler pH	7.2			7.8			2.9			6.6			6.3		

\*CR-Liq—stands for corrosion rate in liquid phase

†CR-Vap—stands for corrosion rate in vapor phase

‡Calculated after all negative values that are within experimental error {±20 nm/yr [0.00079 mil/yr]} were set to zero. Note: 1 mil/yr = 25,400 nm/yr

and E at 160 °C [320 °F] resulted in very different average corrosion rates {27.7 and 462 nm/yr [0.0011 and 0.018 mil/yr], respectively}. In light of the possible effect of the incomplete surface oxide removal as Dixit, et al. (2006) reported, the true corrosion rate may have been higher than the value measured from the weight loss measurement. To be consistent with the data reported previously (Yang, 2006) and with the long-term corrosion rate data reported for the Yucca Mountain Project (Sandia National Laboratories, 2007c), the effect of the incomplete oxide removal is ignored in this analysis.

In the liquid phase at 190 and 220 °C [374 and 428 °F], the corrosion rates from the thermally aged specimens are approximately two times higher than those of the annealed specimens; the corrosion rates of the welded creviced specimens are also approximately two times higher than those of the annealed creviced specimens. However, significantly different corrosion rates were not observed among the different types of specimens tested at 130 and 160 °C [266 and 320 °F].

For the specimens exposed to the vapor phase, the average corrosion rate was roughly the same at different temperatures {0.8 to 30 nm/yr [0 to 0.0012 mil/yr]}. The small negative value at 160 °C [320 °F] for Vessel E (see Table 3-3) was within the error that the weight loss measurement may cause {±20 nm/yr [0.00079 mil/yr]} and was treated as zero for deriving the average value. Unlike the specimens exposed to the liquid phase, the specimens exposed to the vapor phase in this vessel exhibited the lowest value. Because the corrosion rates of specimens exposed to the vapor phase are insignificant {<0.1 μm/yr [0.004 mil/yr]} compared to those exposed to the liquid phase and corrosion rates near 10 to 100 nm/yr [0.0004 to 0.004 mil/yr] are the approximate lower detection limits for the weight loss method under the experiment conditions, the following discussions focus on the corrosion of Alloy 22 exposed to the liquid phase.

Figure 3-4 shows the posttest appearance of typical specimens tested at 160, 190, and 220 °C [320, 374, and 428 °F] for the experiments conducted in 2006. The original polishing marks on the three specimens [Figure 3-4(a), (c), and (d)] that showed corrosion rates lower than 200 nm/yr [0.008 mil/yr] are clearly visible, whereas the polishing marks on the specimen that showed a higher corrosion rate [Figure 3-4(b)] have completely disappeared. In addition, the specimens in Figure 3-4(c) and (d) show visible differences between the welded fusion zone and the base metal. The polishing marks over the welded fusion zone are less visible than those over the base metal. Specimens in Figure 3-4(a) and (b) have very different appearances although they were exposed to the same temperature, confirming the high corrosion rate for specimens in Vessel E [Figure 3-4(b)] and the relatively low corrosion rate for specimens in Vessel B [Figure 3-4(a)].

Table 3-4 lists the corrosion rates obtained in the experiments conducted in 2005 (Yang, 2006; Yang, et al., 2007) and the average pH of the solution in the vent bubbler (Section 3.2.5 for more information). Optical and scanning electron microscopy results from the 2005 experiment showed significant corrosion for all specimens exposed to the liquid phase of the system (Yang, 2006; Yang, et al., 2007). Compared with the corrosion rate results shown in Table 3-4 {ranging from 1 to 6 μm/yr [0.04 to 0.3 mil/yr]} for the specimens exposed to the liquid phase, the corrosion rates listed in Table 3-3 are significantly lower, except for some deviation at 160 °C [320 °F]. No reliable temperature dependence can be drawn from the data shown in Table 3-4 due to the limited number of tests.

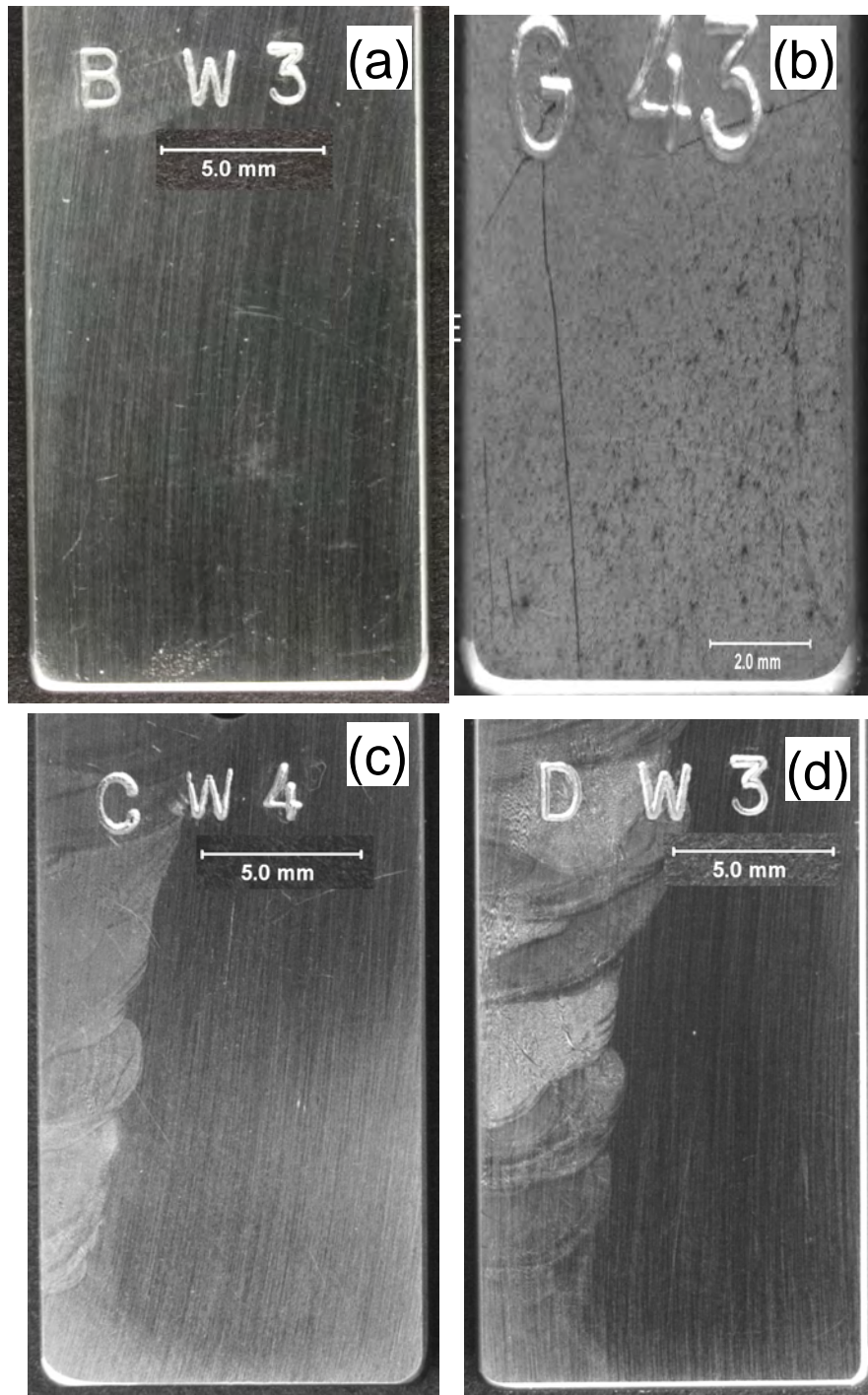


**Figure 3-4. Optical Appearance of the Specimens After the Tests in Liquid Phase For (a) Welded in Vessel B at 160 °C [320 °F], (b) Thermally aged in Vessel E at 160 °C [320 °F], (c) Welded in Vessel C at 190 °C [374 °F], and (d) Welded in Vessel D at 220 °C [428 °F] From the Experiment Conducted in 2006. [Polishing Marks in (b) Completely Disappeared.]**

**Table 3-4. Corrosion Rates of Alloy 22 Specimens in the Liquid and Vapor Phases and the pH of the Water in the Vent Bubbler Conducted in 2005\***

Coupons	Vessel A' 150 °C [302°F]			Vessel B' 160 °C [320 °F]			Vessel C' 180 °C [354 °F]		
	Coupon ID	CR-Liq (nm/yr)	CR-Vap (nm/yr)	Coupon ID	CR-Liq (nm/yr)	CR-Vap (nm/yr)	Coupon ID	CR-Liq (nm/yr)	CR-Vap (nm/yr)
Welded	1'	—	290	8'	—	0.6	3'	—	221
	2'	1623	—	9'	3970	—	4'	1096	—
Thermally Annealed	1	—	197	9	—	344	5	—	474
	2	1869	—	10	4125	—	6	1702	—
	3	—	553	11	—	172	7	—	368
	4	2066	—	12	3094	—	8	1035	—
Annealed Creviced	—	—	—	C	8512	—	A	1968	—
	—	—	—	CV	—	1235	B	—	954
Welded Creviced plus Solution Annealed	—	—	—	12M	9402	—	AV†	1190	—
	—	—	—	12T	—	1374	9T†	—	671
Average	—	1853	375	—	5821	781	—	1398	617
Days	—	80	80	—	49	49	—	60	60
Average Bubbler pH	3.0			2.0			3.5		

\* Yang, L. "Corrosion of Alloy 22 in Concentrated Nitrate and Nitrate and Chloride Sale Environments at Elevated Temperature—Progress Report." CNWRA 2006–02. San Antonio, Texas: Center for Nuclear Waste Regulatory Analyses. 2006.

†Specimens were exposed for 32 days only.

The experimental conditions for Tables 3-3 and 3-4 were nearly identical, except for the following:

1. The exposure times for the data in Table 3-3 were longer (80 to 140 days) than the exposure times for the data in Table 3-4 (50 to 80 days).
2. Some of the reagent grade chemicals were from different batches.
3. Some water from the vent bubbler was recycled back into the test vessel as makeup water in the experiments listed in Table 3-3, while no vent bubbler water was recycled back as makeup water in the experiments listed in Table 3-4.

### 3.2.5 Effect of pH on Corrosion Rate

As discussed previously, the corrosion rates in Tables 3-3 and 3-4 exhibited no reasonable correlation with temperature, immersion time, or metallurgical conditions. For the 2006 data, the corrosion rates varied from 28 to 462 nm/yr [0.0011 to 0.018 mil/yr] for the experiments that were conducted at the same temperature {160 °C [320 °F]} and with the same batch of chemical reagents (Table 3-3).

During the experiments, the water in the vent bubbler was frequently sampled and its pH was measured. Figure 3-5 shows the pH values for the water collected from the vent bubbler. The

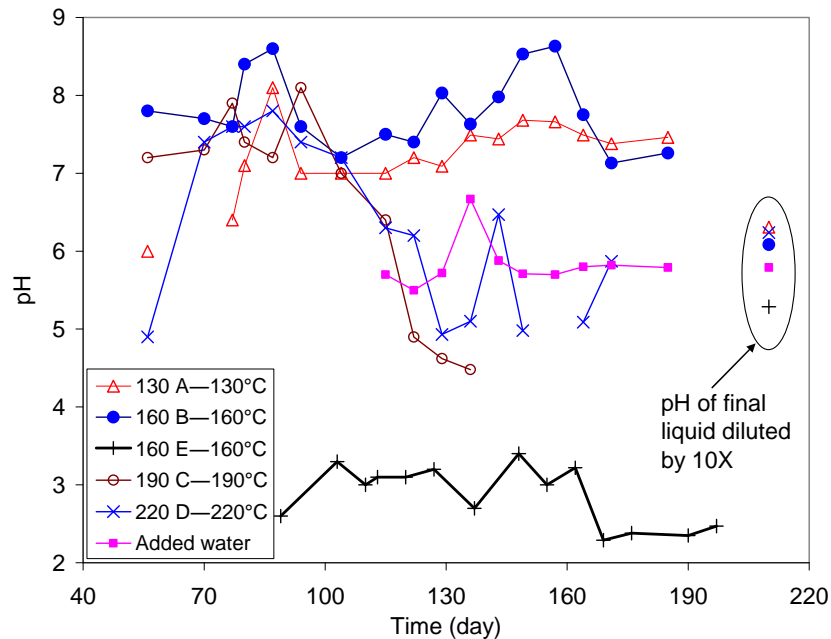


**Figure 3-5. pH of the Vent-Bubbler Water and the Deionized Makeup Water That Was Added to the Test Vessels and Vent Bubblers During the Tests and pH of the Diluted Sample From Four Test Vessels at the End of the Tests for the Experiments Conducted in 2006 { $T [^{\circ}\text{F}] = 1.8T [^{\circ}\text{C}] + 32$ }**

pH values of the deionized water that was used to fill the bubbler and to add to the test vessels as makeup water are also shown in Figure 3-5. The slightly acidic pH (~5.8) was probably due to the absorption of atmospheric  $\text{CO}_2$ . The pH of the water in the vent bubbler connected to Vessel E ranged from 2.2 to 3.2 and was significantly lower than that in the vent bubblers connected to the other test vessels. In the tests conducted at 190 °C [374 °F] (Vessel C) and 220 °C [428 °F] (Vessel D), the pHs of the water from the vent bubblers were high (7 to 8.6) initially, but decreased slowly to slightly acidic values (4.5 to 6) after 100 days. The difference between the pH of the vent-bubbler water and the pH of the deionized water would likely be due to the gases exiting the test vessels. Therefore, Vessel E produced a significant amount of acid gases during the course of the test. The acid gases in Vessel E could have been caused by the impurities in the reagent chemicals used or the components in the Pyrex™ glass vessels, such as silica or boron (see below for details), but the cause of the relatively high pH of the vapor phase in the other vessels is not known.

Figure 3-5 also shows the pH for the samples taken from the liquid phase of four of the test vessels at the end of each experiment (one of the vessels, Vessel C, broke before the liquid sample was taken). The samples were diluted 10 times by weight with deionized water (diluted sample) prior to the pH measurement. In general, the lower the pH in the vent bubbler, the lower the pH of the diluted sample. This observation is expected according to Henry's Law for the distribution of the acidic components in the liquid phase and in the gas phase. Note that the pH of the diluted samples from all the different vessels is in a narrow range (from 5.3 to 6.3) and none is above 7, which may be because of the pH of the added deionized water (~5.8). Figure 3-6 shows the pH of the vent bubblers and the pH of a diluted sample from Vessel A' for the 2005 tests conducted.

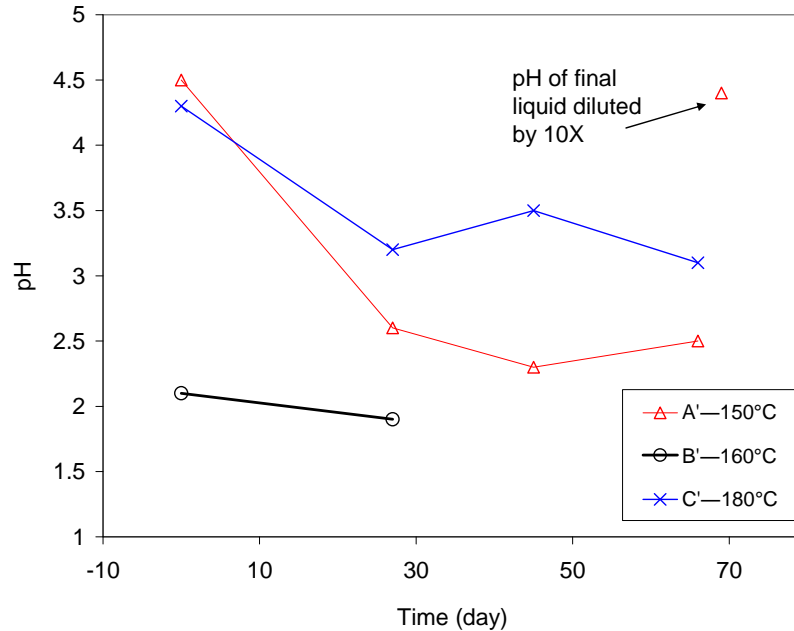


**Figure 3-6. pH of the Vent-Bubbler Water During the Tests Conducted in Vessels A', B', and C' and pH of the Diluted Sample From Vessel A' at the End of the Test for the Experiments Conducted in 2005 { $T [^{\circ}F] = 1.8T [^{\circ}C] + 32$ }**

The average pH for the vent-bubbler water connected to each test vessel is also given in Table 3-3. Figure 3-7 shows the corrosion rates plotted against the pH of the vent-bubbler water for the 2006 and 2005 experiments. There is a strong correlation between the corrosion rate and the pH of the vent-bubbler water regardless of the test temperature. When the vent-bubbler water was acidic (pH close to or less than 4), the corrosion rate of the Alloy 22 was high. The test temperatures are also indicated in Figure 3-7. It appears that the corrosion rates are higher for previous tests than for the present tests for the same vent-bubbler pH. This may be because the water that collected in the vent-bubbler was partially recycled during the 2006 experiments, but the water that collected in the bubbler was not recycled during the 2005 experiments. Bubbler water recycling during the 2006 experiments might have lowered the vent-bubbler pH for the liquid in the vessel with the same pH. In another words, the pH of the liquid in the vessels for the 2006 work should be higher than the pH of the liquid in the vessels for the 2005 data for the same vent bubbler pH. Because the corrosion rate in the liquid phase of the vessels is more directly related to the pH of the liquid rather than the pH of the vent bubbler, the corrosion rate was lower in the present work, even though one of the vent bubbler pHs was as low as that in the 2005 work.

For most of the experiments conducted in 2006, samples were taken directly from the liquid phase at the end of the tests and the pH values for the liquid samples were measured. However, only one value for the pH of the liquid phase sample was available from the experiments conducted in 2005 (Yang, et al., 2007).

In a short-term experiment to characterize the chemistry in the vapor phase of the test vessels, samples were taken from the liquid phase of the test flask after a relatively short period (7–10 days) and from the liquid collector for the condenser water. Figure 3-8 shows the pH of

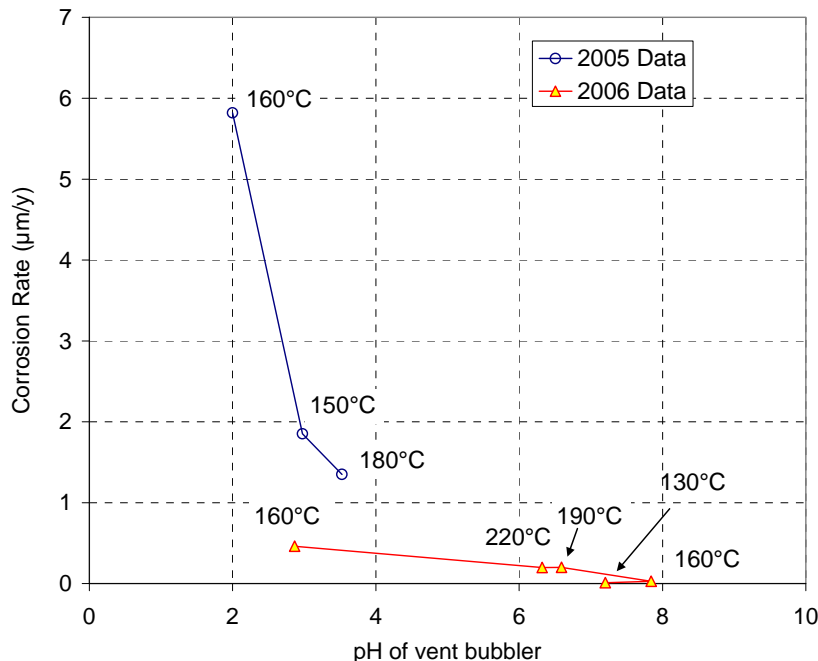


**Figure 3-7. Average Corrosion Rates for Alloy 22 as a Function of pH of the Vent-Bubbler Water [Vent-Bubbler Water Was Recycled During the 2006 Work, but Not Recycled During the 2005 Work (Yang, 2006)]  $\{T [^{\circ}F] = 1.8T [^{\circ}C] + 32\}$**

the diluted sample taken directly from the liquid phase of the test flasks as a function of the pH of the condenser water for the short-term tests and the one data point from the 2005 experiments (Yang, et al., 2007). For the short-term tests conducted in 2006, the pH of the condenser water and the pH of the diluted sample are linearly related, which is consistent with Henry's Law. Figure 3-8 also shows that the pH of the diluted samples from the short-term tests is significantly lower than that of the 2005 experiment for the same bubbler water pH. This is probably because the liquid samples for the 2005 experiments were taken 80 days after the solution was reacted in the vessel and the samples for the vent bubbler pH were taken during the course of the 80-day test (the average pH value). Conversely, the samples from the short-term tests were taken only about 10 days after they were reacted in the vessels. The acidic components of the liquid in the 2005 long-term tests might have decreased with time by processes such as degassing. According to Henry's Law, it is reasonable to assume that the slope of the linear correlation between the pH of the diluted samples at the end of the 2005 experiments and the pH of the vent-bubbler water averaged over the duration of the previous tests is the same as the slope of the linear correlation between the pH of the diluted samples and the pH of the condenser water from the short-term tests. Based on this assumption, the pH of the diluted sample for two of the 2005 tests was estimated using the single available data point (bubbler water pH = 3.0 and diluted sample pH = 4.4). Figure 3-8 shows that the estimated pH values for the diluted samples are 4.7 and 3.9 for the bubbler water pH of 3.5 and 2.0, respectively.

With these two estimated data points for the 2005 tests and the four data points in Figure 3-6 for the 2006 tests, the corrosion rates of Alloy 22 were plotted against the pH of the diluted samples for both the 2006 and the 2005 tests, as shown in Figure 3-9. The two sets of corrosion rate data exhibit an exponential relationship with pH. When the pH of the diluted samples is higher

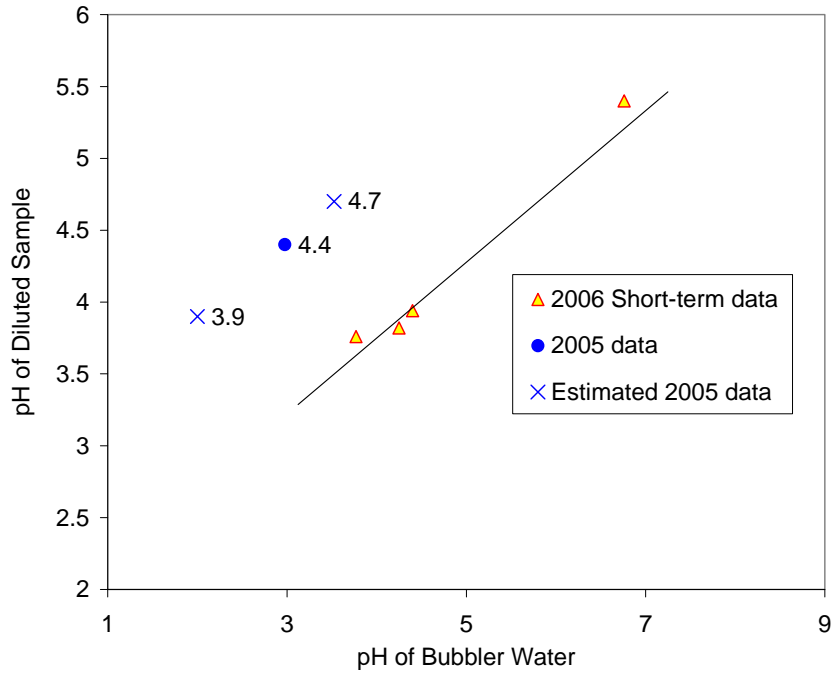


**Figure 3-8. Relationship Between the pH of the Diluted Sample From the Liquid Phase and the pH of the Bubler Water. Two Values for the pH of the Diluted Sample for the 2005 Data (3.9 and 4.7) Were Estimated Using the Linear Relationship for the Short-Term Data From the 2006 Work.**

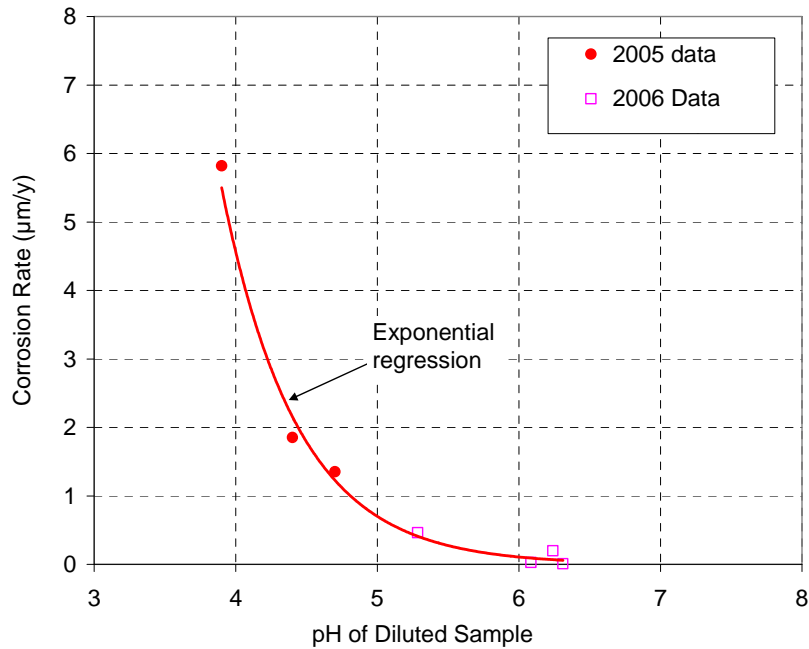


**Figure 3-9. Relationship Between Corrosion Rates of the Alloy 22 Specimens Exposed to the Liquid Phase and the pH of the Diluted Samples From the Liquid Phase (pH Values for Two of the 2005 Data Were Estimated As Shown in Figure 3-8)**

than 6, the corrosion rates are low, but when the pH of the diluted samples is lower than 6, the corrosion rates are significantly higher. Therefore, the high corrosion rates for Alloy 22 in the liquid phase observed in the 2005 tests are likely to have been caused by the low pH in the liquid phase (diluted sample pH <4.8), where the low corrosion rates observed in the 2006 experiments were due to the relatively high pH of the liquid phase (diluted sample pH 5.8).

### 3.3 Verification of the pH Effect on Alloy 22 Corrosion and Understanding of the pH Variations in the NaCl–NaNO<sub>3</sub>–KNO<sub>3</sub> Systems

Experiments were conducted to verify the effect of pH on Alloy 22 corrosion rates observed using the weight loss method in the NaCl–NaNO<sub>3</sub>–KNO<sub>3</sub> system under elevated temperature conditions. Simulation calculations were also conducted to understand the variations in pH of the NaCl–NaNO<sub>3</sub>–KNO<sub>3</sub> system at test temperatures.

#### 3.3.1 Corrosion Rates Measured With Coupled Multielectrode Array Sensors

The experiments for verifying the corrosion rates observed with the weight loss method were conducted using a coated Alloy 22 coupled multielectrode array sensor. The sensor has nine electrodes made with mill-annealed Alloy 22 wires {1 mm [40 mil] in diameter and 150.2 mm [6 in] long}. The wires were coated with an inorganic coating to prevent the formation of a crevice between the wire and the surrounding insulating material (Chiang and Yang, 2007). A schematic diagram of the sensor with coated electrodes is shown in Figure 3-10(a), and a photograph of the sensor after the corrosion tests is shown in Figure 3-10(b).

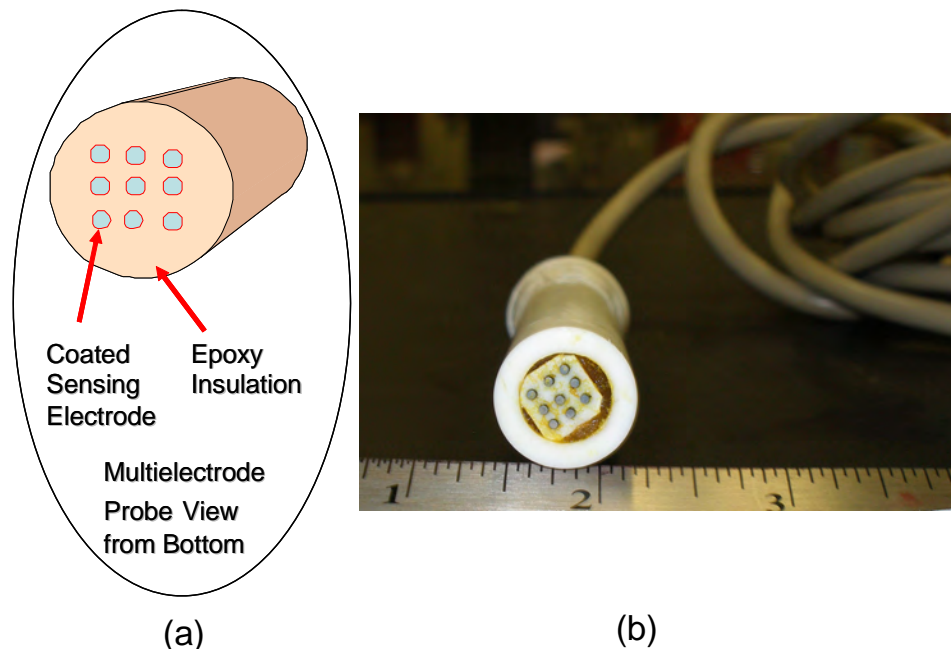


**Figure 3-10. (a) Schematic Diagram of the Coated Multielectrode Array Sensor and (b) Photograph of a Coated Alloy 22 Multielectrode Array Sensor After the Corrosion Test Shown in Figure 3-11**

During the test, the coupled multielectrode array sensor probe was immersed in the liquid phase of a vessel system similar to that shown in Figure 3-2. Reagent grade NaOH and HNO<sub>3</sub> were used to adjust the pH of the liquid in the test vessel.

Figure 3-11 shows the measured maximum corrosion rate [the rate derived from the current that was measured from the most anodic electrode (Yang, 2008; Yang, et al., 2002)] and the pH of the diluted samples. The temperature varied from 124 to 134 °C [255 to 273 °F] and occasionally reached 145 °C [293 °F] during the test. The general corrosion rate, as measured with the weight loss method and shown in Figures 3-7 and 3-9, is anticipated to be lower than the maximum corrosion rate from the multielectrode array sensor. This is because the maximum sensor current is derived from a small electrode {surface area = 0.00785 cm<sup>2</sup> [0.00122 in<sup>2</sup>]} experiencing the most corrosion (Yang, et al., 2002), whereas the corrosion rate from the weight loss tests is averaged over the entire surface area {>2.66 cm<sup>2</sup> [0.412 in<sup>2</sup>]}. The test vessel solution pH was initially adjusted with a dilute NaOH solution so that the diluted sample pH was about 8.5 and the measured maximum corrosion rate of Alloy 22 stabilized at values around 1 μm/yr [0.04 mil/yr] as shown in Figure 3-11. Then dilute nitric acid was added to the test vessel from time to time, and such additions are reflected by the instantaneous decrease in the diluted sample pH. The solution pH increased slowly after each sharp decrease, probably due to the evaporation of the acid in the system. After the diluted sample pH was lowered below 5, the maximum corrosion rate started to increase every time dilute nitric acid was added to the vessel. Figure 3-12 shows the relationship between the maximum corrosion rates and the pH of the diluted sample from the liquid phase. The maximum corrosion rate remained low {about 1 μm/yr [0.04 mil/yr]} over a wide pH range near neutral (from 4.8 to 8.5) and increased exponentially with a decrease in pH when the diluted sample pH became lower than 4.8.

The maximum corrosion rate, as shown in Figure 3-12, is consistent with the general corrosion rate shown in Figure 3-9. Both figures show low corrosion rates for Alloy 22 at pH values greater than 4.8 for the diluted sample and a sharp increase in the corrosion rate of Alloy 22 when the diluted sample pH was lower than 4.5.

Because the current from the most anodic electrode of the coupled multielectrode array sensor indicates nonuniform corrosion, the low rates in Figure 3-12 also show that the localized corrosion rate of Alloy 22 exposed to large quantities of saturated NaCl–KNO<sub>3</sub>–NaNO<sub>3</sub> brine is low {≤1 μm/yr [0.04 mil/yr]} at 130 °C [266 °F] when the pH of the diluted sample is higher than 4.8.

### 3.3.2 Causes for the Variations in the pH of the NaCl–NaNO<sub>3</sub>–KNO<sub>3</sub> Systems

As discussed earlier, the pH of the vent-bubbler water varied significantly even for the vent-bubblers connected to vessels containing the same salts at the same temperature (Vessels B and E). The CO<sub>2</sub> in the air and impurities in the chemical reagents used for the test and their interactions with the salts and the components of the glass vessel (silica and boron) were suspected to cause the pH variations. The experimental setup shown in Figure 3-3 was used to assess the effect of CO<sub>2</sub>. To assess the effect of the impurities and glass components, preliminary model simulations were conducted to understand the influence of these chemical species on the pH of the NaCl–NaNO<sub>3</sub>–KNO<sub>3</sub> solutions.

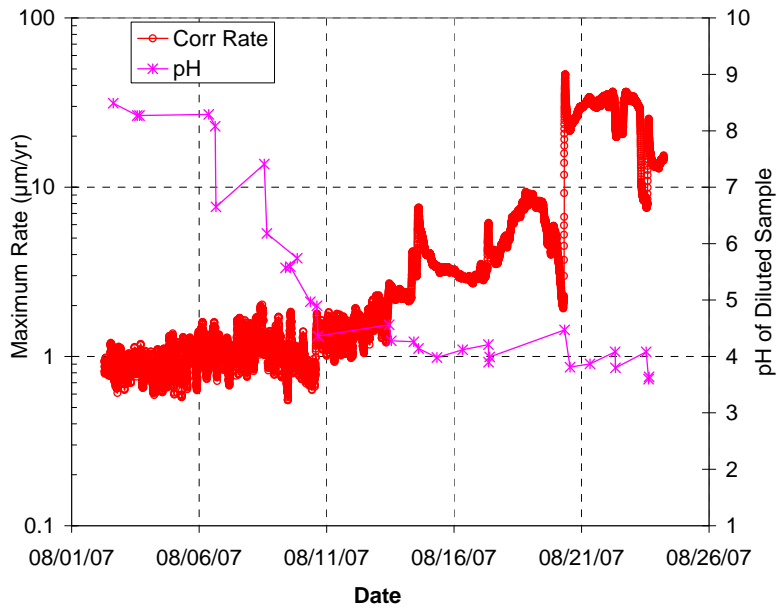


**Figure 3-11. Maximum Corrosion Rates for Alloy 22 Measured With a Coupled Multielectrode Array Sensor at Different pH in the NaCl–NaNO<sub>3</sub>–KNO<sub>3</sub> System at 130 °C [266 °F] (Maximum Corrosion Rate Was Derived From the Highest Anodic Currents Measured From All the Electrodes of the Sensor)**

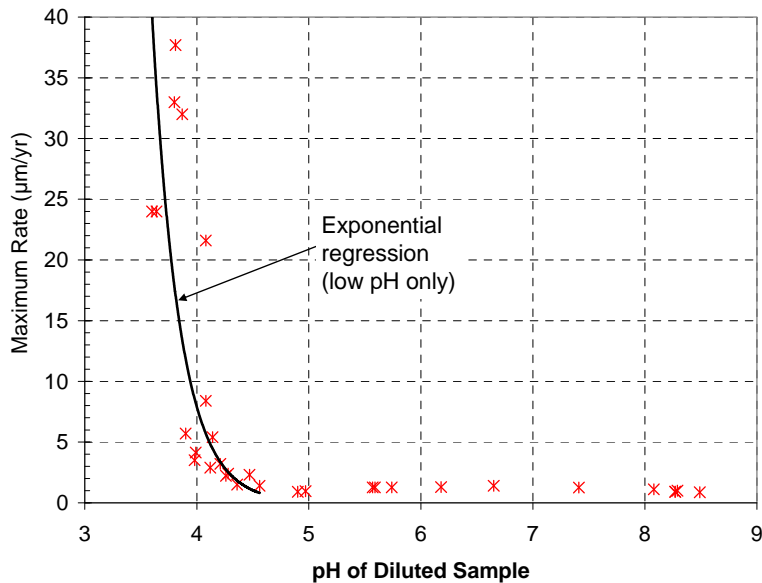


**Figure 3-12. Relationship Between the Maximum Corrosion Rates Measured With the Alloy 22 Coupled Multielectrode Array Sensor and the pH of the Diluted Samples From the Liquid Phase of the NaCl–NaNO<sub>3</sub>–KNO<sub>3</sub> System**

## Effect of CO<sub>2</sub> in Air

Bechtel SAIC Company, LLC (2005) reported that salts containing sodium, chloride, and nitrate ions are not stable in CO<sub>2</sub>-containing environments at temperatures above 100 °C [212 °F]. In such environments, hydrochloric acid or nitric acid will be formed according to the following reactions:

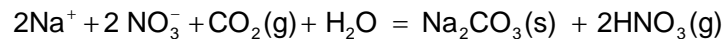
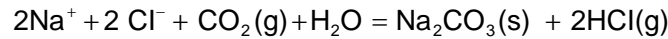


Figure 3-13 shows the condenser water pH as a function of time using the experimental setup shown in Figure 3-3. The venting line was connected to the bubbler, as shown in Figure 3-3, during the first 23 days of the test and opened to the air for the remaining duration of the test. The pH of the condenser water was high initially (7.9), but decreased to 6.9 within the first 15 days. The pH of the condenser water continued to decrease after the venting line was opened to air, but showed no acceleration in the pH decrease. It is not evident from Figure 3-13 that the CO<sub>2</sub> in the open air has caused the pH decrease; moreover, opening the venting line to air did not cause the bubbler pH to decrease to 2 or 3, as observed in Vessel E (Table 3-3). The final pH was close to that of the added deionized water.

To provide a preliminary understanding of the pH changes in a solution containing NaCl, NaNO<sub>3</sub>, and KNO<sub>3</sub> at elevated temperatures, thermodynamic modeling of the chemistry of the salt system was performed, using software developed by OLI Systems, Inc. (see Section 2.3 for more information).

## Model Simulated Effect of Silica

Silica is a primary component of the glass container (about 81 percent SiO<sub>2</sub>) used during the test. Figure 3-14 shows the result of thermodynamic modeling that evaluated the effect of adding SiO<sub>2</sub> on the pH of the NaCl–NaNO<sub>3</sub>–KNO<sub>3</sub> solution. The calculated initial solution pH was 8.0. As SiO<sub>2</sub> was added, the pH decreased and reached 6.6 when SiO<sub>2</sub> reached its solubility limit (337 ppm), which is expected under the test conditions because of silica abundance in the glass and the relatively long test duration. The results indicate that silica did not cause the low pH observed in the liquid phase for some of the tests.

## Model Simulated Effect of Boron

Boron is a major component of the glass container (about 13 percent B<sub>2</sub>O<sub>3</sub>) used in the tests. Figure 3-15 shows the result of thermodynamic modeling that evaluated the effect of adding boron [in the form of B(OH)<sub>3</sub>] on the pH of the NaCl–NaNO<sub>3</sub>–KNO<sub>3</sub> solution. The solution pH decreased from 8.0 to 7.0 when the added B(OH)<sub>3</sub> increased to 210 ppm. The solution pH continued to decrease as more boron was added and reached about 6.5 at a boron content of 500 ppm. The results indicate that boron leached from the glass container could not cause the NaCl–NaNO<sub>3</sub>–KNO<sub>3</sub> solution to attain an acidic pH.

## Model Simulated Effect of Phosphorous

Phosphorous is one of the impurities listed in the specification sheet for the reagents used in the experiments (e.g., 4 ppm PO<sub>4</sub><sup>-</sup> in one of the NaCl batches). Figure 3-16 shows the calculated effect of phosphorous addition (added in the form of P<sub>2</sub>O<sub>5</sub>) on the pH of the NaCl–NaNO<sub>3</sub>–KNO<sub>3</sub>

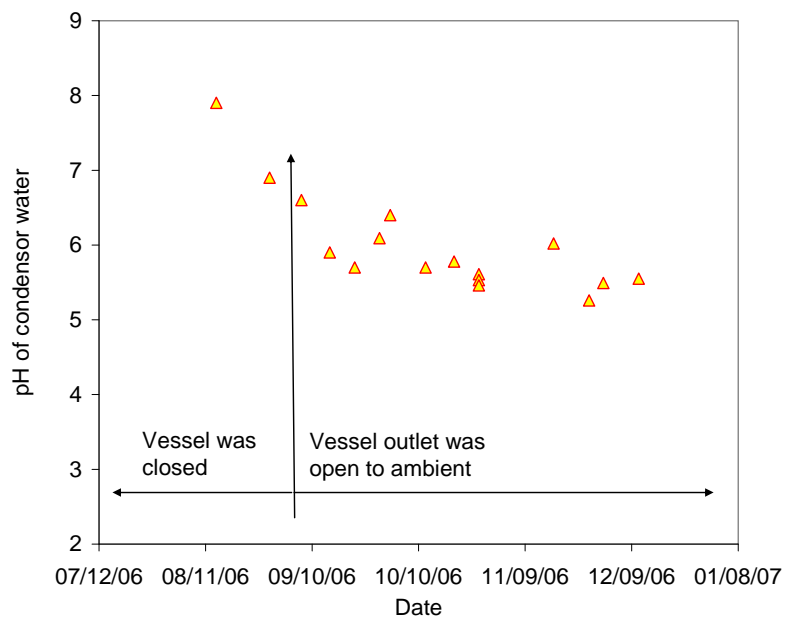


**Figure 3-13. Effect of Atmospheric Components on the pH of the Condenser Water Above the Test Flasks Containing Wet NaCl, NaNO<sub>3</sub>, and KNO<sub>3</sub> Salt Mixtures at 130 °C [266 °F]**

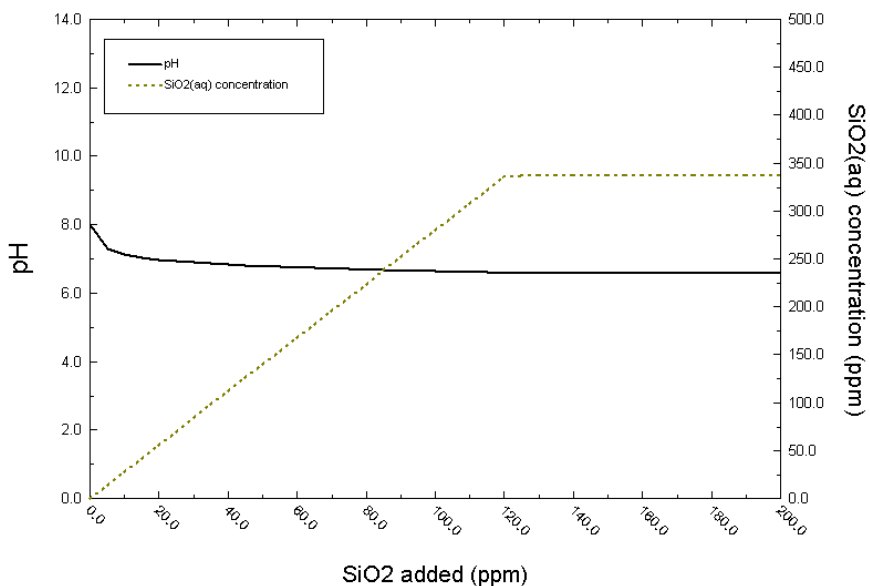


**Figure 3-14. Calculated Effect of Addition of SiO<sub>2</sub> and Dissolved SiO<sub>2</sub> Concentration on the pH of the NaCl–NaNO<sub>3</sub>–KNO<sub>3</sub> Solution at 160 °C [320 °F]**

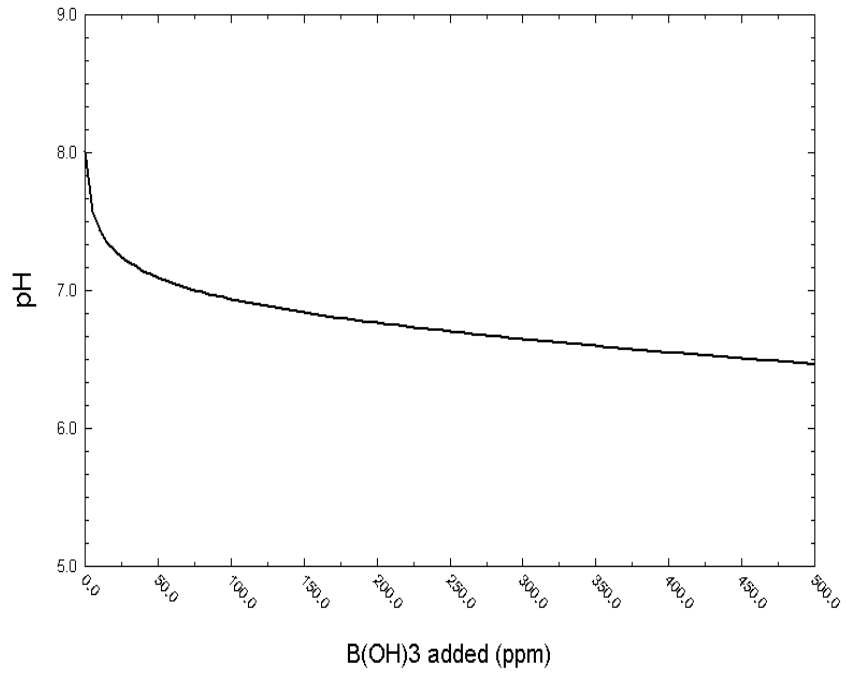


**Figure 3-15. Calculated Effect of the Addition of B(OH)<sub>3</sub> and Dissolved B(OH)<sub>3</sub> Concentration on the pH of NaCl–NaNO<sub>3</sub> Solution at 160 °C [320 °F]**

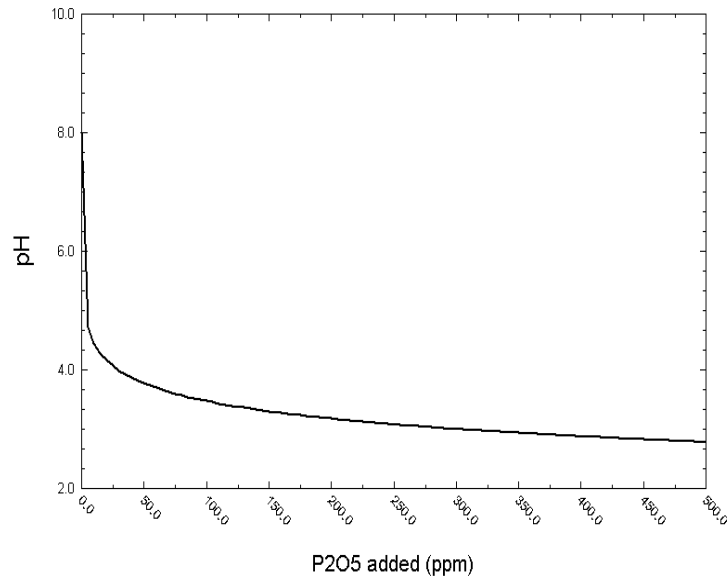


**Figure 3-16. Calculated Effect of the Addition of P<sub>2</sub>O<sub>5</sub> and the Dissolved P<sub>2</sub>O<sub>5</sub> Concentration on the pH of NaCl–NaNO<sub>3</sub>–KNO<sub>3</sub> Solution at 160 °C [320 °F]**

solution. The solution pH decreased sharply from 8.0 to 5.0 with a  $P_2O_5$  content as low as 2.5 ppm. The results indicate that the presence of phosphorus impurity, most likely from the reagent grade chemicals used in the experiments, could have caused the low pH of some of the NaCl–NaNO<sub>3</sub>–KNO<sub>3</sub> solutions.

### Other Impurities

The reagents also contain other impurities that may affect the pH of the solution. For example, the KNO<sub>3</sub> used in the experiment contains 20 ppm calcium and 10 ppm magnesium. If these impurities were in a soluble form such as chlorides or nitrates, they would undergo hydrolysis to form acid at the test temperatures (Pulvirenti, et al., 2004, 2003). In addition, the combination of the impurities mentioned previously (SiO<sub>2</sub>, B, and P) may increase the effect on the pH of the solution.

## 3.4 Summary

Orme, et al. (2004) and Gray, et al. (2006) reported the corrosion rate of Alloy 22 in 1 m NaCl and 4 m NaCl solutions containing different concentrations of hydrochloric, sulfuric, or nitric acid at 90 °C [194 °F] measured using electrochemical linear polarization resistance and electrochemical impedance spectroscopy. Figure 3-17(a) shows the dependence of the corrosion rate on the solution pH in 4 m NaCl solution. The solution pH values in Figure 3-17(a) were the theoretical values calculated with EQ3/6 thermodynamic software (Gray, et al., 2006). The corrosion rate was lower {less than 1  $\mu\text{m}/\text{yr}$  [0.04 mil/yr]} at pH values higher than 2, but started to increase as the pH decreased below 2. The increase in corrosion rate was moderate for nitric acid—increasing to approximately 10 to 25  $\mu\text{m}/\text{yr}$  [0.4 to 1 mil/yr] when pH ranged between 1.5 and 0.5 and to approximately 40  $\mu\text{m}/\text{yr}$  [1.6 mil/yr] when pH was –0.2—but significant for hydrochloric and sulfuric acids {from less than 1  $\mu\text{m}/\text{yr}$  [0.04 mil/yr] to 3,000  $\mu\text{m}/\text{yr}$  [120 mil/yr] at pH 1.0}. The relatively low corrosion rate observed in the presence of nitric acid was attributed to the passive oxide film formed on the Alloy 22 specimen by the nitric acid. The passive behavior of the oxide film formed in the presence of nitric acid is also indicated by the high values of the open circuit potential [Figure 3-17(b)].

In the immersion tests and the test conducted with coupled multielectrode array probes, the critical pH at which the corrosion rate increased significantly in the NaCl–KNO<sub>3</sub>–NaNO<sub>3</sub> system was 4.5 for the solution that was diluted tenfold by weight and cooled to room temperature (Figures 3-9 and 3-11). The pH obtained from the diluted sample cannot be directly compared with the pH reported by Orme, et al. (2004), but the pH values for the undiluted solutions at the testing temperatures can be measured directly with a high temperature pH probe or calculated using thermodynamic software such as EQ3/6.

Pulvirenti, et al. (2004, 2003) also conducted corrosion rate measurements for Alloy 22 in concentrated brines obtained by evaporating solutions containing Mg<sup>2+</sup>, Ca<sup>2+</sup>, Na<sup>+</sup>, K<sup>+</sup>, Cl<sup>–</sup>, and NO<sub>3</sub><sup>–</sup>. Because of the hydrolysis of the alkaline earth metals, Cl<sub>2</sub>, NO, NO<sub>2</sub>, HCl, and HNO<sub>3</sub> were detected in the vapor phase of the system during evaporation. The pH of the vapor condensate and the residue liquid were close to 1 or less. The corrosion rates of Alloy 22 were on the order of 5 to 100  $\mu\text{m}/\text{yr}$  [0.2 to 4 mil/yr] over the temperature range of 110 to 145 °C [230 to 293 °F]. Pitting corrosion was also observed in some of the specimens. The high corrosion rates reported by Pulvirenti, et al. (2004, 2003) are consistent with the corrosion rates measured in the low pH range, as shown in Figures 3-9 and 3-12.

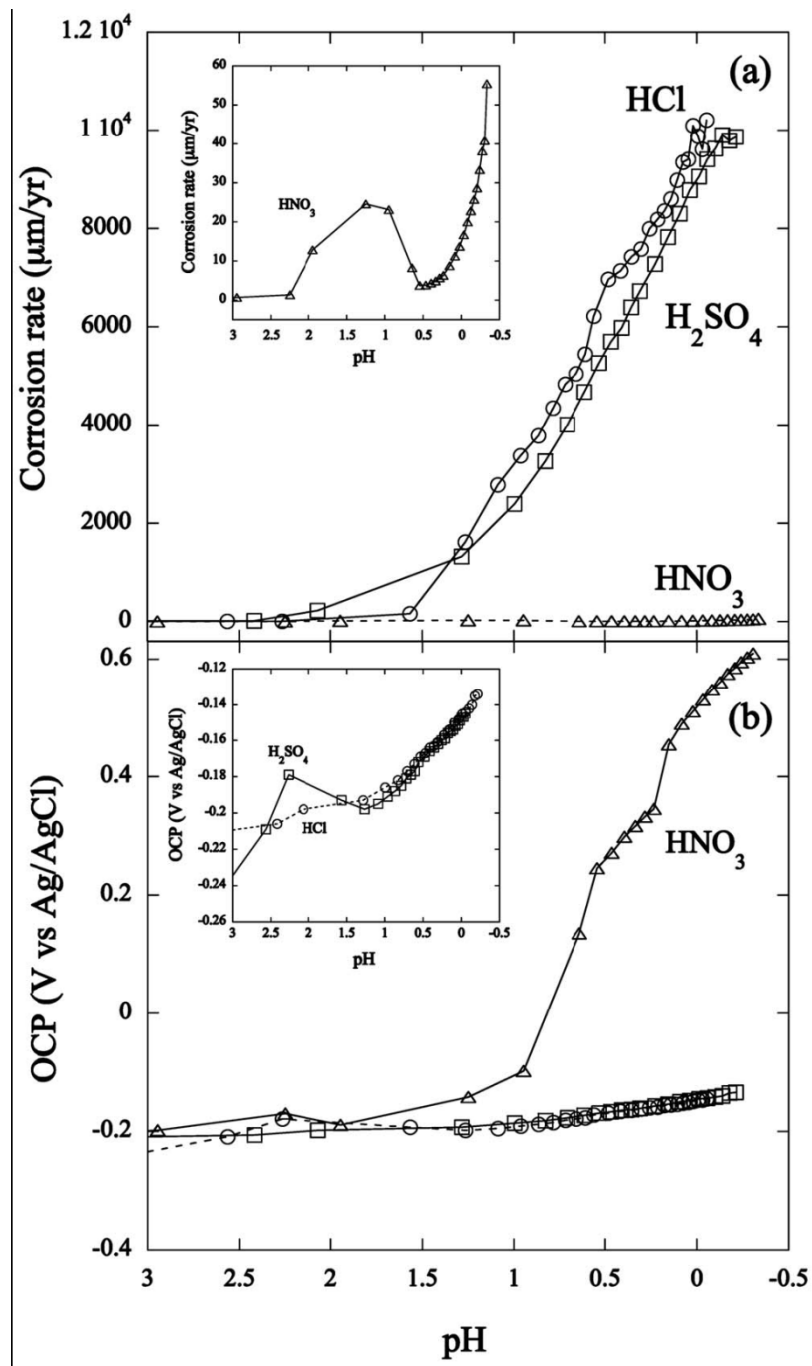


Figure 3-17. (a) Corrosion Rates and (b) Open Circuit Potential Versus pH for Alloy 22 in Hydrochloric (Circles), Sulfuric (Squares), and Nitric (Triangles) With 4 m NaCl at 90 °C [194 °F]

Manufacturers of Alloy 22 have reported the corrosion rate of Alloy 22 below or at boiling temperatures slightly over 100 °C [212 °F] in a wide range of chemical solutions (Haynes International, 2002). According to Haynes International, the corrosion rate of Alloy 22 in dilute nitric acid (10 weight percent) at temperatures up to the boiling temperature is relatively low {25  $\mu\text{m}/\text{yr}$  [1 mil/yr]}. However, the general corrosion rate of Alloy 22 in hydrochloric solutions varies from 75 to 10,000  $\mu\text{m}/\text{yr}$  [3 to 400 mil/yr] when the concentration changes from 1 to 10 wt percent at boiling temperatures. In a solution containing 4.9 wt percent  $\text{HNO}_3$  and 0.125 wt percent HCl, the corrosion rate of Alloy 22 was 50  $\mu\text{m}/\text{yr}$  [2 mil/yr] at boiling temperature.

The experimental results reported in this chapter conclude that the  $\text{NaCl-NaNO}_3\text{-KNO}_3$  system is not corrosive toward Alloy 22, exhibiting a general corrosion rate less than 1  $\mu\text{m}/\text{yr}$  [.0.4 mil], unless the pH is lower than 4.8 as measured at room temperature for the brine solution that was diluted 10 times by weight. Only at a pH lower than 4.8 can high corrosion rates be expected.

### 3.5 References

ASTM International. "Standard Practice for Preparing, Cleaning, and Evaluating Corrosion Test Specimens." G1-03. West Conshohocken, Pennsylvania: ASTM International. 2005.

Bechtel SAIC Company, LLC. "Analysis of Dust Deliquescence for FEP Screening." Report ANL-EBS-MD-00007. Rev. 01. Las Vegas, Nevada: Bechtel SAIC Company, LLC. 2005.

Chiang, K.T. and L. Yang. "Development of Crevice-Free Multielectrode Sensors for Elevated Temperature." Paper No. 07376. CORROSION/2007. Houston, Texas: NACE International. 2007.

Dixit, S., S. Roberts, K. Evans, T. Wolery, and S. Carroll. "General Corrosion and Passive Film Stability." UCRL-TR-217393. Livermore, California: Lawrence Livermore National Laboratory. 2006.

Dunn, D.S., O. Pensado, Y.-M. Pan, R.T. Pabalan, L. Yang, X. He, and K.T. Chiang. "Passive and Localized Corrosion of Alloy 22—Modeling and Experiments." CNWRA 2005-02. San Antonio, Texas: CNWRA. 2005.

Gray, J.J., J.R. Hayes, G.E. Gdowski, B.E. Viani, and C.A. Orme. "Influence of Solution pH, Anion Concentration, and Temperature on the Corrosion Properties of Alloy 22." *Journal of the Electrochemical Society*. Vol. 153. No. 3. pp. B61-B67. 2006.

Haynes International. "HASTELLOY C-22 Alloy." Bulletin H-2019F. Kokomo, Indiana: Haynes International. 2002.

Orme, C.A., J. Gray, J. Hayes, L. Wong, R. Rebak, S. Carroll, J. Harper, and G. Gdowski. "Fiscal Year 2004 Summary Report: General Corrosion and Passive Film Stability." UCRL-TR-208588. Livermore, California: Lawrence Livermore National Laboratory. 2004.

Pulvirenti, A., K. Needham, M. Adel-Hadadi, A. Barkatt, C. Marks, and J. Gorman. "Multi-Phase Corrosion of Engineered Barrier Materials." Proceedings of the CORROSION 2004 Conference. Paper No. 694. Houston, Texas: NACE International. 2004.

Pulvirenti, A., K. Needham, M. Adel-Hadadi, E. Bishop, A. Barkatt, C.R. Marks, and J.A. Gorman. "Corrosion Behavior of Alloy 22 Under Conditions of Dynamic Groundwater Composition." Proceedings of the CORROSION 2003 Conference. Paper No. 693. Houston, Texas: NACE International. 2003.

Sandia National Laboratories. "Analysis of Dust Deliquescence for FEP Screening." ANL-EBS-MD-000074. Rev. 01 AD 01. Las Vegas, Nevada: Sandia National Laboratories. 2007a.

———. "Multiscale Thermohydrologic Model." ANL-EBS-MD-000049. Rev. 03 AD01. Las Vegas, Nevada: Sandia National Laboratories. 2007b.

———. "General and Localized Corrosion of Waste Package Outer Barrier." ANL-EBS-MD-000003. Rev. 03. Las Vegas, Nevada: Sandia National Laboratories. 2007c.

Wang, P., R.D. Springer, A. Anderko, and R.D. Young. "Fluid Phase Equilibria." Proceedings of 15<sup>th</sup> Symposium on Thermophysical Properties, Boulder, Colorado, June 22–27, 2003. Vol. 222/223. Boulder, Colorado: University of Colorado. p. 11. 2004.

Yang, L. "Multielectrode Systems." *Techniques for Corrosion Monitoring*. Chapter 8. L. Yang, ed. Cambridge, England: Woodhead Publishing. 2008.

Yang, L. "Corrosion of Alloy 22 in Concentrated Nitrate and Nitrate and Chloride Salt Environments at Elevated Temperature—Progress Report." CNWRA 2006-02. San Antonio, Texas: CNWRA. 2006.

Yang, L., D. Dunn, G. Cragolino, X. He, Y.-M. Pan, A. Csontos, and T. Ahn. "Corrosion Behavior of Alloy 22 in Concentrated Nitrate and Chloride Salt Environments at Elevated Temperatures." CORROSION/2007. Paper No. 07580. Houston, Texas: NACE International. 2007.

Yang, L., N. Sridhar, O. Pensado, and D. Dunn. "An *In-situ* Galvanically Coupled Multi-Electrode Array Sensor for Localized Corrosion." *Corrosion*. Vol. 58. p. 1,004. 2002.

## 4 LOCALIZED CORROSION OF ALLOY 22 IN DUST DELIQUESCENT BRINES

This chapter focuses on understanding the localized corrosion of Alloy 22 in dust deliquescence brines. As reported in Chapter 2, dust deliquescence brines are expected to be rich in nitrate ions. In seepage water brines, nitrate acts as a localized corrosion inhibitor (Dunn, et al., 2005). This chapter summarizes the reported experimental data relating to localized corrosion of Alloy 22 in dust deliquescence brines. The review is primarily based upon the reports by Felker, et al. (2006) and Dixit, et al. (2006). Additional references are also included where applicable. The experimental data show a strong tendency to localized corrosion inhibition of the alloy with increasing brine temperature. This result is based upon the values of corrosion potential and repassivation potentials that are reported in Sections 4.1 and 4.2.

A mathematical model of the localized corrosion process simulating the cathodic side of the process is presented in Section 4.3. The current generated at the cathodic site is referred to as cathodic capacity. Model parameters used for estimating the cathodic capacity are discussed, and the cathodic capacity of Alloy 22 in various dust deliquescence brines is calculated for varying brine amounts at different temperatures. Finally, the work reported in this chapter and conclusions drawn from that work are provided in Section 4.4.

### 4.1 Electrochemical Test Data on Localized Corrosion in Large Quantity of Brines

Both corrosion and repassivation potentials are important electrochemical parameters with respect to localized corrosion. It has been long established that localized corrosion in the form of crevice corrosion could initiate if the corrosion potential is greater than the repassivation potential after long exposure of the metal in a test solution (Shukla, 2008). The studies on the localized corrosion susceptibility of Alloy 22 in aqueous solutions of chloride and nitrate salts of sodium and potassium in the temperature range of 110–150 °C [230–302 °F] by measuring the repassivation and corrosion potentials were reported by Felker, et al. (2006).

As Felker, et al. (2006) reported, a three-electrode electrochemical cell consisting of a Pyrex™ corrosion cell, a working electrode, an auxiliary electrode, and a suitable reference electrode [saturated silver/silver chloride (SSC)<sup>†</sup> or saturated calomel electrode (SCE)<sup>†</sup>] through a Luggin capillary was used. Carbon dioxide free air was purged through a dispenser immersed in the solution. A condenser was used to condense the vapors formed due to evaporation of the test solution. Specimens were cleaned sequentially with distilled water, hexane, acetone, and methanol (or ethanol) prior to testing. Nonwelded Alloy 22 prism specimens were used in the experimental studies. Standard ASTM procedures (G 5 and G 59) were followed for conducting the potentiostatic, potentiodynamic, and corrosion potential measurements.

The aqueous solutions were made using the chloride and nitrate salts of sodium and potassium. As stated in the report by Felker, et al. (2006), the chloride-dominated aqueous solutions existed only below 116 °C [240.8 °F]. In these solutions, the maximum nitrate salt solubility was determined. For solutions in which nitrate ions dominate the solutions, the maximum amount of soluble chloride was determined. It was observed that the nitrate-dominated solutions can

---

<sup>†</sup>Saturated silver/silver chloride reference electrode is referenced frequently throughout this chapter; therefore, the acronym SSC will be used. This acronym is predominantly used as a subscript.

<sup>†</sup>Saturated calomel electrode is referenced frequently throughout this chapter; therefore, the acronym SCE will be used. This acronym is predominantly used as a subscript.

exist at temperatures much higher than 116 °C [240.8 °F] because of the very high boiling points of the mixed nitrate salt solutions.

The corrosion potential measurements were conducted in the test solution containing 25m NO<sub>3</sub><sup>-</sup> + 1m Cl<sup>-</sup> at 110 °C [230 °F]. The pH of the solution was adjusted and varied between 2 and 7. These results are shown in Figure 4-1. As seen in the figure, the  $E_{corr}$  values for the solution with pH equal to 2 are several hundred mV higher than the  $E_{corr}$  values in solutions with higher pH.  $E_{corr}$  is about -100 mV<sub>SSC</sub> in the neutral solution and increases by 100 mV for solutions with pH equal to 3. However, there is a sudden increase in  $E_{corr}$  for the test solution with pH equal to 2. At this pH, the nitrate becomes a dominant reductive species in solution.

The values of the repassivation potential  $E_{rp}$  reported by Felker, et al. (2006) are summarized in Table 4-1. The repassivation potential  $E_{rp}$  versus NO<sub>3</sub><sup>-</sup>/Cl<sup>-</sup> for different temperatures is graphically represented in Figure 4-2 where open and partially open symbols represent  $E_{rp}$  of Alloy 22 in test solutions with neutral and acidic pH, respectively. As seen in the Figure 4-2,  $E_{rp}$  increases with increasing NO<sub>3</sub><sup>-</sup>/Cl<sup>-</sup> at a fixed temperature. Also note that  $E_{rp}$  values vary within a range of 0.383 to 0.522 V<sub>SSC</sub> at NO<sub>3</sub><sup>-</sup>/Cl<sup>-</sup> ratio and temperature equal to 1 and 110 °C [230 °F], respectively, and  $E_{rp}$  values for solution pH equal to 4 lie within 0.383 to 0.522 V<sub>SSC</sub>. Similar variations can be observed for  $E_{rp}$  values at NO<sub>3</sub><sup>-</sup>/Cl<sup>-</sup> equal to 10.5 where  $E_{rp}$  values lie between 0.54 and 0.683 V<sub>SSC</sub>. In this case, the  $E_{rp}$  value for solution pH equal to 4.0 is at the lower end of the range. Therefore, the solution pH does have a statistically significant effect on  $E_{rp}$  values. Furthermore,  $E_{rp}$  reaches the asymptotic value 0.773 and 0.685 V<sub>SSC</sub> in the test solution containing only nitrate ions at 110 and 125 °C [230 and 257 °F], respectively.

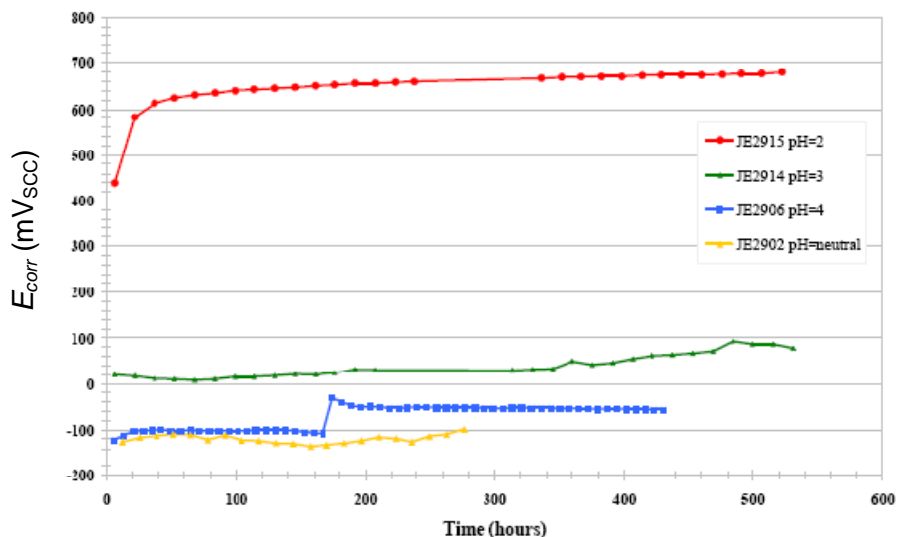


**Figure 4-1. Corrosion Potential Versus Time of Alloy 22 in 25m NO<sub>3</sub><sup>-</sup> + 1m Cl<sup>-</sup> Solution With the pH Adjusted to Different Values at 110 °C [230 °F]. The Legend on the Graph Represents the Test Solution Identification Numbers (JE2915, JE2914, JE2906, and JE2902) and Corresponding Solution pH (Felker, et al., 2006).**

Temperature (°C) [°F]	pH	Cl <sup>-</sup> (molal)	NO <sub>3</sub> <sup>-</sup> (molal)	NO <sub>3</sub> <sup>-</sup> /Cl <sup>-</sup> (molal ratio)	$E_{rp}$ V <sub>SSC</sub>
110 [230]	Neutral	8	0	0	-0.200
110 [230]	Neutral	8	0	0	-0.182
110 [230]	Neutral	8	0.8	0.1	-0.047
110 [230]	Neutral	8	0.8	0.1	-0.096
110 [230]	Neutral	8	1.6	0.2	-0.017
110 [230]	Neutral	8	2.4	0.3	0.320
110 [230]	Neutral	8	4	0.5	0.328
110 [230]	Neutral	6	6	1	0.383
110 [230]	Neutral	6	6	1	0.522
110 [230]	Neutral	2	42	21	0.674
110 [230]	Neutral	1	42	42	0.690
110 [230]	Neutral	0	42	NA	0.773
110 [230]	4	8	0	0	-0.207
110 [230]	4	8	0.8	0.1	-0.097
110 [230]	4	8	4	0.5	0.443
110 [230]	4	6	6	1	0.444
110 [230]	4	6	6	1	0.480
110 [230]	4	4	42	10.5	0.654
110 [230]	4	2	42	21	0.661
110 [230]	4	1	42	42	0.661
125 [257]	Neutral	4	42	10.5	0.622
125 [257]	Neutral	4	42	10.5	0.683
125 [257]	Neutral	2	42	21	0.595
125 [257]	Neutral	1	42	42	0.608
125 [257]	Neutral	0	42	NA	0.685
125 [257]	4	4	42	10.5	0.540
125 [257]	4	2	42	21	0.590
125 [257]	4	1	42	42	0.685
140 [284]	4	1	72	72	0.640
140 [284]	Neutral	1	72	72	0.725
140 [284]	Neutral	3	76	25.3	0.623
140 [284]	Neutral	3	76	25.3	0.656
150 [302]	Neutral	1	100	100	0.671

\*Felker, S., P.D. Hailey, T. Lian, K.J. Staggs, and G. Gdowski. "Alloy 22 Localized Corrosion Susceptibility in Aqueous Solutions of Chloride and Nitrate Salts of Sodium and Potassium at 110–150 °C." UCRL-TR-218195. Livermore, California: Lawrence Livermore National Laboratory. 2006.

$E_{rp}$  values lie above 0.383 V<sub>SSC</sub> irrespective of temperature and solution pH for NO<sub>3</sub><sup>-</sup>/Cl<sup>-</sup> ratios greater or equal to 1. In test solutions with such high values of  $E_{rp}$ , the localized corrosion could initiate only if solution pH is close to 2 (see Figure 4-1). This conclusion is based upon observations that the corrosion potential of Alloy 22 in test solutions containing 25m NO<sub>3</sub><sup>-</sup> and 1m Cl<sup>-</sup> with pH equal to 2 could reach as high as 0.7 V<sub>SSC</sub>. Similarly,  $E_{rp}$  values lie below 0 V<sub>SSC</sub> if the NO<sub>3</sub><sup>-</sup>/Cl<sup>-</sup> ratios are equal to or less than 0.2, and localized corrosion is possible (see Figure 4-1) if the solutions pH is close to 3.

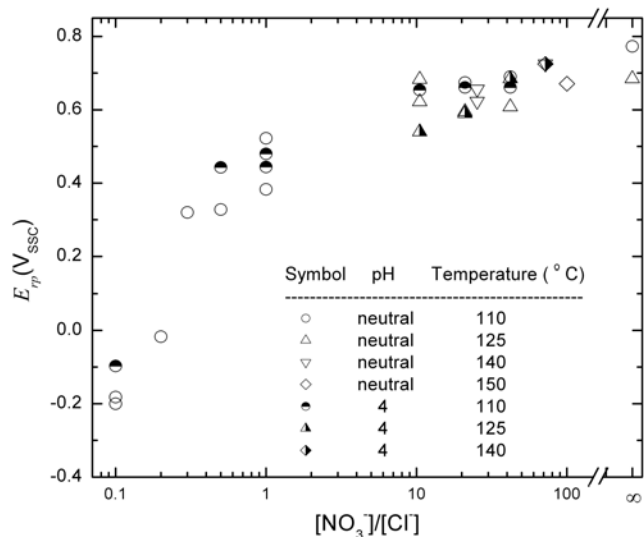


**Figure 4-2. Graphical Representation of the  $E_{rp}$  Data Tabulated in Table 4-1**

Rebak (2006) presented an additional experimental data point on repassivation potential in 100 m  $\text{NO}_3^-$  and 3 m  $\text{Cl}^-$  test solution at 150 °C [302 °F]. This data point is not included in the Felker, et al. (2006) report. The Rebak (2006) reported value of repassivation potential of Alloy 22 in the test solution is close to 0.7  $V_{SSC}$ . The pH of the solution was not reported.

Yang (2006) reported the short-term corrosion potential  $E_{corr}$  for mill-annealed and welded plus solution-annealed Alloy 22 specimens in a brine saturated by a  $\text{NaCl-KCl-NaNO}_3$  salt mixture under semiopen conditions. The corrosion potential  $E_{corr}$  values lie in the range of 0.17 and 0.37  $V_{SCE}$  at 160 °C [320 °F]. Although there is a difference of 0.045V between SCE and SSC, the difference is insignificant as compared to measurement uncertainties in corrosion and repassivation potentials.

As discussed in Chapter 2, the brines that are likely to form during the deliquescence period contain a high  $\text{NO}_3^-/\text{Cl}^-$  molar ratio (higher than 5) at or above 120 °C [248 °F]. Therefore, dust deliquescence brine-induced localized corrosion is unlikely based on the measurements of corrosion and repassivation potentials, unless the solution has a sustainable low pH close to 2. At temperatures between 100 and 120 °C [212 and 248 °F], however, some brines that may develop during the deliquescence period may have nitrate-to-chloride ratios below 0.1, but the ratio of total inhibitors (nitrate + sulfate + bicarbonate + carbonate) to chloride is still high (higher than 3.3 for the  $\text{KCl-KNO}_3$  system). Based on the measurements of corrosion and repassivation potentials in pure nitrate and chloride solutions, localized corrosion is possible for nitrate-to-chloride molar ratios at or below 0.2. It is not clear, however, whether the repassivation potential will be higher than the corrosion potential for systems containing low nitrate but high concentrations of the other anion such as sulfate, bicarbonate, and carbonate, which were shown to be localized corrosion inhibitors at 95 °C [203 °F] (Dunn, et al., 2005).

## 4.2 Immersion Test Data on Localized Corrosion in Large Quantity of Brines

Dixit, et al. (2006) conducted localized corrosion tests using crevice assemblies specimens partially submerged in Na–K–Cl–NO<sub>3</sub> brines. The experiments were conducted in a 2 L [0.44 gal] Alloy 276 autoclave under a slight pressure at 160 and 220 °C [320 and 428 °F]. A specimen holder made of Alloy 22 was used inside each autoclave. The Alloy 22 specimens were not electrically isolated from the Hastelloy C–276. Specimens were held in a vertical position to minimize settling of secondary precipitates on the Alloy 22 specimens.

The experimental setup was assembled by first adding 1 L [0.22 gal] of brine solution in the autoclave at 90 °C [194 °F]. The assembled specimen holder was placed such that half of the specimen was fully immersed in liquid and the other half was fully exposed to the vapor phase above the liquid. The autoclave was then sealed, and the solution was purged with nitrogen for 1 hour at 100 °C [212 °F] to remove oxygen and carbon dioxide gases. Dixit, et al. (2006) reported that at high temperatures and high nitrate concentrations, nitrate will be the most readily available oxidant for Alloy 22 corrosion. Test solutions were prepared by mixing the sodium nitrate and sodium chloride such that the NO<sub>3</sub><sup>-</sup> / Cl<sup>-</sup> molal ratio was 7.4 at 160 °C [320 °F], and NO<sub>3</sub><sup>-</sup> / Cl<sup>-</sup> ratio of 0.5 and 7.4 at 220 °C [428 °F]. Three autoclaves were used to test these three solutions, and 30 specimens were tested in each autoclave. The 30 specimens for each autoclave consisted of 8 pucks (of which 4 were immersed in the solution and 4 were exposed to the vapor phase), 12 weight loss foils, and 10 creviced foils. The autoclaves were heated to get the desired temperature, and the experiment ran continuously for 267 days (≈ 9 months).

Dixit, et al. (2006) observed crevice corrosion on specimens immersed in the solution and on specimens held in the vapor phase at all conditions [i.e., in test solutions with NO<sub>3</sub><sup>-</sup> / Cl<sup>-</sup> molal ratio equal to 7.4 at 160 °C [320 °F]] and in test solutions with NO<sub>3</sub><sup>-</sup> / Cl<sup>-</sup> molal ratio equal to 7.4 and 0.5 at 220 °C [428 °F]. All the creviced specimens in the three autoclaves showed crevice corrosion initiation. Crevice corrosion penetration depths were not quantified due to experimental difficulties.

Lee and Solomon (2006) also reported localized corrosion for Alloy 22 disc specimens held at 200 °C [392 °F] under dripping conditions in ambient pressure to simulate the potential Yucca Mountain condition. The dripping solution was the 10-time diluted standard simulated saturated water which contains NO<sub>3</sub><sup>-</sup>, Cl<sup>-</sup>, Na<sup>+</sup>, and K<sup>+</sup> (with a molar ratio of 21.1:3.6: 21.1:3.6). Unlike the tests reported by Dixit, et al. (2006), which were conducted in closed autoclaves, the Lee and Solomon (2006) dripping test was conducted in an open system where air was expected to be present. A liquid pool was observed on the top surface of the specimen during the dripping test, and the measured temperature of the pool was 143 °C [289.4 °F]. Because the relative humidity was low under the test conditions, the solution above the Alloy 22 specimen was expected to be rich in NO<sub>3</sub><sup>-</sup>. However, pits were observed on the Alloy 22 surface that was in contact with the solution during the test. A scanning electron microscope image reveals that the size of the pits was as large as 10 μm [0.39 mil] after 3 hours of exposure.

As is evident from these studies, localized corrosion did initiate in immersion tests in both closed autoclaves and open dripping environments for Alloy 22 specimens in the nitrate-rich solution. Crevice corrosion was also observed for specimens exposed to the vapor phase of the autoclave containing the nitrate-rich brine solutions. These observations appear to contradict

the electrochemical test results reported in the previous section, which concluded that the localized corrosion initiation is inhibited in nitrate-rich brine solutions.

### 4.3 Localized Corrosion Model for Alloy 22 in Dust Deliquescence Brines Under Potential Repository Conditions

In localized corrosion processes, metal corrodes at certain preferential sites at an accelerated rate. The localized corrosion of Alloy 22 in the dust deliquescence brines can occur in the form of crevice corrosion when the corrosion potential is greater than the repassivation potential. This condition can be represented by the following expression

$$E_{corr} - E_{rp} > 0 \quad (4-1)$$

where

$E_{corr}$  — corrosion potential [V]  
 $E_{rp}$  — repassivation potential for localized corrosion initiation [V]

It is further assumed that the crevice corrosion instantaneously initiates when the corrosion potential exceeds the repassivation potential. The choice of repassivation potential for crevice corrosion initiation is based upon several experimental observations reported in the literature for nickel-based alloys (Dunn, et al., 2000; Kolts and Sridhar, 1984).

The localized corrosion sites will remain active as long as the corrosion potential exceeds the repassivation potential (Dunn, et al., 2005, 2003; Hua, et al., 2004) and there is sufficient cathodic current available to balance the anodic currents generated by metal dissolution reactions (Cui, et al., 2005; Kelly, et al., 2006). In the absence of either condition, localized corrosion could stifle and even repassivation may occur. For example, if the corrosion potential of Alloy 22 in a given dust deliquescence brine is greater than the repassivation potential, but the available cathodic capacity is of the order of the passive current density, then the localized corrosion sites are likely to corrode at the rate of general corrosion. Therefore, the sufficient cathodic current is necessary for achieving the high dissolution rates required to maintain the localized corrosion sites.

In contrast to general corrosion, the cathodic and anodic reaction sites are physically separated in the crevice corrosion process. A schematic diagram of the crevice corrosion process depicting the physical separation of the anodic and cathodic regions is presented in Figure 4-3. Cathodic reactions dominate in the cathodic area, and the excess current generated in the cathodic area is referred to as cathodic capacity. The oxygen reduction reaction is the dominant cathodic reaction within the expected range of environmental conditions at the potential repository drift environment, and a sufficient cathodic capacity is needed for sustained propagation of crevice corrosion at a sufficiently high rate.

The cathodic capacity is affected by the following factors: (i) electrochemical conditions, such as corrosion potential and repassivation potential; (ii) environmental conditions such as temperature, pH, and chemical composition of brines; (iii) quantity of available electrolytes; and (iv) oxygen reduction kinetics.

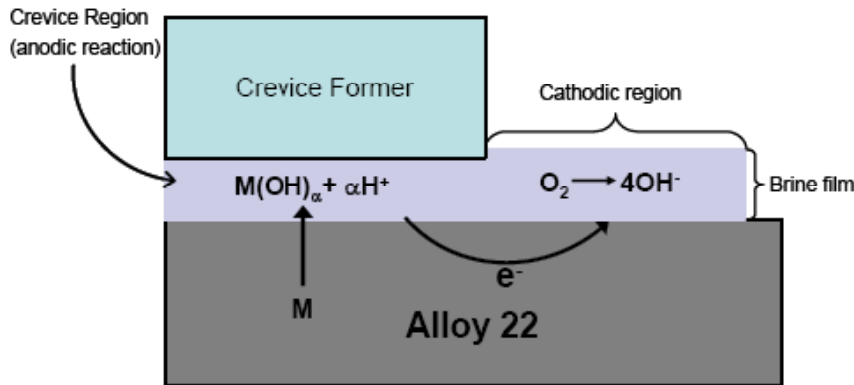


**Figure 4-3. Schematic Diagram of the Crevice Corrosion Process. The Anodic Reactions Predominantly Occur in the Crevice Region, Whereas Cathodic Reactions Dominate in the Cathodic Region Located Adjacent to the Crevice.**

This section focuses on estimating the role of brine quantity in the cathodic capacity. In the potential repository environment, DOE expects that only a limited quantity of dust (Bechtel SAIC Company, LLC, 2005) would accumulate at the waste package surface after the permanent closure. As a result, only a limited quantity of brine would be available for localized corrosion. Because the available dust is expected to be uniformly distributed on the waste package surface, DOE assumes that the dust deliquescence brine would be also uniformly distributed. DOE expects that the thickness and length of the brine film would play a major role in determining the cathodic capacity. At constant ionic conductivity and brine film length, the resistance to ionic flow and the corresponding ohmic potential drop increases as the brine film thickness decreases. For this reason, the effect of the characteristics of brine films on cathodic capacity should be evaluated. To this end, a one-dimensional physic-chemical process model was developed to estimate the cathodic capacity. The interplay of oxygen reduction kinetic phenomenon with brine quantity was integrated into the model to calculate the electrode potential and current distribution in the cathodic region as a function of film height, length, and electrochemical and environmental conditions for dust deliquescence brines. The current distribution in the cathodic region was then integrated to obtain the cathodic capacity for a given set of conditions. The information generated from cathodic capacity calculations is used to estimate the crevice penetration rate for a fixed area of the crevice site.

#### **4.3.1 Model Development**

A process-level model for calculating the cathodic capacity is presented in this section. As seen in Figure 4-3, the anodic and cathodic regions are physically separated. The crevice region is anticipated to become deficient in oxidants due to the physical barrier to diffusional flow created by the restricted geometry of the crevice former once the oxidant is consumed. As a result, the metal dissolution reaction dominates in the crevice region, whereas cathodic reactions dominate in the area adjacent to the crevice. As depicted in Figure 4-3, the anodic dissolution reactions

predominantly occur in the crevice region formed underneath the crevice former. A generic form of the metal dissolution reaction can be represented by the following expression:



where metal  $M$  reacts with the water molecules to produce metal hydroxide, hydrogen ions, and free electrons.

In the potential Yucca Mountain repository environment, the dominant oxidant would likely be oxygen. In the region outside the crevice, the oxygen reduction reaction would take place under mild oxidizing conditions in neutral-to-alkaline aerated solutions. This reaction can be expressed as



In acidic solutions, the dissolved oxygen molecules are reduced according to the following expression



It is assumed that even in acidic solutions, the contribution of the hydrogen evolution reaction is negligible compared to that of oxygen reduction. This assumption is justifiable because the equilibrium potential of the hydrogen evolution reaction is much lower than that of the oxygen reduction reaction (Bard and Faulkner, 1980). For the same reason, the contribution of the water reduction reaction to the cathodic current in neutral-to-alkaline solutions is expected to be negligible.

Nitrate reduction may also be an important reduction reaction in acidic solutions, but not in neutral-to-alkaline solutions. This pH dependence of nitrate reduction can be inferred from the results of corrosion potential measurements on Alloy 22 similar to those presented in Figure 4-1. In addition, the values of general corrosion rates of Alloy 22 presented in Chapter 3 indicate that there is a marked increase in corrosion rate in low pH solutions. This increase in corrosion rate in acidic solution is attributed to reduction in nitrate.

Dunn, et al. (2005) reported corrosion studies at lower temperatures, demonstrating that nitrate is an important inhibitor of localized corrosion of Alloy 22 and suggesting that nitrate reduction is not an important reduction reaction except at very acidic pHs (< 2.0). Because the probability of having a low pH (i.e., pH < 6) dust deliquescence brine is much lower than having a high pH solution in the potential Yucca Mountain repository environment (Yang, 2006), this study assumes that the dominant reduction reaction [as stated by Eq. (4-3)] involves only dissolved oxygen.

Under a steady-state crevice corrosion process, the sum of net current generated by the anodic and cathodic reactions must be equal to zero to maintain charge neutrality. This statement can be represented by the following equation

$$I_A + I_C = 0 \quad (4-5)$$

where

- $I_A$  — net anodic current generated by metal dissolution reactions [A]
- $I_C$  — net cathodic current generated by the oxygen reduction reaction [A]

The cathodic capacity is equal to the net cathodic current,  $I_C$ . For a given set of electrochemical conditions that would initiate localized corrosion, the net cathodic current can be calculated in both acidic and neutral-to-alkaline solutions because sufficient information exists on the kinetics of oxygen reduction reactions in both types of solutions.

Excess cathodic current is generated in the cathodic region because of a potential gradient in the electrolyte solution. The excess cathodic current is equal to the current generated due to the oxygen reduction reaction minus the current generated by the anodic dissolution reaction in the cathodic region only. The electrode potential is expected to be close to the repassivation potential at the crevice and cathodic region interface, and the electrode potential farther into the cathodic region should approach the value of the corrosion potential. As a result, a gradient in the electrode potential is established in the cathodic region. The current density generated at a given location in the cathodic region is determined by the polarization curve of the oxygen reduction reaction. A schematic of the cathodic region with appropriate boundary conditions and a corresponding oxygen reduction polarization curve is presented in Figure 4-4. As indicated in the polarization curve, the electrode potential is equal to the repassivation potential at the interface of the two regions. The oxygen reduction current density near the repassivation potential is markedly higher than at the corrosion potential. As the electrode potential approaches the corrosion potential, the oxygen reduction reaction current density decreases. Thus, the electrode potential distribution in the cathodic region and the corresponding potential dependence of oxygen reduction kinetics are the sources of excess cathodic current.

In the cathodic region, the current density due to the oxygen reduction reaction is determined by the interplay between the flow of current and the potential drop in the electrolyte, and the activation over potential as a function of the distance from the crevice mouth. The passage of current in the electrolyte leads to the potential drop governed by Ohm's law, which can be expressed by the following equation

$$i = -k \frac{d\phi}{dx} \quad (4-6)$$

where

- $i$  — current density flowing through the electrolyte solution [ $A/cm^2$ ]
- $k$  — conductivity of the electrolyte solution [ $ohm^{-1}cm^{-1}$ ]
- $\phi$  — electrostatic potential of the electrolyte at a given location [V]
- $x$  — position vector [m]

The current flowing along the cathode surface varies with position due to the oxygen reduction reaction. This variation in current as a function of position can be expressed by the following equation

$$\frac{di}{dx} = \left[ \frac{j(x) + i_p}{H} \right] \quad (4-7)$$

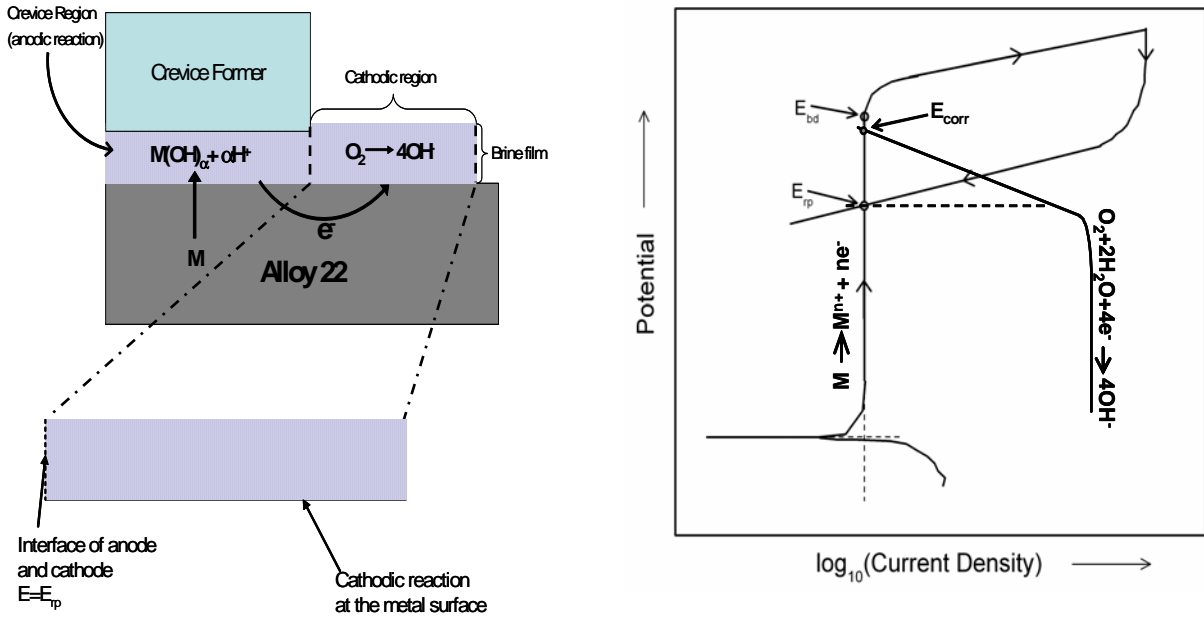


**Figure 4-4. Schematic Representation of the Cathodic Region With Corresponding Cathodic and Anodic Polarization Curves. At the Interface of the Crevice and Cathode, the Potential Is Equal to the Repassivation Potential. The Excess Cathodic Capacity Is Generated in the Cathodic Polarization Curve When the Cathodic Region Electrode Potential Lies Between the Repassivation and Corrosion Potential.**

where

- $j(x)$  — current density [ $A/cm^2$ ] generated by the cathodic reduction reaction current at position  $x$
- $H$  — height of the electrolyte film [m]
- $i_p$  — passive current density [ $A/cm^2$ ]

The combination of Eqs. (4-6) and (4-7) yields

$$\frac{d^2\phi}{dx^2} = -\frac{[j(x) + i_p]}{kH} \quad (4-8)$$

The current density generated due to the cathodic reduction reaction,  $j(x)$ , can be expressed by the following equation

$$j(x) = - \frac{i_{corr} \exp \left[ \frac{-\alpha_c n F}{RT} (V - \phi(x) - E_{corr}) \right]}{1 + \frac{i_{corr}}{i_{lim}} \exp \left[ \frac{-\alpha_c n F}{RT} (V - \phi(x) - E_{corr}) \right]} \quad (4-9)$$

where

$E_{corr}$	—	corrosion potential [V]
$i_{corr}$	—	corrosion current density at the corrosion potential (equal to passive current density, $i_p$ ) [ $A/cm^2$ ]
$\alpha_c$	—	charge transfer coefficient for the cathodic reduction reaction
$n$	—	number of electrons per molecule of oxygen in the cathodic reduction reaction = 4
$F$	—	Faraday constant = 96,486 C/mol
$R$	—	universal gas constant = 8.3145 J/K/mol [1.987 cal/K/mol]
$T$	—	temperature of the system [K]
$V$	—	metal potential [V]
$\phi(x)$	—	solution potential adjacent to the metal surface at position $x$
$i_{lim}$	—	mass-transfer-limited current density [ $A/cm^2$ ]

The cathodic reaction can be under either activation or concentration control. If the cathodic reduction reaction is under concentration control, the current density is equal to the mass-transfer-limited current density; otherwise, the reduction reaction current density under pure activation control is equal to the numerator of Eq. (4-9). For a given thickness of electrolyte film, the mass-transfer-limited current density can be calculated by the following equation:

$$i_{lim} = \frac{n F D C_b}{H} \quad (4-10)$$

where

$C_b$	—	dissolved concentration of oxygen in the bulk electrolyte solution [ $mol/cm^3$ ]
$D$	—	diffusivity of dissolved oxygen in the electrolyte solution [ $cm^2/sec$ ]

At the crevice and cathodic region interface, the electrode potential, which is equal to the potential drop across the metal–solution interface, is assumed to be the repassivation potential. This is a reasonable assumption given that very little or no cathodic current can be generated inside the crevice. A boundary condition for Eq. (4-8) can be represented by the following equation

$$V - \phi(x=0) = E_{rp} \quad (4-11)$$

Under the free corrosion condition, the metal potential, denoted by  $V$ , is equal to zero. At the cathodic region and air interface, the following boundary condition for Eq. (4-8) prevails

$$-\kappa \left. \frac{d\phi}{dx} \right|_{x=L} = 0 \quad (4-12)$$

Equation (4-12) represents the fact that no current can flow across the electrolyte and air interface.

Equation (4-8) is solved subject to the boundary conditions given by Eqs. (4-11) and (4-12). The solution of Eq. (4-8) is obtained in terms of the solution potential,  $\phi$ , as a function of position vector,  $x$ . Then the cathodic reduction current density,  $j(x)$ , is calculated for each value of  $x$  using Eq. (4-9). The net cathodic current is calculated by numerically integrating the cathodic reduction plus passive current density for a given length of the cathodic region according to the following equation

$$I_C = \int_{x=0}^{x=L} [j_p + j(x)] dx \quad (4-13)$$

The net cathodic current calculated using Eq. (4-13) is in units of A/cm. Cathodic capacities are calculated assuming the brine film and the crevice region have a width of 1 cm [0.39 in]. This assumption is based upon a physical representation of the crevice region and brine film surrounding the crevice region where both regions extend infinitely along the width. This is a bounding assumption because a crevice region would be limited by the cylindrical shape of the waste package. As a result, only a fraction of the brine film surrounding the crevice region would generate excess cathodic current. The parameter values used in Eqs. (4-8), (4-9), and (4-10) are described in the following section.

### 4.3.2 Model Parameters

The cathodic capacity model needs the values of corrosion potential ( $E_{corr}$ ), passive current density ( $j_{pass}$ ), corrosion current density ( $i_{corr}$ ), electrolyte conductivity ( $\kappa$ ), dissolved oxygen concentration ( $C_b$ ), diffusivity of oxygen ( $D$ ), film thickness ( $H$ ), film length ( $L$ ), and repassivation potential ( $E_{rp}$ ). It is assumed that the available brine is uniformly spread over the cathodic region located adjacent to the crevice (see Figure 4-3). The value of the cathodic reduction reaction charge transfer coefficient, denoted by  $\alpha_c$  in Eq. (4-9), is set equal to 0.49, and the value of oxygen diffusivity is set equal to  $10^{-5}$  cm<sup>2</sup>/sec [ $1.55 \times 10^{-6}$  in<sup>2</sup>/sec]. These two values are adopted from reported experimental results on oxygen reduction kinetics on Alloy 22 (Bryan, 2005). The values of film length, film thickness, and repassivation potential are varied, and their effects on cathodic capacity are studied in this report.

The deliquescence brine properties needed to calculate the cathodic capacity of Alloy 22 are the brine film thickness and length, the effective ionic conductivity of the brine solution, and the dissolved oxygen concentration. The amount of dust on the metal surface is assumed to be 26 mg/cm<sup>2</sup> [0.37 mlb/in<sup>2</sup>]. DOE considers this amount to be an upper bound value for dust that could deposit on the waste package surface in the potential Yucca Mountain repository (Bechtel SAIC Company, LLC, 2005). The dust particles are assumed to have a specific density of 1 g/cm<sup>3</sup> [36.13 mlb/in<sup>3</sup>] and a spherical diameter equal to either 10 or 30  $\mu$ m [0.39 or 1.18 mil], based on the density and upper-bound estimates of particle size reported by DOE (Bechtel SAIC Company, LLC, 2005). From the specific density of 1 g/cm<sup>3</sup> [36.13 mlb/in<sup>3</sup>], the number of particles per square centimeter of metal surface corresponding to 26 mg [ $5.73 \times 10^{-2}$  mlb] of

dust is calculated to be  $4.97 \times 10^7$  for 10- $\mu\text{m}$  [0.39-mil]-diameter particles or  $1.84 \times 10^6$  for 30- $\mu\text{m}$  [1.18-mil]-diameter particles. Based on geometric considerations and assuming cubic packing of particles, this number of particles in one square centimeter is calculated to occupy 50-particle layers if the particle diameter is 10  $\mu\text{m}$  [0.39 mil] or 17 particle layers if the particle diameter is 30  $\mu\text{m}$  [1.18 mil]. Based on geometric considerations, the interparticle pore space is calculated to be  $2.4 \times 10^{-2} \text{ cm}^3$  [ $1.46 \times 10^{-3} \text{ in}^3$ ] for the 50 particle layers and  $2.38 \times 10^{-2} \text{ cm}^3$  [ $1.45 \times 10^{-3} \text{ in}^3$ ] for the 17 particle layers for 10- $\mu\text{m}$  [0.39-mil] and 30- $\mu\text{m}$  [1.18-mil] diameter particles, respectively, in 1  $\text{cm}^2$  [0.16  $\text{in}^2$ ] of the waste package surface. These results are summarized in Table 4-2.

To calculate the thickness of the brine film resulting from deliquescence, it is assumed that 10 weight percent of the dust that deposits on the metal surface comprises deliquescent salt [ $2.6 \text{ mg/cm}^2$  [ $36.98 \times 10^{-3} \text{ mlb/in}^2$ ]]. The 10 weight percent value is based on the average weight percent reported in the literature (Reheis, 2003) for dust samples taken near Yucca Mountain. The deliquescent salt composition is assumed to be a NaCl–NaNO<sub>3</sub>–KNO<sub>3</sub> mixture. At a temperature of 150 °C [302 °F], this salt mixture would deliquesce when the relative humidity in the environment reaches 17.7 percent and would form a saturated electrolyte solution with a density of 1.29  $\text{g/cm}^3$  [46.6  $\text{mlb/in}^3$ ] according to the data shown in Table 4-3. The deliquescence relative humidity (or deliquescence point) and the brine density data in Table 4-3 are calculated using the chemical thermodynamic simulator (OLI Systems, 2005). The software has been validated for determining the brines properties formed due to deliquescence of salt mixtures with Na–K–Mg–Ca–Cl–NO<sub>3</sub> ions (Gruszkiewicz, et al., 2007). At the deliquescence point of the NaCl–NaNO<sub>3</sub>–KNO<sub>3</sub> salt mixture, the electrolyte solution is calculated to have a composition of 69.6, 4.07, and 61.6 molal of KNO<sub>3</sub>, NaCl, and NaNO<sub>3</sub>, respectively. The nitrate-to-chloride ratio for this brine is approximately equal to 32. This work assumes that localized corrosion initiates in this brine.

The amount of brine that forms is limited by the amount of deliquescent salt. Given that only  $2.6 \text{ mg/cm}^2$  [ $36.98 \times 10^{-3} \text{ mlb/in}^2$ ] of salts are present on the metal surface, the calculated mass of water that forms upon deliquescence is  $2.08 \times 10^{-4} \text{ g/cm}^2$  [ $2.96 \times 10^{-3} \text{ mlb/in}^2$ ]. The brine

**Table 4-2. Dust Particle Size, Dust Layer Thickness, Brine Film Thickness, Ionic Conductivity, and Effective Ionic Conductivity of Dust Deliquescence Brine Formed by NaCl–NaNO<sub>3</sub>–NaNO<sub>3</sub>–KNO<sub>3</sub> Salt Assemblage at 150 °C [302 °F]**

Particle Size ( $\mu\text{m}$ ) [mil]	Dust Layer Thickness ( $\mu\text{m}$ ) [mil]	Brine Film Thickness ( $\mu\text{m}$ ) [mil]	Ionic Conductivity of NaCl–KNO <sub>3</sub> –NaNO <sub>3</sub> Brine ( $\text{ohm}^{-1}\text{cm}^{-1}$ ) [ $\text{ohm}^{-1} \text{in}^{-1}$ ]	Effective* Ionic Conductivity of NaCl–KNO <sub>3</sub> –NaNO <sub>3</sub> Brine ( $\text{ohm}^{-1}\text{cm}^{-1}$ ) [ $\text{ohm}^{-1} \text{in}^{-1}$ ]
10 [0.39]	500 [19.7] (50 particle layers)	45.4 [1.79]	0.0382 [0.0970]	0.01834 [0.04658]
30 [1.18]	510 [20.1] (17 particle layers)	45.6 [1.80]	0.0382 [0.0970]	0.01826 [0.04638]

\*Calculated using Bruggeman's equation (Eq. 4-14). Temperature = 150 °C [302 °F]; Deliquescence Relative Humidity = 17.7 percent. Brine composition: 69.6 molal KNO<sub>3</sub>, 4.1 molal NaCl, and 61.6 molal NaNO<sub>3</sub>

**Table 4-3. Calculated Deliquescence Relative Humidity, Dissolved Oxygen Concentration, and Ionic Conductivity of Deliquescence Salts at Various Temperatures**

Temperature (°C) [°F]	Salts Present	Deliquescence Relative Humidity (Percent)*	Dissolved Oxygen Concentration (Parts Per Million)	Ionic Conductivity (ohm <sup>-1</sup> cm <sup>-1</sup> ) [ohm <sup>-1</sup> in <sup>-1</sup> ]
120 [248]	NaCl–NaNO <sub>3</sub> –KNO <sub>3</sub>	26.7	0.121	0.035 [0.089]
130 [266]	NaCl–NaNO <sub>3</sub> –KNO <sub>3</sub>	22.2	0.092	0.033 [0.084]
140 [284]	NaCl–NaNO <sub>3</sub> –NaNO <sub>3</sub> ·KNO <sub>3</sub>	18.2	0.068	0.032 [0.081]
150 [302]	NaCl–NaNO <sub>3</sub> –NaNO <sub>3</sub> ·KNO <sub>3</sub>	17.7	0.065	0.038 [0.097]
160 [320]	NaCl–NaNO <sub>3</sub> –NaNO <sub>3</sub> ·KNO <sub>3</sub>	16.5	0.057	0.042 [0.107]
170 [338]	NaCl–NaNO <sub>3</sub> –NaNO <sub>3</sub> ·KNO <sub>3</sub>	14.6	0.044	0.042 [0.107]

\*Some values reported here are slightly different from Table 2-13 due to slight differences in the input parameters for the different calculations.

volume corresponding to this mass of water is  $2.18 \times 10^{-3} \text{ cm}^3$  [ $1.33 \times 10^{-4} \text{ in}^3$ ], based on a brine density of  $1.29 \text{ g/cm}^3$  [46.6 mlb/in<sup>3</sup>].

The brine would occupy the interparticle pore spaces and would have a film thickness equivalent to 4.54 layers of 10- $\mu\text{m}$  [0.39-mil]-diameter particles or 1.52 layers of 30- $\mu\text{m}$  [1.18-mil]-diameter particles.

A schematic representation of the spreading of the brine film layer with dust particles is represented in Figure 4-5, showing that the thickness of brine film is less than that of the dust layer. This work assumes that the capillary effect of the dust particles on brine film is negligible.

The calculated ionic conductivity of the deliquescence brine at 150 °C [302 °F] using the software (OLI Systems, 2005) is  $0.0382 \text{ ohm}^{-1}\text{cm}^{-1}$  [ $0.0971 \text{ ohm}^{-1}\text{in}^{-1}$ ]. However, the effective ionic conductivity of the electrolyte is decreased by the presence of the dust particles. The effective ionic conductivity can be calculated using Bruggeman's equation (Bruggeman, 1935)

$$k_{\text{eff}} = k(\theta)^{1.5} \quad (4-14)$$

where

$$\theta = \frac{V_{\text{solution}}}{V_{\text{solution}} + V_{\text{particle}}} \quad (4-15)$$

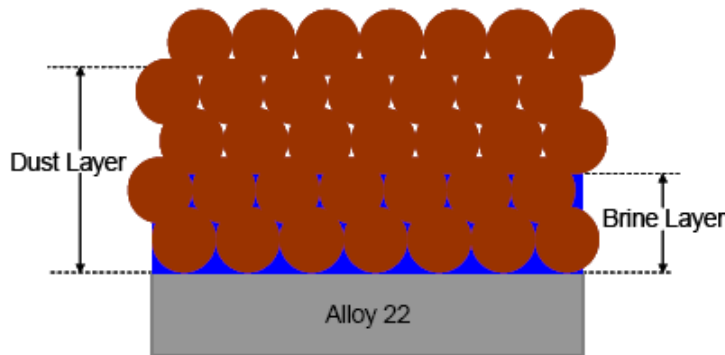


**Figure 4-5. Schematic Representation of Dust Deliquescence Brine Layer and Dust Layer on Alloy 22 Surface**

where

- $V_{\text{solution}}$  — volume occupied by the solution [ $\text{cm}^3$ ]
- $V_{\text{particle}}$  — volume occupied by the particles [ $\text{cm}^3$ ]
- $K$  — ionic conductivity of the pure electrolyte solution [ $\text{ohm}^{-1}\text{cm}^{-1}$ ]
- $k_{\text{eff}}$  — effective ionic conductivity of the electrolyte solution in the presence of particles [ $\text{ohm}^{-1}\text{cm}^{-1}$ ]

For the brine with a film thickness equivalent to 4.54 particle layers, the value of  $\Theta$  is calculated to be 0.480 and the effective ionic conductivity is equal to  $0.01834 \text{ ohm}^{-1}\text{cm}^{-1}$  [ $0.04658 \text{ ohm}^{-1}\text{in}^{-1}$ ]. For the brine with a film thickness of 1.52 particle layers,  $\Theta$  is calculated to be 0.478 and the effective ionic conductivity is equal to  $0.01826 \text{ ohm}^{-1}\text{cm}^{-1}$  [ $0.04638 \text{ ohm}^{-1}\text{in}^{-1}$ ]. Because the relative difference between the two calculated values for both particle sizes is less than 1 percent, the effective ionic conductivity of  $0.01834 \text{ ohm}^{-1}\text{cm}^{-1}$  [ $0.04658 \text{ ohm}^{-1}\text{in}^{-1}$ ] is used in cathodic capacity simulations for dust deliquescence brines at  $150 \text{ }^\circ\text{C}$  [ $302 \text{ }^\circ\text{F}$ ].

The ionic conductivity and effective ionic conductivity of dust deliquescence brines for both particle sizes are also summarized in Table 4-2. The effective ionic conductivity of dust deliquescence brines between  $120$  and  $170 \text{ }^\circ\text{C}$  [ $248$  and  $338 \text{ }^\circ\text{F}$ ] is obtained by using the value of  $\Theta$  equal to 0.480. The calculated values are listed in Table 4-4.

<b>Table 4-4. Effective Ionic Conductivity of Dust Deliquescence Brine Formed Between 120 and 170 °C [248 and 338 °F]</b>	
<b>Temperature (°C) [°F]</b>	<b>Effective Ionic Conductivity (ohm<sup>-1</sup>cm<sup>-1</sup>) [ohm<sup>-1</sup> in<sup>-1</sup>]</b>
120 [248]	0.0168 [0.0427]
130 [266]	0.0158 [0.0402]
140 [284]	0.0154 [0.0390]
160 [320]	0.0202 [0.0512]
170 [338]	0.0202 [0.0512]

The dissolved oxygen concentration in the deliquescence brines at various temperatures is calculated using the model presented in Tromans (2000, 1998). This author gives equations for calculating the effect of electrolytes, including NaCl and NaNO<sub>3</sub>, on the dissolved oxygen concentration. However, Tromans (2000, 1998) did not provide any parameters for KNO<sub>3</sub> solutions. Therefore, this study assumes KNO<sub>3</sub> has the same effect on oxygen solubility as NaNO<sub>3</sub>, and the dissolved oxygen concentration in NaCl–NaNO<sub>3</sub>–KNO<sub>3</sub> solutions is calculated using NaCl and NaNO<sub>3</sub> parameters only. The dissolved oxygen concentration for various salt assemblages is summarized in Table 4-3. Note that the dissolved oxygen concentration does not change much for different salt assemblages between 140 and 160 °C [284 and 320 °F]. For this reason, the dust deliquescence brine temperature is set to 150 °C [302 °F] for calculating cathodic capacity of Alloy 22 at the intermediate temperature. Cathodic capacity calculations are also carried in the temperature range of 120–170 °C [248–338 °F] to elucidate the effect of temperature.

The corrosion potential of Alloy 22 in dust deliquescence brines is selected to be 0.6 V<sub>SHE</sub>, where SHE stands for the standard hydrogen reference electrode. This value is based on the experimental studies conducted by Yang (2006) in which the corrosion potential of Alloy 22 in dust deliquescence brine was found to be in the range of 0.4 to 0.65 V<sub>SHE</sub>. The corrosion potential of Alloy 22 in dust deliquescence brines is assumed to be independent of the temperature.

At the corrosion potential, the corrosion and passive current density are calculated using the following equation

$$i_{corr} = i_{pass} = i_a^0 \exp \left[ -\frac{E}{R} \left( \frac{1}{T} - \frac{1}{T_{ref}} \right) \right] \quad (4-16)$$

where

- $T$  — temperature of the system [K]
- $i_a^0$  — passive current density (A/cm<sup>2</sup>) at temperature  $T_{ref}$  [K] = 10<sup>-8</sup> A/cm<sup>2</sup> [6.45 × 10<sup>-8</sup> A/in<sup>2</sup>]
- $E$  — activation energy [J/mol] for the passive current density = 44,700 J/mol [10,676 cal/mol]
- $R$  — universal gas constant = 8.3145 J/K/mol [1.987 cal/K/mol]
- $T_{ref}$  — reference temperature [K] for the passive current density = 368.15 K [203 °F]

Equation (4-16) is used to calculate the passive current at 150 °C [302 °F] for dust deliquescence brines. Dunn, et al. (2005) originally proposed this equation, derived from their own experimental data, for calculating the passive current density and the corresponding general corrosion rate in seepage water brines at temperatures lower than 100 °C [212 °F]. Note that the corrosion rate estimated using Eq. (4-16) is also within the range of corrosion rates in dust deliquescence brines that Yang (2006) experimentally observed.

### 4.3.3 Calculated Cathodic Capacities

The distribution of the potential drop across the metal–solution interface (i.e., electrode potential) as a function of distance from the crevice region is presented in Figure 4-6(a). Four

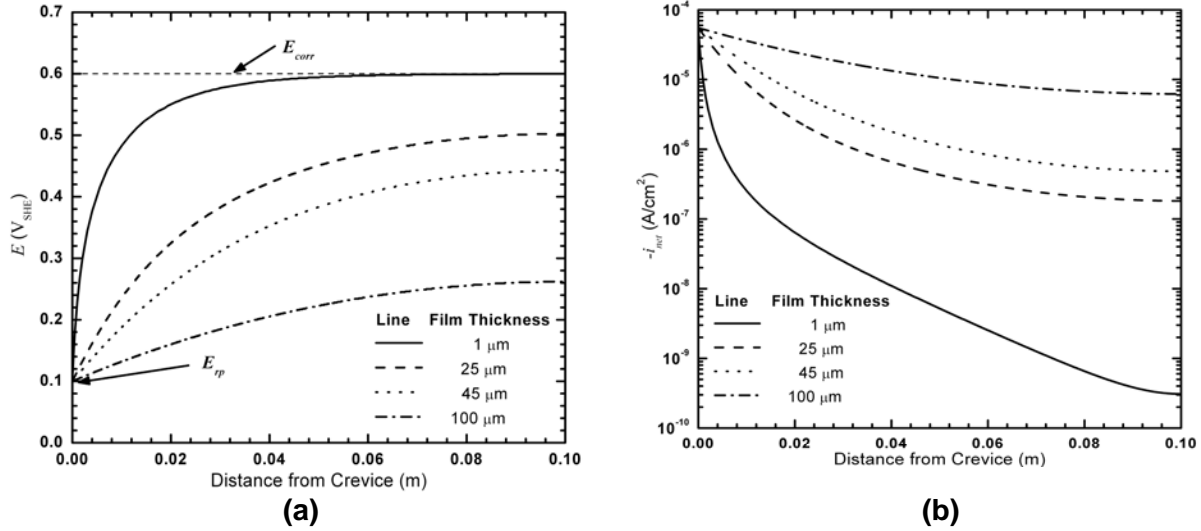


**Figure 4-6. (a) Electrode Potential and (b) Current Density Distribution of Alloy 22 in the Cathodic Region. These Distributions Are Represented as a Function of Distance From the Crevice Region. The Electrolyte Brine Film Is Assumed To Be 0.1 m [3.94 in] Long and the Repassivation Potential Is Fixed at 0.1  $V_{SHE}$ .**

electrode potential distributions are presented corresponding to four film thicknesses: 1, 25, 45, and 100  $\mu\text{m}$  [ $3.94 \times 10^{-2}$ , 0.98, 1.8, and 3.94 mil]. These four simulations are performed using a repassivation potential equal to 0.1  $V_{SHE}$  at 150 °C [302 °F]. As seen in Figure 4-6(a), the electrode potential increases more sharply for a 1- $\mu\text{m}$  [ $3.94 \times 10^{-2}$ -mil]-thick film compared to the thicker films, and attains a value equal to the corrosion potential at a distance approximately 0.06 m [2.36 in] from the crevice region. This result is consistent with the formulation of solution potential distribution represented by Eq. (4-8). An analysis of Eq. (4-8) indicates that solution potential is inversely proportional to the product of electrolyte ionic conductivity and film thickness. Therefore, the solution potential along the metal surface would decrease sharply for thin films. The corresponding current density distributions for four film thicknesses are presented in Figure 4-6(b). The area under the current density distribution curves is equal to the cathodic capacity of the film. As seen in Figure 4-6(b), the area under the 1- $\mu\text{m}$  [ $3.94 \times 10^{-2}$ -mil]-thick film is smaller compared to the 25- $\mu\text{m}$  [0.98-mil]-thick film. The area under the current density distribution curve increases with increasing thickness, which indicates the cathodic capacity also increases with film thickness for a given film length.

The cathodic capacities for various values of repassivation potential and film thickness are presented in Figure 4-7 where each data point represents cathodic capacity for one electrode potential and corresponding current density distribution. The corrosion potential and brine film length are set equal to 0.6  $V_{SHE}$  and 0.1 m [3.94 in], respectively, at 150 °C [302 °F]. The cathodic capacity is presented as a function of the difference between corrosion and repassivation potential (i.e.,  $E_{corr} - E_{rp}$ ). As seen in Figure 4-7, the cathodic capacity increases with increasing values of  $E_{corr} - E_{rp}$ . On other hand, the cathodic capacity increases with film thickness for a fixed value of  $E_{corr} - E_{rp}$ . However, for 1- $\mu\text{m}$  [ $3.94 \times 10^{-2}$ -mil]-thick film, the electrode potential distribution presented in Figure 4-6(a) indicates that cathodic capacity reaches an asymptotic value at a fixed value of  $E_{corr} - E_{rp}$  (i.e., additional increases in film length will not result in further increases in cathodic capacity). This occurs because the electrode potential attains an asymptotic value of corrosion potential close to the crevice region even for

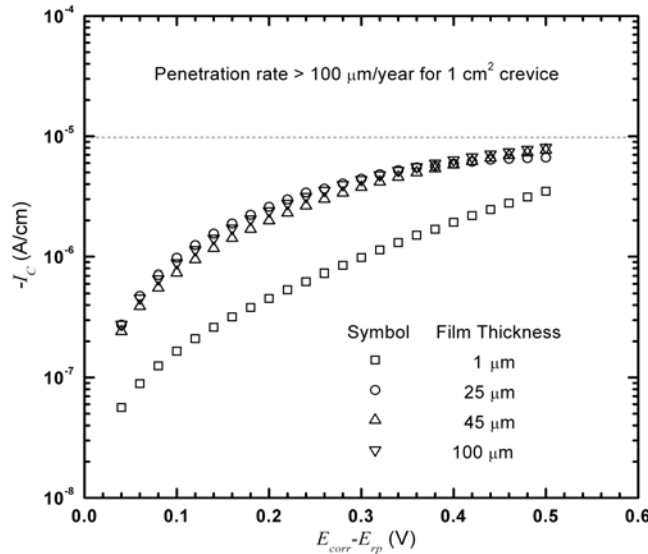


**Figure 4-7. Cathodic Capacity of Alloy 22 in Dust Deliquescence Brine as a Function of the Difference Between the Corrosion Potential and the Repassivation Potential ( $E_{corr}-E_{rp}$ ) for Various Film Thicknesses. The Corrosion Potential and Brine Film Length Are Fixed at  $0.6 V_{SHE}$  and  $0.1\text{ m}$  [ $3.94\text{ in}$ ], Respectively. A Penetration Rate of  $100\text{ }\mu\text{m/yr}$  [ $3.94\text{ mil/yr}$ ] or Higher Is Expected for  $1\text{ cm}^2$  [ $0.16\text{ in}^2$ ] of Active Crevice Region When the Cathodic Capacity Is Above the Horizontal Dashed Line.**

large values of  $E_{corr}-E_{rp}$ . However, for thicker films and for a given value of  $E_{corr}-E_{rp}$ , a marginal increase in cathodic capacity may result because of an increase in film length.

To explore the effect of brine film length on cathodic capacity, additional simulations were performed at a fixed film thickness but variable film length. The simulation results are presented in Figure 4-8, where cathodic capacity is plotted as a function of  $E_{corr}-E_{rp}$ . The brine film thickness and corrosion potential are set equal to  $45\text{ }\mu\text{m}$  [ $1.8\text{ mil}$ ] and  $0.6 V_{SHE}$ , respectively, at  $150\text{ }^\circ\text{C}$  [ $302\text{ }^\circ\text{F}$ ]. As seen in Figure 4-8, there is a marginal variation in cathodic capacity with increasing film length. This result is consistent with the observation that the electrode potential changes sharply near the crevice region. As a result, most of the excess cathodic current density is generated in the cathodic region adjacent to the crevice. For this reason, a film length increase has only a marginal effect on cathodic capacity of Alloy 22 in dust deliquescence brines. In Figures 4-7 and 4-8, a horizontal dashed line is added to emphasize the consequence of cathodic capacity values above the dash line. Cathodic capacity greater than  $9.8 \times 10^{-6}\text{ A/cm}$  [ $2.49 \times 10^{-5}\text{ A/in}$ ] at a given  $E_{corr}-E_{rp}$  will result in a penetration rate of  $100\text{ }\mu\text{m/yr}$  [ $3.94\text{ mil/year}$ ] or higher for an active crevice area of  $1\text{ cm}^2$  [ $0.16\text{ in}^2$ ]. As seen in Figures 4-7 and 4-8, the cathodic capacity is below the horizontal dashed line even if  $E_{corr}-E_{rp}$  approaches a value of  $0.5\text{ V}$ .

Additional simulations were performed for a  $45\text{-}\mu\text{m}$  [ $1.8\text{-mil}$ ]-thick and  $0.1\text{-m}$  [ $3.94\text{-in}$ ]-long brine film to assess the effect of oxygen solubility and brine temperature. The corrosion potential is set equal to  $0.6 V_{SHE}$ , and the temperature of the brine is varied between  $120$  and  $170\text{ }^\circ\text{C}$  [ $248$  and  $338\text{ }^\circ\text{F}$ ]. For a selected brine temperature, the dissolved oxygen concentration of the brine was specified using the values listed in Table 4-3. The corresponding effective ionic

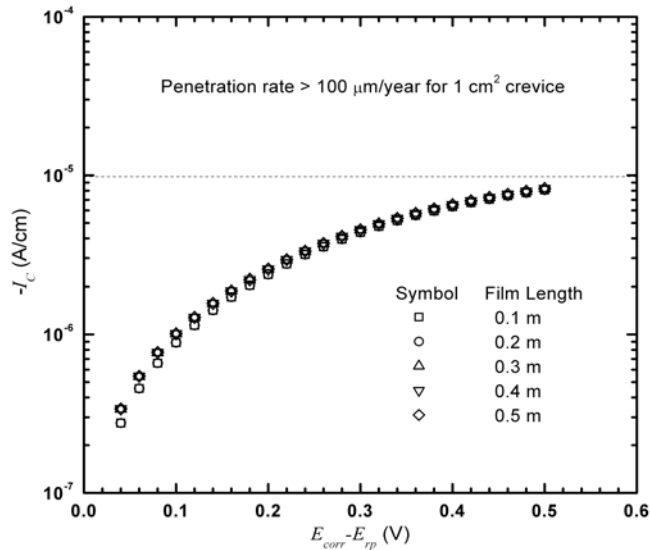


**Figure 4-8. Cathodic Capacity of Alloy 22 in Dust Deliquescence Brines as a Function of the Difference Between the Corrosion Potential and the Repassivation Potential ( $E_{corr}-E_{rp}$ ) for Various Brine Film Lengths. The Corrosion Potential and Brine Film Thickness Are Set Equal to  $0.6 V_{SHE}$  and  $45 \mu\text{m}$  [1.8 mil], Respectively. A Penetration Rate of  $100 \mu\text{m/yr}$  [3.94 mil/yr] or Higher Is Expected for  $1 \text{ cm}^2$  [0.16 in<sup>2</sup>] of Active Crevice Region When the Cathodic Capacity Is Above the Horizontal Dashed Line.**

conductivity of brine is also varied according to the values listed in Table 4-4. The simulation results are presented in Figure 4-9, where cathodic capacity is plotted as a function of  $E_{corr}-E_{rp}$ . As seen in the figure, the cathodic capacity for the brine at  $120 \text{ }^\circ\text{C}$  [248  $^\circ\text{F}$ ] is above the horizontal dashed line when  $E_{corr}-E_{rp}$  is greater than 0.36 V. This result can be attributed to the higher oxygen solubility in the brine at  $120 \text{ }^\circ\text{C}$  [248  $^\circ\text{F}$ ]. For temperatures greater than or equal to  $130 \text{ }^\circ\text{C}$  [266  $^\circ\text{F}$ ], cathodic capacity varies significantly when  $E_{corr}-E_{rp}$  is less than 0.2 V. However, as  $E_{corr}-E_{rp}$  approaches the value of 0.5 V, the cathodic capacity values become closer at different temperatures with the exception of  $120 \text{ }^\circ\text{C}$  [248  $^\circ\text{F}$ ].

#### 4.3.4 Discussion on Cathodic Capacity Results

The cathodic capacity of Alloy 22 in dust deliquescence brines is determined primarily by the film thickness and by the difference between corrosion and repassivation potentials (i.e.,  $E_{corr}-E_{rp}$ ). As seen in Figure 4-6(a), the potential at the metal–solution interface approaches the corrosion potential with increasing distance from the crevice, and the gradient of the potential is fairly steep at the interface. As a result, most of the excess cathodic current is generated where the electrode potential is sufficiently cathodic with respect to the corrosion potential. Even though excess cathodic current also is generated farther into the cathodic region, the magnitude of the excess current is too small to influence significantly the cathodic capacity. Therefore, a sufficiently long brine film {0.1 m [3.94 in]} is needed adjacent to the crevice mouth for generating the excess cathodic current, and a film extending farther than 0.1 m [3.94 in] into the cathodic region does not have much influence on the cathodic capacity. This observation is confirmed by the results presented in Figure 4-8, where cathodic capacity is plotted as a function of  $E_{corr}-E_{rp}$  for various film lengths at a film thickness equal to  $45 \mu\text{m}$  [1.8 mil] at  $150 \text{ }^\circ\text{C}$  [302  $^\circ\text{F}$ ]. The calculated cathodic capacity changes only marginally with increasing film length for a given value of  $E_{corr}-E_{rp}$ . Therefore, the cathodic capacity of Alloy 22

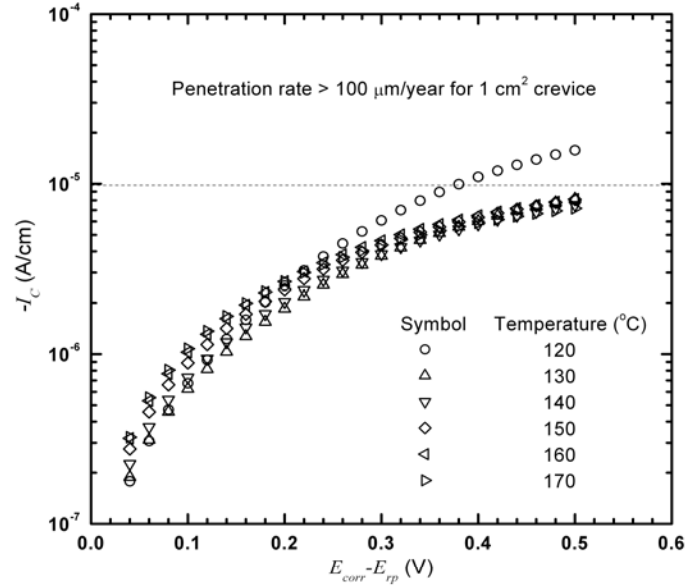


**Figure 4-9. Cathodic Capacity of Alloy 22 in Dust Deliquescence Brines as a Function of the Difference Between the Corrosion Potential and the Repassivation Potential ( $E_{corr}-E_{rp}$ ) for 45- $\mu\text{m}$  [1.8-mil]-Thick and 0.1-m [3.94-in]-Long Brine Film at Different Temperatures. The Corrosion Potential Is Set Equal to 0.6  $V_{SHE}$ . A Penetration Rate of 100  $\mu\text{m}/\text{yr}$  [3.94 mil/yr] or Higher Is Expected for 1  $\text{cm}^2$  [0.16  $\text{in}^2$ ] of Active Crevice Region When the Cathodic Capacity Is Above the Horizontal Dashed Line.**

in dust deliquescence brines is primarily dependent on  $E_{corr}-E_{rp}$  and film thickness as long as the film length is 0.1 m [3.94 in] or more.

The effect of cathodic capacity on the crevice corrosion process can be understood by calculating the penetration rate for a given crevice site. A cathodic capacity of  $9.8 \times 10^{-6}$  A/cm [ $2.49 \times 10^{-5}$  A/in] can sustain metal dissolution at the rate of 100  $\mu\text{m}/\text{yr}$  [3.94 mil/yr] for 1  $\text{cm}^2$  [0.16  $\text{in}^2$ ] of active crevice area. Such cathodic capacity in dust deliquescence brines is attained at 120 °C [248 °F] when  $E_{corr}-E_{rp}$  is approximately equal to 0.36 V for a 45- $\mu\text{m}$  [1.8-mil]-thick film (see Figure 4-9). For all other conditions, the cathodic capacity stays below  $9.8 \times 10^{-6}$  A/cm [ $2.49 \times 10^{-5}$  A/in].

An analysis similar to the one presented in the preceding paragraph can be carried out for evaluating the effect of cathodic capacity when the active crevice area is 0.1  $\text{cm}^2$  [0.16  $\text{in}^2$ ] or less. In this case, a lower value of cathodic capacity may be sufficient to sustain a high penetration rate. For example, a cathodic capacity of  $9.8 \times 10^{-7}$  A/cm [ $2.49 \times 10^{-6}$  A/in] in dust deliquescence brines at  $E_{corr}-E_{rp}$  equal to 0.12 V for a film that is 45  $\mu\text{m}$  [1.8 mil] thick at 150 °C [248 °F] film can sustain a penetration rate of 100  $\mu\text{m}/\text{yr}$  [3.94 mil/yr] in a 0.1  $\text{cm}^2$  [0.016  $\text{in}^2$ ] crevice area. However, a smaller crevice site will have less significance on the release of radionuclides compared to a larger site.

In summary, the results of the cathodic capacity model for dust deliquescence brines indicate that localized corrosion with a penetration rate of 100  $\mu\text{m}/\text{year}$  [3.94 mil/year] for 1  $\text{cm}^2$  [0.16  $\text{in}^2$ ] of crevice can be achieved when  $E_{corr}-E_{rp}$  is greater than a critical value.

## 4.4 Summary

The experimental data on corrosion and repassivation potentials reported by Felker, et al.(2006) and Rebak (2006) indicate that the localized corrosion of Alloy 22 is not likely in large quantities of dust deliquescence-type brines that have nitrate-to-chloride ratios higher than 5, unless the brine pH is close to 2 at temperatures up to 150 °C [302 °F]. However, the localized corrosion is likely in brines having nitrate-to-chloride ratios at or below 0.2.

According to the analysis in Chapter 2, the dust deliquescence brines that are likely to form at temperatures above 120 °C [248 °F] would have nitrate-to-chloride ratios higher than 5. Staff concludes that localized corrosion is not likely to occur under the potential repository conditions at temperatures between 120 and 150 °C [248 and 302 °F], based on the repassivation and corrosion potential data reported by Felker, et al.(2006) and Rebak (2006). However, for dust deliquescence brines that are likely to form between 100 and 120 °C [212 and 248 °F], the nitrate-to-chloride ratio may be low (less than 0.1) enough to initiate the localized corrosion. These dust deliquescence brines may contain other localized corrosion inhibiting species such as sulfate, bicarbonate, and carbonate. As a result, the total inhibitor (nitrate + sulfate + bicarbonate + carbonate) -to-chloride ratio may still be high enough to inhibit the localized corrosion of Alloy 22 in dust deliquescence brines formed between 100 and 120 °C [212 and 248 °F]. Staff considers additional experimental data to be required in order to assess the susceptibility of Alloy 22 to localized corrosion in large quantities of dust deliquescence brine systems containing low nitrate but high concentrations of the other anions such as sulfate, bicarbonate, and carbonate.

Immersion test data reported by Dixit, et al. (2006) and Lee and Solomon (2006) indicated that localized corrosion of Alloy 22 initiated in large quantities of nitrate-rich solutions at temperature equal to or greater than 140 °C [284 °F]. Localized crevice corrosion was also observed for specimens exposed to the vapor phase of the test vessel. These observations appear to contradict the repassivation and corrosion potential data reported by Felker, et al.(2006) and Rebak (2006), which indicated that localized corrosion is unlikely in nitrate-rich brine solutions. Additional long-term immersion tests data are required to resolve the discrepancy if the repassivation potential data is applied to evaluate the localized corrosion of Alloy 22 in large quantities of dust deliquescence brine solutions.

The cathodic capacity results indicate that a sufficient positive value of  $E_{corr} - E_{rp}$  is needed to achieve sufficiently high crevice corrosion penetration rates. Based upon the experimentally measured values of  $E_{corr}$  and  $E_{rp}$ , it can be deduced that  $E_{corr} - E_{rp}$  should be at least equal to 0.2 V and the maximum cathodic capacity on the order of  $10^{-6}$  A/cm [ $2.54 \times 10^{-6}$  A/in]. A high crevice penetration rate over a large surface area of the crevice region cannot be achieved with a cathodic capacity of  $10^{-6}$  A/cm [ $2.54 \times 10^{-6}$  A/in], even though a high penetration rate can be achieved over a smaller crevice region. Nevertheless, a smaller crevice site will have less significance on radionuclide release compared to a larger hole created by crevice corrosion.

## 4.5 References

Bard, A.J. and L.R. Faulkner. *Electrochemical Methods, Fundamentals and Applications*. New York City, New York: John Wiley & Sons. 1980.

Bechtel SAIC Company, LLC. "Analysis of Dust Deliquescence for FEP Screening." ANL-EBS-MD-000074. Rev. 0. Las Vegas, Nevada: Bechtel SAIC Company, LLC. 2005.

Bruggeman, D.A.G. "Berechnung Verschiedener Physikalischer Konstanten von Heterogenen Substanzen. I. Dielectrizitätskonstanten und Leitfähigkeiten der Mischkörper aus isotropen Substanzen." *Annalen der Physik*. Vol. 24. pp. 636–679. 1935.

Bryan, C.R. "Localized Corrosion Due to Dust Deliquescence on the Alloy 22 Waste Package Outer Barrier." Nuclear Waste Technical Review Board Meeting, November 8–9, 2005, Las Vegas, Nevada. 2005. <<http://www.nwtrb.gov/meetings/2005/nov/bryan.pdf>> (7 April 2008).

Cui, F., F. Presuel-Moreno, and R. Kelly. "Computational Modeling of Cathodic Limitation On Localized Corrosion of Wetted SS 316 at Room Temperature." *Corrosion Science*. Vol. 47. pp. 2,987–3,005. 2005.

Dixit, S., S. Roberts, K. Evans, T. Wolery, and S. Carroll. "General Corrosion and Passive Film Stability." UCRL–TR–217393. Livermore, California: Lawrence Livermore National Laboratory. 2006.

Dunn, D.S., O. Pensado, Y.-M. Pan, R.T. Pabalan, L. Yang, X. He, and K.T. Chiang. "Passive and Localized Corrosion of Alloy 22 Modeling and Experiments." CNWRA 2005-02. Rev. 1. San Antonio, Texas: CNWRA. 2005.

Dunn, D.S., L. Yang, Y.-M. Pan, and G.A. Cragnolino. "Localized Corrosion Susceptibility of Alloy 22." CORROSION/2003 Conference. Paper 03697. Houston, Texas: NACE. 2003.

Dunn, D.S., G.A. Cragnolino, and N. Sridhar. "An Electrochemical Approach to Predicting Long-Term Localized Corrosion of Corrosion-Resistant High-Level Waste Container Materials." *Corrosion*. Vol. 56. pp. 90–104. 2000.

Felker, S., P.D. Hailey, T. Lian, K.J. Staggs, and G. Gdowski. "Alloy 22 Localized Corrosion Susceptibility in Aqueous Solutions of Chloride and Nitrate Salts of Sodium and Potassium at 110–150°C." UCRL–TR–218195. Livermore, California: Lawrence Livermore National Laboratory. 2006.

Gruszkiewicz, M.S., D.A. Palmer, R.D. Springer, P. Wang, and A. Anderko. "Phase Behavior of Aqueous Na-K–Mg–Ca–Cl–NO<sub>3</sub> Mixtures: Isopiestic Measurements and Thermodynamic Modeling." *Journal of Solution Chemistry*. Vol. 36. pp. 723–765. 2007.

Hua, F., J. Sarver, J. Jevic, and G. Gordon. "Corrosion Behavior of Alloy 22 and Ti Grade 7 in a Nuclear Waste Repository Environment." *Corrosion*. Vol. 60, No 8. pp. 764–777. 2004.

Kelly, R.G., A. Agarwal, F. Cui, X. Shan, U. Landau, and J. Payer. "Considerations of the Role of the Cathodic Regions in Localized Corrosion." 11<sup>th</sup> International High-Level Radioactive Waste Management Conference, Las Vegas, Nevada, April 30–May 4, 2006.

Kolts, J. and N. Sridhar. "Temperature Effects in Localized Corrosion in Corrosion of Nickel-Based Alloys." Conference Proceedings of the International Conferences of Nickel-Base Alloys. Cincinnati, Ohio, October 23–25, 1984. pp. 191–198. 1984.

Lee, S.G. and A.A. Solomon. "Localized Corrosion of Alloy C22 Nuclear Waste Canister Material Under Limiting Conditions." *Materials Science and Engineering*. Vol. A 434. pp.114–123. 2006.

OLI Systems, Inc. "A Guide to Using the OLI Software for Version 2.0 of the Analyzers." Morris Plains, New Jersey: OLI Systems, Inc. 2005.

Rebak, R. "Newer Alloy 22 Data and Their Relevance to High-Temperature Localized Corrosion." 2006. Nuclear Waste Technical Review Board Meeting. September 25–26, 2006. <<http://www.nwtrb.gov/meetings/2006/sept/rebak.pdf>>. (7 April 2008).

Reheis, M.C. "Dust Deposition in Nevada, California, and Utah, 1984–2002." U.S. Geological Survey Open-File Report 03-138. 2003.

Shukla, P. "Thermodynamics of Corrosion and Potentiometric Methods for Measuring Localized Corrosion." *Corrosion Monitoring Techniques*. Chapter 7. L. Yang, ed. Success, United Kingdom: Woodhead Publishing. 2008.

Tromans, D. "Modeling Oxygen Solubility in Water and Electrolyte Solutions." *Industrial & Engineering Chemistry Research*. Vol. 39. pp. 805–812. 2000.

———. "Temperature and Pressure Dependent Solubility of Oxygen in Water: A Thermodynamic Analysis." *Hydrometallurgy*. Vol. 48. pp. 327–342. 1998.

Yang, L. "Corrosion of Alloy 22 in Concentrated Nitrate and Chloride Salt Environments at Elevated Temperatures—Progressive Report." CNWRA 2006-02. San Antonio, Texas: CNWRA. 2006.

## 5 SUMMARY AND CONCLUSIONS

### 5.1 Formation of Deliquescence Brines at Elevated Temperatures and Low Relative Humidities

Information on the geochemistry of dust samples taken from Yucca Mountain and vicinity was reviewed. Dusts contain relatively small fractions of soluble salts, ranging from 10 percent at the maximum in remote locations to less than 0.1 percent in Yucca Mountain surface dusts. Leachates typically contain sodium, potassium, and calcium as major cations, and chloride, nitrate, and sulfate as major anions. Nitrate-to-chloride molar ratios exceeded 0.1 for all samples. Feldspars, quartz, and calcite were among the minerals typically found in Yucca Mountain dusts.

The possible assemblage of deliquescent salts present in Yucca Mountain dusts was determined by simulating the evaporation of aqueous solutions derived from leaching dust samples from Yucca Mountain. The results of the thermodynamic simulations indicated that the most likely salt assemblages comprise NaCl–NaNO<sub>3</sub>–KNO<sub>3</sub> and NaCl–KNO<sub>3</sub> mixtures, with a relatively uncommon occurrence of assemblages containing calcium nitrate salts. Thermodynamic calculations also were conducted to determine the mutual deliquescence relative humidities of the salt assemblages and the chemistry of the brines that could form by deliquescence. The results indicate that the mutual deliquescence relative humidities of the salt assemblages are low, particularly at temperatures above 100 °C [212 °F]; if these salts are present in the potential repository, brines are likely to form by salt deliquescence even when the waste packages are relatively hot. However, the brines that are likely to form at temperatures above 120 °C [248 °F] would have molar ratios of nitrate to chloride higher than 5. At temperatures between 100 and 120 °C [212 and 248 °F], the nitrate-to-chloride molar ratio may be low (less than 0.1), but the ratio of the total amount of nitrate, sulfate, bicarbonate, and carbonate to chloride would still be higher than 3.3 for the KCl–KNO<sub>3</sub> salt assemblage.

Experiments were conducted to evaluate the effect of capillary retention by insoluble dusts on the corrosivity of deliquescence brines. The experiments were conducted at 70 °C [158 °F] in a temperature- and humidity-controlled chamber using solid mixtures with varying ratios of NaCl to quartz or rock dust particles placed on top of carbon steel coupled multielectrode array probes. The results indicate that even at a dust-to-NaCl weight ratio of 249, corrosion of carbon steel was observed, indicating that there was a significant amount of brine available on the metal surface. In addition, no significant effect of dust particle size on capillary retention was observed, except for the largest dust particles {>149 μm [>5.87 mil]} used in the test.

Additional experiments were carried out to assess the corrosion of Alloy 22 in brines formed by deliquescence of salts (NaCl–KNO<sub>3</sub>–NaNO<sub>3</sub>) mixed with rock dust. Tests were conducted using Alloy 22 coupled multielectrode array probes at 125 °C [257 °F] and relative humidities near the deliquescence point of an NaCl–KNO<sub>3</sub>–NaNO<sub>3</sub> salt mixture. The results indicate that the corrosion rate of Alloy 22 was significantly lower than that of carbon steel, and no visible localized corrosion was observed. Because the coupled multielectrode probe measures the rate of nonuniform corrosion, including localized corrosion, the low currents measured with the Alloy 22 probe also indicate that the penetration rate of localized corrosion in the dust and NaCl–KNO<sub>3</sub>–NaNO<sub>3</sub> mixture is low at 125 °C [257 °F] under the test conditions.

## 5.2 Corrosivity of Potential Deliquescence Brines to Alloy 22 Waste Package Materials

The corrosivity of large quantities of potential deliquescence brines in contact with Alloy 22 was reviewed. Weight loss measurements for Alloy 22 in closed autoclaves and in open systems containing NaCl–KNO<sub>3</sub>–NaNO<sub>3</sub> salt mixtures were reported for temperatures ranging from 120 to 220 °C [248 to 428 °F]. The corrosion rate measured in closed autoclaves was lower than 1 μm/yr [0.04 mil/yr]. The measurements using Alloy 22 specimens with different metallurgical treatment (mill annealed, thermally aged, welded, and welded plus solution annealed) in a system open to the atmosphere that simulates plausible drift environments at the Center for Nuclear Waste Regulatory Analyses laboratory showed low corrosion rates except for cases where the pH of the solution was low. Only when the solution pH was lower than 4.5 as measured at room temperature after tenfold dilution by weight was the corrosion rate high and increased dramatically with decreasing pH. The dependence of the corrosion rate on different pH solutions was verified with an Alloy 22 coupled multielectrode array sensor. The corrosion rate of Alloy 22 was equal or lower than 1 μm/yr [0.04 mil/yr] in the NaCl–KNO<sub>3</sub>–NaNO<sub>3</sub> brine at 160 °C [320 °F] when the solution pH measured at room temperature after tenfold dilution by weight ranged from 4.8 to 8.5. The low pH observed in the test solutions was attributed to the impurities contained in the reagent grade salts used in the test. It is not clear whether such low pH brines could be formed under the potential Yucca Mountain drift conditions or whether such low pH brines, if formed, would persist over a long period of time and affect the integrity of the waste package containers.

Corrosion rates of Alloy 22 were also reported for concentrated brines obtained by evaporation of solutions containing Mg<sup>2+</sup>, Ca<sup>2+</sup>, Na<sup>+</sup>, K<sup>+</sup>, Cl<sup>-</sup>, and NO<sub>3</sub><sup>-</sup>. Corrosion rates varied between 5 and 100 μm/yr [0.2 and 4 mil/yr] within the temperature range of 110 to 145 °C [230 to 293 °F]. Localized corrosion in the form of pitting corrosion was also observed in the specimens. Because the vapor condensate and the residual liquid contacting the Alloy 22 specimen had a pH close to 1 or less. The hydrolysis of the alkaline earth metals (magnesium and calcium cations) present in the system caused the decrease in the solution pH. The observed high corrosion rates are consistent with the measured corrosion rates in the NaCl–KNO<sub>3</sub>–NaNO<sub>3</sub> solutions at low pH values (< 4.5 as measured at room temperature after tenfold dilution by weight). However, such low pH systems may not last for long periods of time especially under potential repository conditions, because the hydrolysis process would eventually deplete the acid-producing alkaline earth metal ions.

## 5.3 Localized Corrosion of Alloy 22 in Deliquescence Brines Under Potential Yucca Mountain Conditions

At temperatures between 120 and 150 °C [248 and 302 °F], the literature data on repassivation and corrosion potential indicate that localized corrosion in the form of crevice corrosion in the presence of large quantities of dust deliquescence brines could initiate only when pH is close to or lower than 2. The reported values of the repassivation potential of Alloy 22 in dust deliquescence brines that are likely to form at these temperatures (nitrate-to-chloride molar ratio > 5) lie above 0.44 V<sub>SSC</sub>. For corrosion potential to exceed this value of the repassivation potential, the solution pH should be close to 2, which is far lower than the values normally expected under potential repository conditions.

At temperatures between 100 and 120 °C [212 and 248 °F], however, the low nitrate-to-chloride molar ratio (<0.1) that may be present in the deliquescence brines from nitrate and chloride salt

mixtures would not be sufficient to prevent localized corrosion by raising the repassivation potentials. It is not clear whether high concentrations of other anions such as sulfate, bicarbonate, and carbonate also present in the nitrate-lean brines would be effective inhibitors to raise the repassivation potentials of Alloy 22 under the deliquescence brine conditions. Those anions were localized corrosion inhibitors for Alloy 22 at 95 °C [203 °F], but there are no data available for temperatures above 100 °C [212 °F].

The immersion test data discussed in the literature obtained from both closed autoclaves and open dripping environments indicated that localized corrosion of Alloy 22 specimens initiated at temperatures equal to or greater than 140 °C [284 °F] in nitrate-rich solutions where the nitrate-to-chloride molar ratio was greater than 5. Localized crevice corrosion was also observed for specimens exposed to the vapor phase of the autoclave containing large quantities of nitrate-rich brine solutions. These observations appear to contradict the conclusions derived from repassivation and corrosion potential measurements, which indicated that localized corrosion is unlikely in dust deliquescence brine solutions with nitrate-to-chloride molar ratios greater than 5. It is not clear, however, whether the observed localized corrosion of Alloy 22 in the presence of large quantities of brines would propagate further with time. Additional data are needed to examine the discrepancy between the results of corrosion and repassivation electrochemical potential measurements and the immersion tests if the repassivation potential data are applied to evaluate the localized corrosion of Alloy 22 in large quantities of dust deliquescence brines.

The measurements using the Alloy 22 coupled multielectrode probe indicated that the rate of nonuniform corrosion, including localized corrosion, was lower than 1  $\mu\text{m}/\text{yr}$  [0.04 mil/yr] in large quantities of saturated NaCl–KNO<sub>3</sub>–NaNO<sub>3</sub> brine at 130 °C [266 °F] for pH values from 4.8 to 8.5 (as measured at room temperature for the liquid that was diluted by tenfold).

The results of cathodic capacity estimations indicate that a sufficient positive value of  $E_{\text{corr}} - E_{\text{rp}}$  is needed to achieve high penetration rates. Based upon the experimentally measured values of  $E_{\text{corr}}$  and  $E_{\text{rp}}$ , it can be deduced that  $E_{\text{corr}} - E_{\text{rp}}$  can, at most, be equal to 0.2 V and the maximum cathodic capacity on the order of  $10^{-6} \text{ A}/\text{cm}$  [ $2.54 \times 10^{-6} \text{ A}/\text{in}$ ]. The high crevice penetration rate over a large surface area of the crevice region cannot be achieved with the cathodic capacity of  $10^{-6} \text{ A}/\text{cm}$  [ $2.54 \times 10^{-6} \text{ A}/\text{in}$ ]. Even though a large penetration rate can be achieved over a smaller crevice region, a smaller crevice site would be of less risk significance to the release of radionuclides than a larger site.

Considering that the amount of dust deliquescence brines on the waste package would be extremely small and the brine would be mixed with insoluble dust particles, the localized corrosion rate in the presence of dust deliquescence brines under plausible repository conditions is relatively low. This conclusion is supported by the low nonuniform corrosion current measured with the Alloy 22 coupled multielectrode probe in the mixture of dust and NaCl–KNO<sub>3</sub>–NaNO<sub>3</sub> at 125 °C [257 °F].